

# **Advanced Studies on Neutron Stars and Pulsars**

## **THESIS**

Submitted in partial fulfillment  
of the requirements for the degree of  
**DOCTOR OF PHILOSOPHY**

by

**NOBLESON K.**

**ID No. 2018PHXF0458H**

Under the Supervision of  
**Prof. SARMISTHA BANIK**




**BITS Pilani**  
Pilani | Dubai | Goa | Hyderabad


**BIRLA INSTITUTE OF TECHNOLOGY & SCIENCE, PILANI**

**2023**

# Certificate


This is to certify that the thesis entitled ‘**Advanced Studies on Neutron Stars and Pulsars**’ and submitted by **NOBLESON K.**, ID.No. **2018PHX0458H** for award of Ph.D. of the Institute embodies original work done by him under my supervision.

Signature of the Supervisor :   
Name in capital letters : **Prof. SARMISTHA BANIK**  
Designation : **Professor**

Date : 

# Declaration

I, **Nobleson K.**, declare that this thesis titled, '**Advanced Studies on Neutron Stars and Pulsars**', submitted by me under the supervision of **Prof. Sarmistha Banik** is a bonafide research work. I also declare that it has not been submitted previously in part or in full to this University or any other University or Institution for award of any degree.

Signature of the student :   
Name of the student : **NOBLESON K.**  
ID number of the student : **2018PHX0458H**  
Date : **October 31, 2023**

# Acknowledgements

I want to start by expressing my sincere appreciation to Prof. Sarmistha Banik, my adviser, for her unwavering support, direction, and encouragement during the course of my research. Her expertise, zeal, and generosity have been invaluable. I also am thankful to her for organizing the “*Pulsar Astronomy with uGMRT Boot-Camp & Multi-Wavelength Neutron Star Workshop*” during January 3-8, 2018, which introduced me to the science of Pulsar Timing Array and the wonderful collaboration, Indian Pulsar Timing Array (InPTA).

I have been an active member of InPTA throughout my graduate career, and I am grateful to all of its members. I have benefited immensely from the expertise of this community of scientists. Special thanks to Prof. Bhal Chandra Joshi, Dr. Krishnakumar, and Prof. Shantanu Desai who, from time to time, provided training (with a lot of hand holding) by sharing their wealth of knowledge and skills pertaining to pulsar astronomy.

I would also like to thank Prof. P. K. Thiruvikraman and Dr. Sashideep Gutti from the Doctoral Advisory Committee for their informative remarks and constructive criticism. Their expertise and attention to detail have been invaluable in assisting me in improving my research and writing.

I wholeheartedly thank all my teachers from my High school to the University and friends who played an important role in shaping me as a person.

I am also thankful to all my colleagues in the Department who have made it a welcoming and exciting place to work. I will fondly remember the discussions and friendly banter. I am grateful for the relationships and partnerships that developed along the way. Heartfelt thanks to Dr. Amna Ali for collaborating with me on my first research project. A special thanks to Dr. Tuhin Malik for being a wonderful collaborator and a host during my visit at the University of Coimbra, Portugal.

I want to thank the larger academic community, whose research and perspectives have influenced and informed mine. I am grateful to the several academics and researchers who have advanced my understanding of the subject, and I consider it an honor to be a part of this group of forward-thinking individuals. Thank you to everyone who has contributed to my academic and personal development. I could not have gotten to this stage without your help, and I am eternally thankful.

Finally, I want to acknowledge the sacrifices of my mother, P. S. Annamma, without which I would not be here today. Many many thanks to my wife, P. Sirisha, for her unfailing love and support throughout the life that we shared together. Her encouragement and understanding has been a constant source of strength throughout my academic journey.

# Abstract

Neutron stars are remnants of massive main sequence stars ( $> 10 M_{\odot}$ ) that have reached the end of their lives in a cataclysmic supernovae and are no longer producing nuclear fusion. With no outward pressure from fusion to counterbalance gravity's inward pull, the star condenses and collapses in upon itself, compressing a couple of sun's worth of mass in a tiny sphere of a few kilometers. Because of this, aside from black holes, they are known to be the densest objects in the universe and are uniquely suited to study gravitational interactions in strong-field regime.

General relativity (GR) has had tremendous success in describing the large-scale structure and dynamics of the universe. However, there are certain observed phenomena, such as accelerated expansion of the universe and incompatibility with quantum mechanics, which remain unexplained. Modifications to GR were proposed to explain these phenomena. Modified gravity theories are theoretical frameworks that propose modification to GR. In recent years, neutron stars have emerged as valuable tools for studying modified theories of gravity. These incredibly dense stellar objects provide unique environments to test the limits of our current understanding of gravity and explore alternative theories. One widely studied modified gravity model is represented by the function  $f(R) = R + \alpha R^2$ , where  $R$  is the Ricci scalar and  $\alpha$  is a parameter determining the strength of the modification. When investigating the behavior of neutron stars in modified gravity, we see that there are two main approaches to derive the Tolman-Oppenheimer-Volkoff (TOV) equations, which describe the equilibrium configurations of these stars. They are referred to as perturbative and non-perturbative methods. There is an ongoing debate surrounding the accurate method for deriving the TOV equations in modified gravity. To resolve this debate and determine the most rigorous method, our first study compares the predictions of both the methods with same equation of states (EoS) of neutron stars and observational constraints. We conclude that the non-perturbative method is the preferred one. The EoS refers to the mathematical relationship between the pressure and density of a system that plays an important role in understanding the structure and properties of neutron stars.

In our second study, we analyze the properties of neutron stars within  $f(R)$  gravity using a Bayesian approach. Bayesian analysis is a statistical method that allows researchers to infer the probability distribution of model parameters given the available data and any prior knowledge or assumptions. Three realistic EoS which are generated using a relativistic mean field framework are used. These EoS span the range of uncertainties in stiffness, which refers to how the pressure of matter inside the neutron star responds to changes in density. In this case, the analysis focuses on determining the posterior distribution of the free parameter  $\alpha$  in the  $f(R)$  model. The study incorporates observational constraints from Neutron Star Interior Composition Explorer (NICER) observations. These constraints include the maximum mass of neutron stars, the radius corresponding to maximum mass, and the radius of a neutron star with a mass of 1.4 times the solar mass (denoted as  $1.4 M_{\odot}$ ). The findings of this study reveal a universal

relationship between the parameter  $\alpha$  of the  $f(R)$  gravity model and the maximum mass of the neutron star. This means that there is a correlation or functional dependence between the free parameter of the modified gravity theory and the maximum mass that a stable neutron star can attain.

In our third study, we investigate several neutron star properties in modified gravity using density dependent relativistic mean field EoS that considers different particle compositions within the core of the neutron star. We specifically chose the presence of nucleons and strange particles, such as  $\Lambda$  hyperons,  $K^-$  condensate, and quarks. The results of this study reveal interesting findings. Firstly, the mass-radius relation for neutron stars in this non-perturbative  $f(R)$  gravity model allows for a wide range of values for the parameter  $\alpha$ . Observational constraints from the NICER data are also used in the course of the study. These constraints include the maximum mass of neutron stars, the radius of maximum mass, and tidal deformability inferred from the binary neutron star merger of GW170817 observed by LIGO and Virgo collaborations. Tidal deformability quantifies how much a compact object, such as a neutron star, is deformed under the influence of tidal forces exerted by a companion object during a gravitational interaction. Our study finds that the observed neutron star mass and its radius are not sufficient to constrain the value of  $\alpha$ . However, the inferred value of tidal deformability from the merger of binary neutron stars imposes an upper bound on the possible values of  $\alpha$ , narrowing down the parameter space by one order of magnitude.

The next portion of our study focuses on the application of the wideband timing technique on the data obtained using low-frequency wideband receivers. This research is conducted as part of the Indian Pulsar Timing Array (InPTA) project, utilizing observations from the upgraded Giant Metrewave Radio Telescope (uGMRT) in the frequency range of 300–500 MHz. The radio frequencies undergo dispersion due to the interstellar medium. Dispersion measure (DM) refers to the total electron content along the line of sight between the pulsar and the observer. These electrons cause delays in the time of arrivals (ToAs) of pulsar signals due to dispersion. By accurately measuring the DM, information about the density of free electrons along the line of sight to the pulsar can be obtained. Traditionally, DM measurements were obtained using narrowband observations at specific frequencies. However, the wideband timing technique allows simultaneous measurements of both pulsar ToAs and DMs using telescopes equipped with wideband receivers. In this study, we utilize the data from the uGMRT observations of five pulsars that are part of the InPTA campaign. The estimated DM measurements demonstrate high precision, reaching up to an order of  $10^{-6}$  pc cm $^{-3}$ . This level of precision enables detailed investigations of the interstellar medium and its impact on pulsar timing. The ToAs obtained from the wideband timing technique exhibit sub-microsecond precision. The post-fit residuals, which represent the differences between the observed and modeled ToAs, have root mean square (rms) values in the sub-microsecond range. These results highlight the effectiveness of the wideband timing technique for achieving precise pulsar timing measurements. Importantly, the study finds that the uncertainties in DM measurements and ToAs obtained through the wideband technique, applied to low-frequency data, are consistent with the results obtained using traditional pulsar timing techniques. Furthermore, the precision achieved with the wideband technique is comparable to the results obtained from other pulsar timing arrays (PTAs) that utilize high-frequency observations. Conventionally, high-frequency observations have been the norm for such studies, but this work demonstrates that similar level of precision can be achieved using low-frequency wideband observations as well. This opens up new avenues for studying pulsars and their interactions

with the interstellar medium, as well as exploring gravitational wave signals through pulsar timing techniques. Very recently this method has been applied to the data of 14 pulsars as part of the first InPTA data release.

## **Results at a Glance**

- In this thesis, we settle the debate between perturbative and non-perturbative approaches of deriving the TOV equations in  $f(R)$  gravity. We conclude that non-perturbative method is a robust and preferred method.
- We demonstrate that the tidal deformability parameter can constrain the free parameter  $\alpha$  of modified gravity by an order of magnitude based upon the inferred tidal deformability parameter obtained from the binary neutron star merger.
- We analyze the neutron star properties with  $f(R)$  gravity model using the Bayesian approach and unveil a universal relationship between the parameter  $\alpha$  and the neutron star maximum mass.
- We demonstrate that the wideband timing technique can be applied to low-frequency pulsar observation data to estimate the DM and ToAs. These results are consistent with the results obtained from other PTAs.

# Contents

<b>Acknowledgements</b>	<b>iii</b>
<b>Abstract</b>	<b>vi</b>
<b>List of Tables</b>	<b>ix</b>
<b>List of Figures</b>	<b>x</b>
<b>1 Introduction</b>	<b>1</b>
1.1 Neutron Stars and Pulsars . . . . .	1
1.2 Motivation . . . . .	9
1.3 Aims and Scope . . . . .	10
<b>2 Equation of State</b>	<b>11</b>
<b>3 Modified Gravity Theories</b>	<b>16</b>
3.1 Introduction . . . . .	16
3.2 Formalism . . . . .	18
3.2.1 NS in GR . . . . .	18
3.2.2 NS in $f(R)$ Using Perturbative Method . . . . .	19
3.2.3 NS in $f(R)$ Using Non-Perturbative Method . . . . .	20
3.2.4 Tidal Love number . . . . .	24
<b>4 Understanding Modified Gravity: Insights from Our Results</b>	<b>28</b>
4.1 Comparison of Methods in $f(R)$ . . . . .	29
4.1.1 Results and Discussions . . . . .	30
4.1.2 Conclusions . . . . .	35
4.2 Universal Relation in $f(R)$ . . . . .	36
4.2.1 Bayesian estimation . . . . .	37
4.2.2 Results and Discussions . . . . .	39
4.2.3 Conclusions . . . . .	48
4.3 Tidal Deformability in $f(R)$ . . . . .	49
4.3.1 Results and Discussions . . . . .	50
4.3.2 Conclusions . . . . .	54



<b>5</b>	<b>Role of Pulsars in Gravitational Wave Science</b>	<b>55</b>
5.1	Introduction . . . . .	55
5.1.1	Gravitational Wave Spectrum . . . . .	55
5.1.2	Pulsar Timing Arrays . . . . .	56
5.1.3	The InPTA Experiment . . . . .	57
5.1.4	Brief Introduction to Pulsar Timing . . . . .	57
5.2	Application of Wideband Method to Low-Frequency Observations . . . . .	63
5.2.1	Observations and Data Reduction . . . . .	64
5.2.2	Our Findings . . . . .	65
5.2.3	Conclusions and Discussions . . . . .	78
5.3	Wideband Method in InPTA Data Release 1 . . . . .	81
5.3.1	Observations and Data Processing . . . . .	81
5.3.2	Conclusions . . . . .	84
<b>6</b>	<b>Conclusions</b>	<b>87</b>
6.1	Summary . . . . .	87
6.2	Future Scope of Work . . . . .	88
	<b>Bibliography</b>	<b>90</b>
	<b>List of Publications and Presentations</b>	<b>112</b>
	<b>Brief Biography of the Candidate</b>	<b>113</b>
	<b>Brief Biography of the Supervisor</b>	<b>114</b>

# List of Tables

2.1	Table of nuclear properties . . . . .	14
4.1	Maximum mass and corresponding radius of the NS for $a=0$ (GR); $a = 50$ for non-perturbative (NP) $f(R)$ and $a = 0.2$ for perturbative (P) $f(R)$ . . . . .	31
4.2	Constraints imposed in the Bayesian inference . . . . .	38
4.3	Universal relation curve fit values . . . . .	46
4.4	$M_{max}$ , $R_{S,1.4}$ , and $\Lambda_{1.4}$ for different $\alpha$ . . . . .	52
5.1	Gravitational wave detectors . . . . .	56
5.2	Summary of the results of the PulsePortrait analysis . . . . .	74
5.3	Comparison of the WT and NT postfit timing parameters . . . . .	77

# List of Figures

2.1	Energy density versus pressure curves . . . . .	15
4.1	EoS and M-R curves in GR . . . . .	31
4.2	M-R curves of perturbative and non-perturbative methods of DD2 and $BHB\lambda\phi$ . . . . .	32
4.3	M-R curves of perturbative and non-perturbative methods of FSU and FSUQ . . . . .	33
4.4	Compactness of NS in perturbative and non-perturbative methods . . . . .	34
4.5	Normalized compactness of NS in perturbative and non-perturbative methods . . . . .	35
4.6	Validity of perturbative method . . . . .	35
4.7	Baryonic number density versus pressure . . . . .	39
4.8	Posteriors of the parameter $\alpha$ for $f(R)$ gravity . . . . .	40
4.9	M-R domain in $f(R)$ for DD2, FSU2R, SFHx . . . . .	41
4.10	Kendall rank correlation coefficients . . . . .	42
4.11	Normalized radius versus $\alpha$ , . . . . .	43
4.12	Normalized maximum mass versus $\alpha$ . . . . .	44
4.13	Normalized central density versus normalized radius of the maximum mass . . . . .	47
4.14	Energy density versus pressure curves for different EoS . . . . .	50
4.15	M-R curves in GR and $f(R)$ . . . . .	51
4.16	Tidal Love Number ( $k_2$ ) versus Compactness (C) . . . . .	52
4.17	Tidal deformability ( $\Lambda$ ) versus mass . . . . .	53
5.1	Sky distribution of InPTA pulsars . . . . .	57
5.2	Fiducial DM-subtracted plots with different nbins . . . . .	66
5.3	Fiducial DM-subtracted plots with different nchans . . . . .	67
5.4	Median-subtracted DM plots . . . . .	68
5.5	Timing residuals . . . . .	69
5.6	Plot of eigenprofiles . . . . .	70
5.7	Comparison of the DM uncertainties obtained with DMcalc and PulsePortraiture . . . . .	71
5.8	DM time-series for 14 pulsars . . . . .	85

## Chapter 1

# Introduction

*"Somewhere, something incredible is waiting to be known."* – Carl Sagan

### 1.1 Neutron Stars and Pulsars

When massive stars die in a catastrophic explosion, the stellar material is expelled into the interstellar environment. A rapidly spinning core is left in its wake. It sweeps an electromagnetic radiation beam around the sky. When these beams cross the Earth, we detect it as a pulse on a telescope. A regular pulse of 1.337 seconds was first observed in 1967 by Jocelyn Bell Burnell ([Hewish \*et al.\*, 1968](#)). It was unknown at the time what caused these regular pulsed signals. Interestingly, Baade and Zwicky predicted in 1934 that when a large star explodes in a supernova, the remaining iron core compresses into a dense core of neutrons ([Baade and Zwicky, 1934](#)). This remnant is referred to as a neutron star (NS). The magnetic field and angular momentum imparted onto a NS by the death of its progenitor gives it a magnetic field strength of around  $10^{12}$  gauss and a spin period of up to tens of milliseconds. A self-gravitating object can only spin so fast before it disintegrates; a spin period of 33 milliseconds indicates a minimum density of the order of nuclear matter. The discovery of the Crab pulsar ([Staelin and Reifstein, 1968](#)), with its short 33 millisecond spin period and intrinsic spin down of 36 nanoseconds per day, could only be explained by a rotating NS. The discovery of the Crab and Vela pulsars ([Large \*et al.\*, 1968](#)) provided strong evidence that NS are created as a result of supernova explosions when high mass stars end their fusion-powered lives. The nuclear burning generates an iron-rich core. When all the nuclear fuel in the core is depleted, the core is maintained only by the electron degeneracy pressure. Additional mass deposits from the shell burning lead the core to surpass the Chandrasekhar limit causing further collapse. The intense gravitational forces in the core of the collapsing star cause the protons and electrons to combine through a process called electron capture, resulting in the formation of neutrons and neutrinos. In addition to neutron-degenerate matter, there is a theoretical possibility that exotic matter

(hyperons, quarks, and strange particles) may exist within NS.

The equation of state (EoS) describes the relationship between the pressure, density, and other physical properties of matter inside a NS. The EoS is derived from the fundamental laws of physics, such as quantum chromodynamics and interaction of fundamental particles. It determines the structure and properties of NS. The exact composition of NS beyond the presence of neutrons can be complex and is still an area of ongoing research. The composition and internal structure of NS depend on factors such as the star's mass, rotation, and cooling history. These NS properties can be studied through various methods of astronomical observations such as:

- **Electromagnetic radiation:** NS can emit electromagnetic radiation across a wide range of wavelengths. This includes radio waves, optical, X-rays, and gamma rays. The radiation is emitted from various processes, such as thermal radiation from the surface, synchrotron radiation from high-energy particles, and pulsed emissions from rotating NS ([Lorimer and Kramer, 2012](#)). Observations of NS at optical and infrared wavelengths have expanded from the more classical rotation-powered ones to other categories, like the Anomalous X-ray Pulsars (AXPs) and the magnetars ([Mignani \*et al.\*, 2007](#)). NS in binary systems can accrete matter from a companion star. This accretion process can generate intense X-ray emission due to the heating and compression of the accreted material. X-ray binaries provide insights into the properties of NS, as well as the dynamics of accretion processes ([Tauris and van den Heuvel, 2006](#)).
- **Cooling curves:** NS gradually cool down over time as they radiate away their thermal energy. Observing the cooling curves of NS, particularly in X-rays, can provide information about their internal composition, superfluidity, and the presence of exotic matter ([Ofengeim and Yakovlev, 2017](#)).
- **Neutrinos:** NS mergers, supernovae, and other astrophysical events involving NS can produce intense neutrino emission. Detecting these neutrinos provides important insights into the core physics, energy release mechanisms, and nucleosynthesis processes associated with NS ([Sato \*et al.\*, 2021](#)).
- **Gravitational waves:** NS, particularly those in binary systems, can emit gravitational waves. The first indirect discovery was from observation of binary neutron stars PSR 1913 + 16 ([Weisberg and Taylor, 1981](#); [Hulse, 1994](#); [Weisberg \*et al.\*, 2010](#)). These ripples in the fabric of spacetime are generated by the orbital motion and eventual merger of NS. Observatories such as LIGO and Virgo

(Abbott *et al.*, 2016) have detected gravitational waves from NS mergers, providing information about their masses, tidal effects, and equation of state.

There are several physical observables of NS that can be studied and measured.

- **Mass:** The mass of a NS is one of its primary physical observables. NS typically have masses several times that of our Sun, with a canonical mass of  $1.4 M_{\odot}$ . The masses of NS in binary systems can be accurately measured using various methods such as analyzing the X-ray pulse profile, measuring the Doppler shift of the companion star, and analyzing the gravitational waves emitted by the system (Tang *et al.*, 2020; Miller and Lamb, 2016). The NASA's Neutron Star Interior Composition Explorer (NICER) constrains the mass of PSR *J0740 + 6620* at  $2.072 \pm 0.067 M_{\odot}$ . PSR *J0952 - 0607*, the most massive NS discovered so far, is estimated to have  $2.35 \pm 0.17 M_{\odot}$  (Romani *et al.*, 2022).
- **Radius:** The radius of a NS is another important physical observable. However, directly measuring the radius is challenging due to the compact nature of NS and large distances from earth. The effective tidal deformability of the binary can be used to directly measure the NS radius (Raithel *et al.*, 2018; De *et al.*, 2018). Indirect methods, such as modeling thermal emission (Miller *et al.*, 2019; Riley *et al.*, 2021) and gravitational effects, are used to estimate NS radii (Bauswein *et al.*, 2017). They typically have a radius of 10-15 km. Radius of PSR *J0030 + 0451* is  $13.02 \pm 1.24$  km. (Miller *et al.*, 2019)
- **Surface temperature:** The surface temperature of NS can change over time due to various factors. Joule heating caused by dissipation of the magnetic field in the neutron star crust can maintain a relatively high surface temperature in very old NS for an extremely long time ( $>100$  Myr), comparable with the decay time of the magnetic field (Miralles *et al.*, 1998). Observing the X-ray or optical emissions from the surface can provide information about the surface temperature. Studying the surface temperature helps understand the cooling mechanisms and properties of the outer layers of NS. The temperatures usually range from  $10^6$  to  $10^{12}$  kelvin depending on the age of the NS.
- **Rotation period:** NS often have incredibly fast rotation periods. Also known as pulsars, their rotation period, or spin period, can be measured by tracking the arrival times of these pulses. Pulsar timing provides valuable information about the NS rotation and its magnetic field. PSR *J17482446ad* is known to have a short period of 1.4 milliseconds (716 times per second) (Hessels

*et al.*, 2006).

- **Magnetic field:** NS can have powerful magnetic fields with non-trivial origins and evolution. Observations indicate that magnetic fields on NS span at least  $10^8 - 10^{15}$  G, corresponding to a range of magnetic fields similar to that found in white dwarfs and main sequence stars. The origin and evolution of NS magnetic fields are still yet to be fully understood; various theoretical models have been proposed. Physical processes potentially leading to magnetic field evolution include thermal creep of pinned vortices, outward motion of proton vortices, and superconductivity. The magnetic field in the core of a NS cannot be considered frozen or vanishing, and its temporal evolution should affect the observational properties of neutron stars. The presence of NS with large magnetic fields in binary systems is still unexplained. However, there are many claims based on model-dependent analysis of spin properties or/and luminosity of NS in X-ray binaries in favor of large fields (Lugones, 2005; Gusakov *et al.*, 2020; Popov, 2020).
- **Tidal deformability:** It is a measure of the object's response to the gravitational field of its companion. In recent years, the tidal deformability of NS has been investigated, notably following the detection of gravitational waves from the merging of binary NS in the event GW170817 (Raithel *et al.*, 2018; Wei *et al.*, 2019). The binary's effective tidal deformability can be used to directly measure the NS radius, and the upper limit on GW170817's effective tidal deformability implies that the radius cannot be larger than approximately 13 km at the 90% confidence level, regardless of the assumed masses for the component stars. The NS radii constraints imposed by a determination of the average tidal deformability of the binary NS system GW170817 are consistent with radius ranging from 12 to 13 km (Wei *et al.*, 2019). The binary's effective tidal deformability primarily depends on the ratio of the chirp mass-to-NS radius, and measuring it may be employed to investigate the stellar radii in any NS-NS merger with a measured chirp mass. The observed tidal deformability of a binary NS system may additionally constrain the upper bound of the speed of sound in dense nuclear matter (Kanakis-Pegios *et al.*, 2020).

Studying these observables helps in gaining a deeper understanding of NS properties, their formation mechanisms, equation of state, and the behavior of matter under extreme conditions.

NS and gravitational waves are closely connected through their association with compact binary systems. When two NS or a NS and a black hole orbit each other closely, they can emit gravitational waves as predicted by Einstein's theory of general relativity (GR). Gravitational waves are perturbations in the fabric of spacetime that propagate at the speed of light. These are produced by the acceleration

of heavy objects such as NS or black holes. They were predicted by GR and were first directly detected in 2015, opening up new possibilities for exploring the universe ([Abbott \*et al.\*, 2016](#); [Dirkes, 2018](#)). Gravitational waves, like electromagnetic radiation, have a spectrum. It has an extensive range. However, the frequencies of gravitational waves are typically much lower than those of electromagnetic waves. The main regions of the gravitational wave spectrum are as follows:

- **Low-frequency regime:** This includes waves with frequencies below  $100 \mu\text{Hz}$ . Sources in this range could be supermassive black hole mergers, cosmic strings, or relics from the early universe.
- **Intermediate-frequency regime:** This range spans from approximately  $100 \mu\text{Hz}$  to  $10 \text{ Hz}$ . Sources in this regime could include binary systems consisting of neutron stars and black holes.
- **High-frequency regime:** This covers frequencies in the range of  $10 \text{ Hz}$  to  $10 \text{ kHz}$ . Sources in this range include stellar-mass compact objects, such as neutron stars and black holes, and could also involve phenomena related to the early universe.

Detecting gravitational waves across the entire spectrum requires different types of detectors and techniques. Advanced LIGO and Virgo are ground-based detectors primarily focused on the high-frequency regime, while space-based detectors like LISA (Laser Interferometer Space Antenna) aim to observe the intermediate-frequency regime, and Pulsar Timing Arrays (PTA) and CMB polarization aim to observe the low-frequency regime. Depending on the source of the gravitational waves, these can be of several types:

- **Continuous waves:** These are produced by rotating asymmetric objects, such as neutron stars, which emit gravitational waves at a constant frequency. Continuous waves are often searched for using dedicated detectors like PTA and ground-based detectors.
- **Burst waves:** These waves are produced by sudden and violent events, such as the collision and/or scattering of two black holes or the explosion of a supernova. Burst waves have a short duration and a wide range of frequencies.
- **Stochastic background:** A stochastic background of gravitational waves refers to a pervasive and random distribution of gravitational waves at different frequencies throughout the universe. These waves can arise from a variety of sources, such as the mergers of black holes and neutron stars, cosmic inflation in the early universe, or other astrophysical processes. The stochastic nature of the background means that it does not originate from a single, localized source but is instead a superposition of waves from many different sources.



In this thesis, our interest lies in the analyses that facilitate the detection of a stochastic gravitational wave background (SGWB). The detection of SGWB differs from the detection of individual gravitational wave events in several ways:

- Detection method:
  - The detection of individual gravitational wave events relies on the identification of a specific waveform in the data from a single detector or a network of detectors ([Renzini \*et al.\*, 2022](#)).
  - Detection of SGWB would require detectors with arm lengths of the order of light years which cannot be achieved by ground-based or the upcoming space-based interferometric gravitational wave detectors. Nature, on the other hand, has endowed us with detectors located light years apart that can potentially be used to detect nanohertz gravitational waves. The detection of an SGWB relies on the cross-correlation of data from multiple detectors to extract the signal from the noise ([Romano and Cornish, 2017](#)).
- Observable:
  - The detection of individual gravitational wave events provides information about the properties of the source, such as the masses and spins of the merging black holes or neutron stars.
  - The detection of an SGWB provides information about the population of sources that contribute to the background, such as the merger rate and mass distribution of binary black holes ([Romano and Cornish, 2017](#)).
- Signal strength:
  - The amplitude of individual gravitational wave events is typically much larger than the amplitude of the SGWB, which is a collection of unresolved signals that lie below the detection threshold of current detectors ([Romano and Cornish, 2017](#)). Recently, in May 2023, there was an announcement of detecting SGWB signals in the PTA dataset.
- Frequency range:
  - The frequency range of individual gravitational wave events is typically narrow and determined by the masses of the merging objects.
  - The frequency range of the SGWB is broad and determined by the population of sources that contribute to the background ([Romano and Cornish, 2017](#)).

Detecting SGWB is a challenging task due to several reasons, including:

- Low amplitude: The amplitude of the SGWB is typically much smaller than the amplitude of individual gravitational wave events, making it difficult to detect (Renzini *et al.*, 2022).
- Broad frequency range: The frequency range of the SGWB is broad and determined by the population of sources that contribute to the background, making it challenging to distinguish the SGWB from other sources of noise in the data (Romano and Cornish, 2017; Renzini *et al.*, 2022).
- Computational requirements: The detection of an SGWB requires the cross-correlation of data from multiple detectors, which can require vast computer memory and processing time (Thrane *et al.*, 2015).
- Systematic errors: The detection of an SGWB is also susceptible to systematic errors, such as instrumental noise and calibration errors, which can mimic the SGWB signal (Meacher *et al.*, 2015).
- Astrophysical uncertainties: The properties of the sources that contribute to the SGWB, such as the merger rate and mass distribution of binary black holes, are not well understood, which makes it challenging to model the SGWB signal (Renzini *et al.*, 2022)

Pulsar timing arrays (PTAs) are ultra-stable galactic pulsars that are distributed more or less uniformly across the sky. They each rotate a few hundred times every second on their own axis while emitting collimated radio beams over a broad range of wavelengths. They can be used for detecting SGWB created by the cosmological history of hierarchical supermassive black hole formation from mergers (Bertotti *et al.*, 1983) by analysing the pulsed emission using pulsar timing methods. Pulsar beams sweeping across the Earth produce pulses that correlate to the spin of the NS. PTAs can detect low-frequency gravitational waves by searching for a correlated signature between pulsars, arising from the influence of gravitational waves at the Earth. PTAs complement other methods of gravitational wave detection in their frequency coverage and the physics they probe. They are sensitive to gravitational waves with frequencies in the nanohertz range ( $10^{-9}$  Hz -  $10^{-7}$  Hz), which are lower than the frequencies that ground-based or space-based interferometers are sensitive to. PTAs work by measuring the times-of-arrival (ToAs) of radio pulses emitted from pulsars. These measurements contain many terms of known functional form (pulsar period, spin-down, etc.), radiometer noise, pulse phase jitter, and possible signals from gravitational waves. The line of sight from the telescope to the precise pulsar clock acts like a detector-arm sensitive to the passage of gravitational waves through space. By comparing observations of

many stable pulsars, PTA can detect gravitational waves, improve the solar system planetary ephemeris, and study irregularities in terrestrial time scales.

Some of the challenges in using PTAs to detect gravitational waves are:

- **Reducing noise:** One of the key difficulties in using PTAs to detect gravitational waves is reducing the noise in the pulsar data. The noise can come from a variety of sources, including the pulsar itself, the interstellar medium, and the stability of terrestrial clocks. Reducing the noise is important because it can make it easier to detect the gravitational wave signal (Hobbs, 2005; Lommen, 2015).
- **Number of pulsars:** Another challenge is determining how many pulsars should be in the array. The greater the number of pulsars, the better the chance of detecting a gravitational wave signal. However, adding more pulsars also increases the complexity of the analysis and the computational resources required (Hobbs, 2011).
- **Source detection:** It is not clear what kind of source will be detected first using PTAs. The expected sources of gravitational waves include supermassive black hole mergers, cosmic strings, and other astrophysical phenomena. Detecting these sources will require careful analysis of the data and sophisticated statistical techniques (Hobbs, 2005).
- **Large bandwidth systems:** PTAs have a large bandwidth, which can make it difficult to analyze the data. Accommodating these large bandwidth systems is a challenge that requires careful planning and the development of new analysis techniques (Lommen, 2015).

Detecting and characterizing the stochastic background of gravitational waves can provide insights into the overall population of sources and the evolution of the universe itself.

Also, because NS are the densest objects in the universe, they allow us to study the effects of gravity in the strong field regime. The concept of modified gravity refers to the possibility that the laws of gravity differ from those described by Einstein's theory of general relativity (GR). While GR has proved tremendously effective in understanding the behaviour of gravity on large scales, there are still certain lingering difficulties that have yet to be fully resolved, such as the existence of dark matter and dark energy. One possible answer to these issues is to modify the laws of gravity so that it explains the universe without the addition of adhoc matter and energy. Because neutron stars are highly compact and have a strong gravitational field, they provide a unique testing ground for modified gravity. This means that deviations from GR would be more noticeable near a neutron star than in other regions of

the universe. There are several ways in which modified gravity could affect the behavior of NS. One possibility is that the gravitational force could become stronger or weaker at small scales than predicted by GR. This could affect the structure of NS, altering their density profiles and potentially leading to observable differences in their masses and radii. Another hypothesis is that modified gravity could affect the way in which neutron stars emit radiation, such as X-rays or gamma rays (Capozziello and Lambiase, 2015). For example, if the laws of gravity are different in the vicinity of a neutron star, this could lead to changes in the way in which radiation is emitted, which could be observed by telescopes. Thus the effect of any modifications to GR can be studied in the environment of NS.

## 1.2 Motivation

The study of NS and the fundamental laws of gravity has been a subject of great intrigue and scientific curiosity. These incredibly dense stellar remnants, formed through the cataclysmic collapse of massive stars, hold the key to unraveling the mysteries of the cosmos. While our understanding of NS has advanced significantly, there are still profound questions that remain unanswered, particularly in the realm of gravity and its potential modifications at astrophysical scales. The desire to pursue research in the disciplines of theoretical and observational astrophysics prompted the work in this thesis.

The first motivation behind this thesis is to delve into the fascinating interplay between NS and modified theories of gravity. Traditional models, such as GR, have provided us with a remarkable framework for understanding gravity. However, recent advancements in theoretical physics have sparked a reevaluation of these conventional theories, prompting the exploration of alternative frameworks that can potentially explain unexplained phenomena and address long-standing discrepancies. NS provide an exceptional laboratory for testing the boundaries of GR and exploring the existence of alternative theories. By analyzing their behavior within modified gravity frameworks, we can investigate potential deviations from GR and uncover evidence of new gravitational interactions or modifications that may have profound implications for our understanding of the universe at large. Through a comprehensive analysis of observational data, numerical simulations, and theoretical models, this thesis aims to contribute to the growing body of knowledge on NS and modified gravity. The findings have the potential to deepen our understanding of the complex interplay between gravity and astrophysical phenomena.

The second motivation in this thesis is to contribute to the ongoing efforts in PTA research to detect and study gravitational waves in the nanohertz frequency range. The PTAs conduct long-term observations of pulsars using radio telescopes at regular intervals of every two weeks. The data analysis process involves several steps. First, the raw data from each pulsar, including the times of arrival of the pulses,

is collected and carefully processed to account for various effects such as dispersion caused by the interstellar medium and the Earth's motion. Next, the timing residuals, which are the differences between the observed arrival times and the expected arrival times based on a model, are computed. The timing residuals are then analyzed to search for systematic trends or correlations that may indicate the presence of gravitational waves. This can involve using various statistical techniques and signal processing methods to extract the weak gravitational wave signals from the noise and other astrophysical sources of timing variations. Additionally, efforts are made to carefully model and account for other sources of timing variations, such as intrinsic pulsar irregularities and astrophysical phenomena, to ensure that any detected signals are indeed attributable to gravitational waves. The outcome of this research has the potential to deepen our understanding and enhance our ability to detect and characterize low-frequency gravitational waves.

### **1.3 Aims and Scope**

1. Comparing the NS properties in perturbative and non-perturbative methods of deriving the TOV equations in  $f(R)$  gravity to resolve an ongoing debate surrounding the validity of the methods.
2. Constrain the free parameter of  $f(R)$  gravity model using the inferred value of tidal deformability from the GW170817 binary NS merger.
3. Establish a universal relationship between the free parameter of  $f(R)$  gravity model and NS observables.
4. Demonstrate the effectiveness of timing pulsars in the low-frequency radio waves and its utility in the search for nanohertz gravitational waves.

## Chapter 2

# Equation of State

*"A science is any discipline in which the fool of this generation can go beyond the point reached by the genius of the last generation."* – Max Gluckman

The dense matter in the neutron stars (NS) core may ideally be composed of neutrons, protons, and electrons. We describe the interior of a static NS that is held against gravity by the degeneracy pressure of constituent fermions. A thermodynamic equation linking state variables that characterise the state of matter under a specific set of physical conditions, such as pressure, volume, temperature, or internal energy, is known as an equation of state (EoS).

The EoS of NS can be studied through theoretical modeling. This involves simulating the behavior of matter under extreme conditions within the formalism of GR, using models that take into account the strong force. Broadly speaking, there are two types of EoS models for beta-equilibrated and charge-neutral homogeneous matter in neutron stars: a) relativistic and b) non-relativistic models. Microscopic models, chiral effective field theory models, and phenomenological models are further categories that these models can be grouped into.

A relativistic field theoretical model known as Walecka model ([Walecka, 1974, 1986, 2004](#)) is used to describe NS matter. It is a fully Lorentz invariant phenomenological description of the nuclear many-body problem. The nucleons are treated as point-like particles and are defined by the Dirac equation. The exchange of scalar( $\sigma$ ), vector ( $\omega$ ) mesons mediates nucleon-nucleon interaction in the Walecka model. They carry the long-range attractive and short-range repulsive nuclear forces, respectively. Later, it was expanded to include  $\rho$  meson to account for the system's isospin asymmetry ([Glendenning, 1997](#)).

The Lagrangian density consists of terms related to the free Dirac nucleons of rest mass  $m_B$ , the mesons, and the interaction among them.

$$\begin{aligned} \mathcal{L}_B = & \sum_B \bar{\psi}_B (i\gamma_\mu \partial^\mu - m_B + g_{\sigma B} \sigma - g_{\omega B} \gamma_\mu \omega^\mu - g_{\rho B} \gamma_\mu \boldsymbol{\tau}_B \cdot \boldsymbol{\rho}^\mu) \psi_B \\ & + \frac{1}{2} (\partial_\mu \sigma \partial^\mu \sigma - m_\sigma^2 \sigma^2) - \frac{1}{4} \omega_{\mu\nu} \omega^{\mu\nu} + \frac{1}{2} m_\omega^2 \omega_\mu \omega^\mu - \frac{1}{4} \boldsymbol{\rho}_{\mu\nu} \cdot \boldsymbol{\rho}^{\mu\nu} + \frac{1}{2} m_\rho^2 \boldsymbol{\rho}_\mu \cdot \boldsymbol{\rho}^\mu. \end{aligned} \quad (2.1)$$

Here  $\psi_B$  denotes the Dirac spinor for baryon B,  $\boldsymbol{\tau}_B$  the isospin operator; the field strength tensors for the vector mesons are given by  $\omega^{\mu\nu} = \partial^\mu \omega^\nu - \partial^\nu \omega^\mu$  and  $\boldsymbol{\rho}^{\mu\nu} = \partial^\mu \boldsymbol{\rho}^\nu - \partial^\nu \boldsymbol{\rho}^\mu$ . The coupling strength of the mesons with baryons is specified by  $g_{\alpha B}(\hat{n})$  where  $\alpha = \sigma, \omega$  and  $\rho$ . The couplings are adjusted to nuclear matter properties at saturation density. To represent the behaviour of the matter above saturation density, the  $g_{\alpha B}(\hat{n})$ 's are made density-dependent. The density operator  $\hat{n}$  is given by,  $\hat{n} = \sqrt{\hat{j}_\mu \hat{j}^\mu}$ , where  $\hat{j}_\mu = \bar{\psi} \gamma_\mu \psi$  (Typel, 2005; Typel et al., 2010). This model is known as density-dependent relativistic mean field model (DDRMF). We use EoS with hadronic matter represented by DD2 (Hempel and Schaffner-Bielich, 2010; Typel et al., 2010), FSU2R (Tolos et al., 2017), and SFHx (Steiner et al., 2013) models.

*DD2* – The basic relativistic lagrangian has effective interaction via contributions from  $\sigma, \omega$ , and  $\rho$  mesons without any self-coupling factors. The density-dependent couplings allow the pressure term to rearrange and account for the system's energy-momentum conservation and thermodynamic consistency (Hempel and Schaffner-Bielich, 2010; Banik and Bandyopadhyay, 2002). The DD2 model satisfies the constraints on nuclear symmetry energy and its slope parameter, as well as the incompressibility from the nuclear physics experiments (Char and Banik, 2014). As emphasised in Fortin et al. (2016), proper core-crust matching is critical to avoiding uncertainty in the macroscopic properties of stars. The DD2 EoS uses the same lagrangian density to describe both the low-density crust and the high-density core, allowing for a smooth transition between the two.

*FSU2R* – The nucleonic EoS is derived as a new parameterization of the nonlinear realisation of the RMF model. Beginning with the current RMF parameter set FSU2 (Chen and Piekarewicz, 2014), if the pressure of NS matter in the vicinity of saturation is reduced, it allows for smaller stellar radii while maintaining nuclear matter and finite nuclei properties. Furthermore, the pressure at high densities are preserved while remaining consistent with high-energy heavy-ion collisions findings and sufficiently stiff to support  $2M_\odot$  NS (Danielewicz et al., 2002).

*SFHx* – The Lagrangian is based on the interchange of isoscalar-scalar  $\sigma$ , isoscalar-vector  $\omega$ , and isovector-vector  $\rho$ -mesons (Steiner et al., 2013). Fits from the experimental data are required to estimate the free parameters in the Lagrangian, the masses of the nucleons and mesons, and their coupling

strengths. It is based on an interpolation of two parameter sets, TM1 and TM2 (Sugahara and Toki, 1994), which were fitted to binding energies and charge radii of light (TM2) and heavy nuclei, respectively (TM1). To have a fair description of nuclei throughout the full mass number range, the coupling parameters  $g_i$  of the set TMA are chosen to be mass-number dependent of the form  $g_i = a_i + b_i/A^{0.4}$ , with  $a_i$  and  $b_i$  being constants. The couplings become constants for uniform nuclear matter and are given by  $a_i$ .

The NS's high-density core is also believed to be filled by strange baryons and even quark matter under extreme pressure. Strange matter stars could be more stable than nucleon-only stars. The emergence of a new degree of freedom relaxes the EoS and supports a star that is less massive and less compact than those composed simply of nucleons. We consider three strange EoS consisting of i)  $\Lambda$  hyperons ( $BHB\Lambda\phi$ ) (Banik *et al.*, 2014), ii)  $\Lambda$  hyperons and  $K^-$  mesons ( $BHB\Lambda\phi K^-$ ) (Malik *et al.*, 2021), iii) FSUQ Chen and Piekarewicz (2015) and 2 flavor quark matter (DD2-FRG) (Otto *et al.*, 2020) in addition to the nucleons. The DD2 EoS for hadronic matter serves as the foundation for all three hybrid EoS. There is an additional  $\phi$  meson which mediates the hyperon-hyperon interaction. When the  $\Lambda$  hyperon's in-medium chemical potential matches that of the neutron, it is populated. The density-dependent  $\Lambda$ -vector meson hyperon couplings are derived from the quark model's SU(6) symmetry. (Dover, 1984; Schaffner and Mishustin, 1996) i.e.,  $g_{\omega\Lambda} = \frac{2}{3}g_{\omega N}$ ,  $g_{\rho\Lambda} = 0$ ,  $g_{\phi\Lambda} = -\frac{\sqrt{2}}{3}g_{\omega N}$ .

$BHB\Lambda\phi$  – The scalar meson coupling to  $\Lambda$  hyperons is determined by their potential depth (–30MeV) in normal nuclear matter, which is obtained from experimental data of hypernuclei single particle spectra. Additional octet baryons are not considered mostly because of the uncertainty in their experimental results.

$BHB\Lambda\phi K^-$  – The anti-kaon nucleon interaction is treated similarly to the nucleon-nucleon interaction. When the in-medium energy of the  $K^-$  condensate equals the chemical potential given by  $\mu_{K^-} = \mu_n - \mu_p$ , it emerges in the system. The kaon-meson couplings are considered as constants that do not change with density. They are calculated using the quark model and the iso-spin counting rule  $g_{\omega K} = \frac{1}{3}g_{\omega N}$  and  $g_{\rho K} = g_{\rho N}$  (Schaffner and Mishustin, 1996; Banik and Bandyopadhyay, 2001). The scalar coupling constant is calculated from the real component of  $K^-$  optical potential at saturation density, which we assume to be –120 MeV.

FSUQ – FSUQ EoS has quarks on top of the nucleonic FSUGarnet EoS. The parameters of FSUGarnet are determined by fitting model predictions to experimental data, based on genuine physical observables that can be either measured in the laboratory or extracted from observation (Chen and Piekarewicz, 2015). The EoS is stiff, the resulting values for the symmetry energy and its slope at saturation density



**Table 2.1:** For the EoS model used in the work, namely SFHx (Steiner *et al.*, 2013), FSU2R (Tolos *et al.*, 2017), FSUQ (Chen and Piekarewicz, 2015), DD2 (Hempel and Schaffner-Bielich, 2010; Typel *et al.*, 2010), BHB $\Lambda\phi$  (Banik *et al.*, 2014), BHB $\Lambda\phi K^-$  (Malik *et al.*, 2021), and DD2-FRG (Otto *et al.*, 2020), we compile the nuclear matter saturation properties.

EoS	$n_B^0$ ( $fm^{-3}$ )	B/A (MeV)	$K_0$ (MeV)	$Q_0$ (MeV)	$J_0$ (MeV)	$L_0$ (MeV)
SFHx	0.160	-16.16	239	-457	28.7	23.2
FSU2R	0.151	-16.28	238	-135	30.7	47.0
FSUQ	0.153	-16.23	229.5	-	30.92	51.0
DD2	0.149	-16.02	243	169	31.7	55.0
DD2-FRG	0.149	-16.02	243	169.0	31.7	55.0
BHB $\Lambda\phi$	0.149	-16.02	242.7	168.7	31.67	55.03
BHB $\Lambda\phi K^-$	0.149	-16.02	242.7	168.7	31.67	55.03

are  $30.92 \pm 0.47$  and  $51.0 \pm 1.5$  MeV, respectively. These are well within the acceptable range.

*DD2-FRG* – The EoS for quark matter is constructed within a model based on the underlying chiral symmetry breaking of QCD. The functional renormalization group (FRG) was used to generate this non-perturbative two- and three-flavored quark model (Otto *et al.*, 2020).

In figure 2.1, we plot the pressure versus the baryonic number density for the EoS used in this study: DD2 (black, right triangle), DD2-FRG (green, left triangle) BHB $\Lambda\phi$  (golden, diamond), BHB $\Lambda\phi K^-$  (magenta, square), FSU2R (blue, circle), FSUQ (turquoise, star), and SFHx (orange, pentagon). These EoS satisfy the maximum mass and radius constraints from observations (Riley *et al.*, 2021, 2019; Miller *et al.*, 2019, 2021). The maximum hybrid star mass for the two-flavor model is roughly  $2.1M_\odot$ , which is consistent with current mass data, however the strange quark model does not meet the mass limit. As a result, we considered the two-flavored DD2-FRG EoS in our analysis.

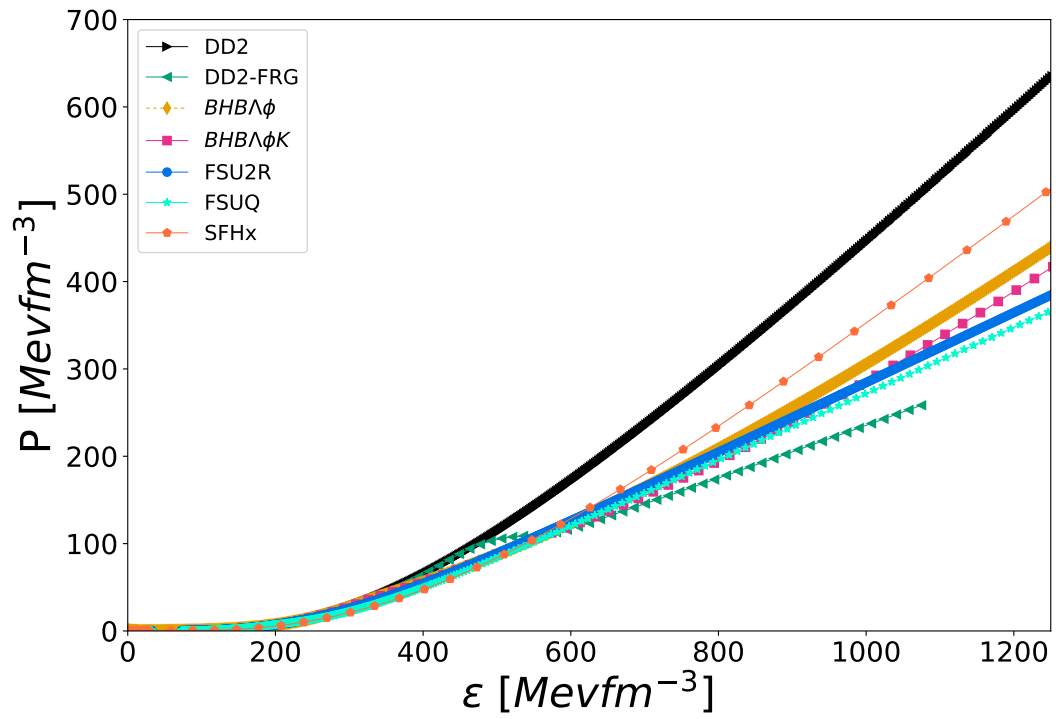


**Figure 2.1:** a) Pressure versus energy density curve of the hadronic, strange, and quark EoS under study.

## Chapter 3

# Modified Gravity Theories

*"The great tragedy of science – the slaying of a beautiful hypothesis by an ugly fact."* – Thomas Huxley

### 3.1 Introduction

General relativity (GR) ([Einstein, 1916](#)) is widely recognized as an accepted theory for explaining the nature of gravity. It substitutes Newtonian concept of gravity as a force with a description of geometric characteristics of spacetime. It has been put through rigorous testing within the solar system and the larger universe over the past century, consistently demonstrating its remarkable success. In the weak field regime, it is in agreement with a myriad of solar system gravity precision tests, including gravitational lensing of light from distant background stars, Mercury's anomalous perihelion precession, gravitational redshift, the Shapiro time-delay effect, and Lunar laser experiments ([Will, 2014](#)). In the strong field regime, the predictions of GR involves changes in the orbital parameters of binary pulsars due to gravitational wave emission and black hole (BH) - neutron star (NS) or BH-NS mergers. These binary mergers were successfully observed opening a new window into the study and understanding of gravity ([Abbott \*et al.\*, 2016](#)).

The findings of observational cosmology in the past few decades indicate that the universe has gone through two phases of cosmic acceleration called inflation ([Kazanas, 1980](#); [Starobinsky, 1980](#); [Guth, 1981](#)) and late-time cosmic acceleration ([Sakharov, 1991](#); [Huterer and Turner, 1999](#); [Sahni and Starobinsky, 2000](#)). Our current understanding of ordinary matter is insufficient to describe these two scenarios of expansion. Some form of negative energy is required to explain the universe's accelerating expansion. The unknown component causing this late-time cosmic acceleration is known as dark energy, and its presence has been established by a number of observations; such as, supernova Ia ([Riess \*et al.\*,](#)

1998; Perlmutter *et al.*, 1999) baryon acoustic oscillations (Eisenstein *et al.*, 2005; Percival *et al.*, 2007), and Cosmic Microwave Background (Spergel *et al.*, 2003, 2007). Einstein himself, in his later years, introduced the cosmological constant  $\Lambda$  (Einstein, 1931) in to the field equations. However, if we assume that  $\Lambda$  originates from the vacuum energy of the quantum field theory, there is a significant discrepancy between the observed value and the field theoretical calculation of  $\Lambda$  (Weinberg, 1989). A scalar field  $\phi$  with a slowly evolving potential can be a contender for both inflation and dark energy.

On the other hand, our understanding of the fundamental interactions, such as strong, electromagnetic, and weak, comes from the standard model of particle physics, which is quantum in nature. Whereas gravitational interaction, though fundamental, is not described in the framework of quantum mechanics. The conceptual challenges in quantizing Einstein's theory (Birrell and Davies, 1982), as well as the astronomical observations of accelerated expansion of the universe, suggests that GR might need to be modified.

There are many ways one can modify GR. The following are a few of the several modified gravity theories that have been put forth:

- **Scalar-Tensor Theories** (Brans and Dicke, 1961; Faraoni, 1999): According to these theories, there is a scalar field that mediates the gravitational interaction. The value of this scalar field then determines the strength of gravity. Among these theories is the Brans-Dicke theory, which served as a forerunner to many modern scalar-tensor theories. The  $f(R)$  gravity is a type of scalar-tensor theories which modifies GR in which it replaces the Einstein-Hilbert action with a function of the Ricci scalar curvature. The modification is introduced to explain the observed acceleration of the universe's expansion without the need for dark energy.
- **Vector-Tensor Theories** (Lagos *et al.*, 2016): These theories propose the existence of a vector field that mediates the gravitational interaction. The vector field may affect the propagation of gravitational waves and can lead to deviations from GR. These theories are not as well-developed as scalar-tensor theories.
- **Modified Newtonian Dynamics (MOND)** (Milgrom, 1983): MOND proposes that the behavior of gravity changes when the gravitational acceleration is very small, such as in the outskirts of galaxies. This theory has been successful in explaining the rotation curves of galaxies but has faced challenges in explaining other observations. Later, Jacob Bekenstein in 2004 proposed Tensor-Vector-Scalar Theories as a relativistic generalization of MOND paradigm.
- **Tensor-Vector-Scalar Theories** (Bekenstein and Sanders, 2006): These theories propose the

existence of all three types of fields: a tensor field, a vector field, and a scalar field. These theories attempt to unify the three fields into a single framework.

- Emergent Gravity (Verlinde, 2011): Emergent gravity proposes that gravity arises from the collective behavior of microscopic degrees of freedom, rather than being a fundamental force of nature. This theory is still in its infancy, and more research is needed to test its validity.

Despite the fact that these changes are well-motivated and consistent, the plethora of ideas and possibilities has resulted in the lack of a single compelling hypothesis that might really define gravity. Any large-scale modification of gravity must reconcile with the local physical constraints by undergoing solar system testing and laboratory experiments in order to be a viable model of gravity. The majority of these models have been subjected to solar system testing where the gravitational field is significantly weak, confirming the accuracy of GR on the weak gravitational background. Any coherent gravity theory, whether classical or modified should be equally relevant to the strong gravity regime. Compact objects like NS provide an excellent platform for studying the behaviour of strong gravity. They provide a powerful probe of the GR in the strong-field domain and open up new avenues for exploring and constraining modified gravity theories.

The simplest of these modifications are  $f(R)$  theories, where  $f(R)$  has the higher order extensions of the Ricci scalar (Sotiriou and Faraoni, 2010). To study NS in  $f(R)$  theory of gravity, one can derive a set of modified Tolman-Oppenheimer-Volkoff (TOV) equations that describe a static, spherically symmetric mass distribution under hydrostatic equilibrium. Due to the presence of higher order curvature terms in the action, it is not trivial to derive the TOV equations. There are two methods proposed to tackle this problem: a) perturbative approach (Arapoğlu *et al.*, 2011; Astashenok, 2014) and b) non-perturbative approach (Yazadjiev *et al.*, 2014; Astashenok *et al.*, 2015; Nobleson *et al.*, 2021). In this chapter, we first start with the TOV in the framework of GR and subsequently describe the TOV in these modified gravity approaches.

## 3.2 Formalism

### 3.2.1 NS in GR

NS are relativistic objects and their structure calculations are carried out in a GR framework. The interior of a spherically symmetric static star is considered as a perfect fluid and its Schwarzschild metric is represented by the line element:

$$ds^2 = -e^{2\phi(r)} dt^2 + e^{2\lambda(r)} dr^2 + r^2(d\theta^2 + \sin^2\theta d\vartheta^2). \quad (3.1)$$

In hydrostatic equilibrium, the structure of a spherically symmetric, static relativistic NS is determined by the Tolman-Oppenheimer-Volkoff (TOV) equations (Tolman, 1939; Oppenheimer and Volkoff, 1939). These ordinary differential equations are (in the units of  $G = c = 1$ ):

$$\begin{aligned}\frac{dm}{dr} &= 4\pi\rho r^2 \\ \frac{dp}{dr} &= -(\rho + p) \left[ \frac{m + 4\pi r^3 p}{r(r - 2m)} \right]\end{aligned}\quad (3.2)$$

where  $\rho$  is energy density,  $p$  is pressure, both in the fluid frame. Given a barotropic EoS, i.e., the EoS can be written as  $\rho = \rho(n_B)$  and  $p = p(n_B)$ , where  $n_B$  is the baryon number density in the fluid frame the stellar structure can be computed by numerically integrating Eqs. 3.2 from the centre at  $r = 0$  out to the star surface at  $r = R$ . The boundary conditions on the surface ( $r = R$ ) is  $p = 0$ , whereas at the center ( $r = 0$ ) is  $p = p_c(\rho_c)$  and  $m = 0$ .  $M$  is the gravitational mass inside radius  $r$  of a sphere about the origin and is given by  $M(r) = 4\pi \int_0^R \rho(r)r^2 dr$ .

### 3.2.2 NS in $f(R)$ Using Perturbative Method

Perturbative constraints allows us to investigate modified gravity phenomenologies while preserving key consistency conditions, such as, gauge invariance, the assumption that we are approximating a fundamentally second order field theory, and stress-energy conservation.

To derive the modified-TOV equations, let us consider the following action (in the units of  $G = c = 1$ ):

$$S = \frac{1}{16\pi} \int d^4x \sqrt{-g} f(R) + S_{matter}\quad (3.3)$$

where  $g$  is the determinant of the metric  $g_{\mu\nu}$  and  $S_{matter}$  is the action of the standard perfect fluid matter. For compact objects, the metric can be assumed to be spherically symmetric as described in eqn 3.1. By varying the action with respect to  $g_{\mu\nu}$ , we can derive the modified-TOV equations. The full derivation of this formalism can be found in Arapoğlu *et al.* (2011); Astashenok (2014).

In the framework of perturbative approach,  $f(R)$  is expressed as  $f(R) = R + \alpha h(R) + \mathcal{O}(\alpha^2)$ , where  $h(R)$  is an arbitrary function of  $R$ ,  $\alpha$  is the free parameter for perturbation, and  $\mathcal{O}(\alpha^2)$  denotes the possible higher-order corrections. Here, we have considered  $h(R) = R^2$ ,  $R$  being the Ricci curvature scalar. The quantities from the EoS, i.e., pressure and energy density are represented as zeroth order  $p^{(0)}$  and  $\rho^{(0)}$ , the corresponding calculated mass in GR is  $m^{(0)}$ . The Ricci curvature scalar has to be evaluated

at  $\mathcal{O}(1)$  order, i.e.,

$$R = R^{(0)} = 8\pi(\rho^{(0)} - 3p^{(0)}). \quad (3.4)$$

Because its value is set by this relation, we do not consider the curvature scalar to be an additional degree of freedom. The density, pressure, mass, and curvature of a perturbative solution can be expanded as

$$\begin{aligned} p &= p^{(0)} + \alpha p^{(1)} + \dots \\ \rho &= \rho^{(0)} + \alpha \rho^{(1)} + \dots \\ m &= m^{(0)} + \alpha m^{(1)} + \dots \\ R &= R^{(0)} + \alpha R^{(1)} + \dots \end{aligned} \quad (3.5)$$

The modified TOV equations in the perturbative method are as follows:

$$\begin{aligned} \frac{dm}{dr} &= 4\pi\rho r^2 - \alpha r^2 \left[ 8\pi\rho^{(0)}R - \frac{R^2}{4} \right] + \alpha \left[ (2r - 3m^{(0)} - 4\pi\rho^{(0)}r^3) \frac{dR}{dr} \right] \\ &+ \alpha \left[ r \left( r - 2m^{(0)} \right) \frac{d^2R}{dr^2} \right] \end{aligned} \quad (3.6)$$

$$\begin{aligned} \frac{dp}{dr} &= \frac{\rho + p}{r - 2m} \left[ 4\pi r^2 p + \frac{m}{r} - \alpha r^2 \left( 8\pi p^{(0)}R - \frac{R^2}{4} \right) \right] \\ &- 2\alpha \left( r - 3m^{(0)} + 2\pi p^{(0)}r^3 \right) \frac{dR}{dr} \end{aligned} \quad (3.7)$$

As in GR, the modified TOV eqs. 3.6, and 3.7, can be solved numerically to obtain mass and radius of the NS. We note that perturbation expansion parameter  $\alpha$  introduces a new scale into the theory. Further, by choosing a realistic EoS, we compute mass-radius relation for various values of  $\alpha$ , thereby allowing to place a bound on  $\alpha$  for perturbative  $f(R)$  gravity model:  $f(R) = R + \alpha R^2$ .

### 3.2.3 NS in $f(R)$ Using Non-Perturbative Method

In the non-perturbative method, we consider the same action as described in eqn 3.3. To make the  $f(R)$  theory free of tachyonic instabilities and appearance of ghosts (Sotiriou and Faraoni, 2010; De Felice and Tsujikawa, 2010; Babichev and Langlois, 2010), the following conditions are imposed.

$$\frac{df}{dR} > 0; \quad \frac{d^2f}{dR^2} \geq 0 \quad (3.8)$$

It is well established that the  $f(R)$  theories are analogous to the Brans-Dicke scalar-tensor theory with  $\omega_{BD} = 0$  and with a potential for the scalar field (O'Hanlon, 1972; Teyssandier and Tourenç, 1983). A new field  $\Phi$  is introduced such that the scalar field  $\varphi = \frac{\sqrt{3}}{2} \ln \Phi$ . For  $f(R) = R + \alpha R^2$ , the Brans-Dicke potential is given by

$$U(\Phi) = \frac{1}{4\alpha} (\Phi - 1)^2 \quad (3.9)$$

which corresponds to a massive scalar field which is a function of the free parameter  $\alpha$  with mass  $m_\Phi = 1/\sqrt{6\alpha}$ . Here we consider only the values of  $\alpha$  which satisfies the condition  $d^2 f/dR^2 \geq 0$ .

The action in eqn 3.3 can be re-written as

$$S = \frac{1}{16\pi} \int d^4x \sqrt{-g} [\Phi R - U(\Phi)] + S_m \quad (3.10)$$

From a mathematical and numerical perspective, it is more convenient to study the field equations in the Einstein frame. An Einstein frame can be defined for the new scalar field  $\varphi$ , and the new metric  $g_{\mu\nu}^*$  is given by

$$g_{\mu\nu}^* = \Phi g_{\mu\nu} = A^{-2}(\varphi) g_{\mu\nu} \quad (3.11)$$

with  $A^2(\varphi) = \Phi^{-1}(\varphi) = \exp(-2\varphi/\sqrt{3})$ .

The Einstein frame action takes the following form:

$$S = \frac{1}{16\pi} \int d^4x \sqrt{-g^*} [R^* - 2g^{*\mu\nu} \partial_\mu \varphi \partial_\nu \varphi - V(\varphi)] + S_m \quad (3.12)$$

where  $R^*$  is the Ricci scalar curvature with respect to the Einstein frame metric  $g^{*\mu\nu}$  and  $V(\varphi) = A^4(\varphi)U(\Phi(\varphi))$ . The explicit form of potential in the Einstein frame for R-squared gravity is  $V(\varphi) = (1 - \exp(-2\varphi/\sqrt{3}))^2/4\alpha$ . In comparison to the Jordan frame, the Einstein frame's field equations are much simpler. The appearance of direct interaction between the scalar field  $\varphi$  and the matter fields in Einstein frame comes at a cost for simplifying the action and the field equations in this frame. By taking variation with respect to the metric  $g_{\mu\nu}^*$  and the scalar field  $\varphi$ , the field equations in the Einstein frame are derived. The final quantities that we obtain have to be transformed back to the physical Jordan frame. In addition, the EoS of the nuclear matter that we use is also in the Jordan frame (Yazadjiev *et al.*, 2014).

$$G_{\mu\nu}^* = 8\pi T_{\mu\nu}^* + 2\partial_\mu \varphi \partial_\nu \varphi - g_{\mu\nu}^* g^{*\epsilon\delta} \partial_\epsilon \varphi \partial_\delta \varphi - \frac{1}{2} V(\varphi) g_{\mu\nu}^* \quad (3.13)$$



$$\nabla_{\mu}^{*} \nabla^{*\mu} \varphi - \frac{1}{4} \frac{dV(\varphi)}{d\varphi} = -4\pi\beta(\varphi)T^{*} \quad (3.14)$$

where

$$\beta(\varphi) = \frac{d \ln A(\varphi)}{d\varphi} = -\frac{1}{\sqrt{3}} \quad (3.15)$$

The Einstein frame energy-momentum tensor  $T_{\mu\nu}^{*}$  is related to the Jordan frame energy-momentum tensor  $T_{\mu\nu}$  via  $T_{\mu\nu}^{*} = A^2(\varphi)T_{\mu\nu}$ . In the case of a perfect fluid, the energy density, the pressure and the 4-velocity in the two frames are related via the formulae

$$\rho_{*} = A^4(\varphi)\rho, \quad p_{*} = A^4(\varphi)p, \quad u_{\mu}^{*} = A^{-1}(\varphi)u_{\mu}. \quad (3.16)$$

The contracted Bianchi identities give the following conservation law for the Einstein frame energy-momentum tensor

$$\nabla_{\mu}^{*} T_{\nu}^{*\mu} = \beta(\varphi)T^{*} \nabla_{\nu}^{*} \varphi \quad (3.17)$$

We consider static and spherically symmetric spacetime described by the Einstein frame metric as defined in eqn 3.1 We consider the matter source to be a perfect fluid and also that the perfect fluid and the scalar field are static and spherically symmetric. With these conditions imposed, the dimensionally reduced field equations are (Yazadjiev *et al.*, 2014; Astashenok *et al.*, 2015)

$$\frac{1}{r^2} \frac{d}{dr} \left[ r \left( 1 - e^{-2\lambda} \right) \right] = 8\pi\rho A^4(\varphi) + e^{-2\lambda} \left( \frac{d\varphi}{dr} \right)^2 + \frac{1}{2}V(\varphi) \quad (3.18)$$

$$\frac{2}{r} e^{-2\lambda} \frac{d\phi}{dr} - \frac{1}{r^2} \left( 1 - e^{-2\lambda} \right) = 8\pi p A^4(\varphi) + e^{-2\lambda} \left( \frac{d\varphi}{dr} \right)^2 - \frac{1}{2}V(\varphi) \quad (3.19)$$

$$\frac{d^2\varphi}{dr^2} + \left( \frac{d\phi}{dr} - \frac{d\lambda}{dr} + \frac{2}{r} \right) \frac{d\varphi}{dr} = 4\pi\beta(\varphi)A^4(\varphi)(\rho - 3p)e^{2\lambda} + \frac{1}{4} \frac{dV(\varphi)}{d\varphi} e^{2\lambda} \quad (3.20)$$

$$\frac{dp}{dr} = -(p + \rho) \left[ \frac{d\phi}{dr} + \beta(\varphi) \frac{d\varphi}{dr} \right] \quad (3.21)$$

For the purposes of arriving at a numerical solution, the above equations can be further reduced to the following:

$$\frac{d\lambda}{dr} = e^{2\lambda} \left[ 4\pi\rho r A^4 + \frac{r e^{-2\lambda}}{2} \left( \frac{d\varphi}{dr} \right)^2 + \frac{r(1-A^2)^2}{16\alpha} - \frac{(1-e^{-2\lambda})}{2r} \right] \quad (3.22)$$

$$\frac{d\phi}{dr} = e^{2\lambda} \left[ 4\pi p r A^4 + \frac{r e^{-2\lambda}}{2} \left( \frac{d\varphi}{dr} \right)^2 - \frac{r(1-A^2)^2}{16\alpha} + \frac{(1-e^{-2\lambda})}{2r} \right] \quad (3.23)$$

$$\frac{d^2\varphi}{dr^2} = e^{2\lambda} \left[ \frac{A^2(1-A^2)}{4\sqrt{3}\alpha} - \frac{4\pi A^4(\rho-3p)}{\sqrt{3}} \right] - \frac{d\varphi}{dr} \left( \frac{d\phi}{dr} - \frac{d\lambda}{dr} + \frac{2}{r} \right) \quad (3.24)$$

$$\frac{dp}{dr} = -(p+\rho) \left[ \frac{d\phi}{dr} - \frac{1}{\sqrt{3}} \left( \frac{d\varphi}{dr} \right) \right] \quad (3.25)$$

The Jordan frame quantities  $\rho$  and  $p$  are naturally connected via the EoS of the neutron star matter  $p = p(\rho)$ . Furthermore, we should impose the standard boundary conditions – regularity of the scalar field  $\varphi$  at the star's center and asymptotic flatness at infinity. The equations describing the spacetime metric and the scalar field outside the neutron star are obtained by setting  $\rho = p = 0$ . In order to solve our systems of differential equations for the interior and the exterior of the neutron star, we should provide the EoS for the neutron star matter  $p = p(\rho)$  and impose the boundary conditions together with the natural Einstein frame boundary conditions at the center of the star which are as follows:

$$\rho(0) = \rho_c, \quad \lambda(0) = 0, \quad \frac{d\varphi}{dr}(0) = 0 \quad (3.26)$$

At infinity,

$$\lim_{r \rightarrow \infty} \phi(r) = 0, \quad \lim_{r \rightarrow \infty} \varphi(r) = 0 \quad (3.27)$$

To get the neutron star mass and radius, we need to solve numerically the equations (3.22, 3.23 and 3.25) together with the boundary conditions equations (3.26) - (3.27) from center to surface of the star and then surface to infinity. In order to integrate those coupled differential equations from center of the star, we

need to set the value of  $\phi$  for each central density of the star at the centre so that it decays exponentially and reaches zero at infinity. The behaviour of  $\phi$  with integrating radius can be seen in figure 5 of (Astashenok *et al.*, 2015). The radius of the star is calculated from the requirement of pressure vanishing at the stellar surface and the mass is taken from the asymptotic expansion of the metric functions at infinity. In Einstein frame, the star mass  $m(r)$  can be defined according to the relation  $e^{-2\lambda} = 1 - \frac{2m}{r}$ . The requirement of asymptotic flatness fixes the constraints on the scalar curvature and the mass parameter as,

$$\lim_{r \rightarrow \infty} R(r) = 0, \quad \lim_{r \rightarrow \infty} m(r) = 0$$

It is important to note that for the considered R-squared gravity the mass in the Einstein and the Jordan frame coincide, while the physical Jordan frame radius of the star  $R_S$  is connected to the Einstein frame one  $r_s$  through the following relation

$$R_S = A(\varphi(r_s))r_s \quad (3.28)$$

The dimensions of the parameter  $\alpha$  is in terms of  $r_g^2$ , where  $r_g = 1.47664$  km corresponds to one solar mass. The  $m(r)$  profile for inside and outside star for both the Einstein and the Jordan frame can be seen in figure 4 of Astashenok *et al.* (2015).

### 3.2.4 Tidal Love number

A NS, like any other extended object, is tidally deformed by an external tidal field. Tidal deformability quantifies the star's quadrupole deformation in response to a perturbing companion star (Hinderer, 2008). The NS' induced quadrupole moment influences the system's binding energy and increases the rate of gravitational wave emission (Peters and Mathews, 1963; Blanchet, 2014). Tidal deformability has been utilised to study the internal structure of NS and has played a major part in the study of merging NS using gravitational waves. The tidal Love number specifies the degree of simplicity or complexity of an NS' deformation away from sphericity (Hinderer, 2008; Yagi and Yunes, 2013). For simplicity, let us only consider quadrupole moments  $Q_{ij}$ . This is reasonable if the two binary neutron stars stay sufficiently apart. In such a scenario, the quadrupole moment ( $l = 2$ ) prevails over the multiple moments.  $Q_{ij}$  is connected to the external tidal field  $\mathcal{E}_{ij}$  as

$$Q_{ij} = -\Lambda \mathcal{E}_{ij}, \quad (3.29)$$

where  $\Lambda$  is the tidal deformability of the NS and it is related to the TLN  $k_2$  as

$$k_2 = \frac{3}{2} \Lambda R^{-5}. \quad (3.30)$$

Consider a static, spherically symmetric star in R-squared gravity. The stationary perturbations of the metric can be separated into magnetic/axial and electric/polar types. In this study, we calculate only the tidal Love number for the polar type and its corresponding tidal deformability. Even though the absolute value of the axial Tidal Love Number can increase dramatically in R-squared gravity (Yazadjiev *et al.*, 2014), recent estimates indicate that they have no observable impact on the gravitational wave signal, even for the next generation of gravitational wave detectors (Jiménez Forteza *et al.*, 2018).

### Polar type

The electric/polar perturbations of the perturbed Einstein frame metric in the Regge-Wheeler gauge can be written in the form (Regge and Wheeler, 1957)

$$H_{\mu\nu}^{polar} = \begin{bmatrix} -e^{2\psi_0} H_0(r) & H_1(r) & 0 & 0 \\ H_1(r) & e^{2\lambda_0} H_2(r) & 0 & 0 \\ 0 & 0 & K(r)r^2 & 0 \\ 0 & 0 & 0 & K(r)r^2 \sin^2\theta \end{bmatrix} \times Y_{lm}(\theta, \phi) \quad (3.31)$$

where  $Y_{lm}(\theta, \phi)$  are the spherical harmonics. The perturbations of the scalar field, energy density and the pressure can be decomposed into  $\delta\varphi = \delta\tilde{\varphi}(r)Y_{lm}(\theta, \phi)$ ,  $\delta\rho^* = \delta\tilde{\rho}(r)Y_{lm}(\theta, \phi)$ ,  $\delta p^* = \delta\tilde{p}(r)Y_{lm}(\theta, \phi)$ .

After perturbing the Einstein frame field equations of the  $f(R)$  gravity coupled to a perfect fluid, it can be shown that  $H_0 = -H_2$  and  $H_1 = 0$  and  $\delta\tilde{\rho}(r)$ ,  $\delta\tilde{p}(r)$ , and  $K$  can be written as a function of  $H_0$  and  $\tilde{\varphi}$ . We also obtain the following two equations for  $H_0 = -H_2 = H$  and  $\tilde{\varphi}$  governing the stationary perturbations of the static and spherically symmetric stars in  $f(R)$  gravity:

$$\begin{aligned} & \frac{d^2 H}{dr^2} + \left\{ \frac{2}{r} + e^{2\lambda_0} K \right\} \frac{dH}{dr} + e^{2\lambda_0} \left\{ -\frac{l(l+1)}{r^2} + 4\pi L - 4\psi_0'^2 e^{-2\lambda_0} \right\} H \\ & + e^{2\lambda_0} \left\{ -4\varphi_0' r M - \frac{16\pi}{\sqrt{3}} N \right\} \delta\tilde{\varphi} = 0 \end{aligned} \quad (3.32)$$

where

$$\begin{aligned}
 K &= \left[ \frac{1 - e^{-2\lambda_0}}{r} + 4\pi r(p_0^* - \rho_0^*) - \frac{r}{2}V(\varphi_0) \right] \\
 L &= \left[ 9p_0^* + 5\rho_0^* + \frac{\rho_0^* + p_0^*}{\tilde{c}_s^2} - \frac{1}{4\pi}V(\varphi_0) \right] \\
 M &= \left[ \frac{1 - e^{-2\lambda_0}}{r} + 8\pi p_0^* + e^{-2\lambda_0}\varphi_0'^2 - \frac{1}{2}V(\varphi_0) \right] \\
 N &= \left[ (\rho_0^* - 3p_0^*) + (\rho_0^* + p_0^*)\frac{1 - 3\tilde{c}_s^2}{2\tilde{c}_s^2} + V'(\varphi_0) \right]
 \end{aligned}$$

$$\begin{aligned}
 &\frac{d^2\delta\tilde{\varphi}}{dr^2} + \left( \psi_0' - \lambda_0' + \frac{2}{r} \right) \frac{d\delta\tilde{\varphi}}{dr} \\
 &- e^{2\lambda_0} \left\{ \frac{l(l+1)}{r^2} + e^{-2\lambda_0}4\varphi_0'^2 + \frac{1}{4}V''(\varphi_0) - \frac{8\pi}{3}P \right\} \delta\tilde{\varphi} \\
 &+ e^{2\lambda_0} \left\{ -2\psi_0'\varphi_0'e^{-2\lambda_0} - \frac{4\pi}{\sqrt{3}}Q + \frac{1}{4}V_0'(\varphi_0) \right\} H = 0
 \end{aligned} \tag{3.33}$$

where

$$\begin{aligned}
 P &= \left[ -2(\rho_0^* - 3p_0^*) + (\rho_0^* + p_0^*)\frac{1 - 3\tilde{c}_s^2}{2\tilde{c}_s^2} \right] \\
 Q &= \left[ (\rho_0^* - 3p_0^*) + (\rho_0^* + p_0^*)\frac{1 - 3\tilde{c}_s^2}{2\tilde{c}_s^2} \right]
 \end{aligned}$$

Here  $\lambda_0$ ,  $\psi_0$ ,  $\varphi_0$ ,  $p_0$  and  $\rho_0$  are the corresponding unperturbed variables taken from the background neutron star solutions and  $\tilde{c}_s$  is the Jordan frame speed of sound defined as  $\tilde{c}_s^2 = \partial p / \partial \rho$ .

As discussed above, the scalar field mass of  $f(R)$  gravity is nonzero which implies that both the background scalar field  $\varphi_0$  and its perturbation  $\delta\tilde{\varphi}$  drop off exponentially at infinity. This implies that the corresponding scalar field tidal Love number is zero. The asymptotic behaviour of  $H$  at large  $r$  is

$$H = \frac{c_1}{r^{l+1}} + \mathcal{O}\left(\frac{1}{r^{l+2}}\right) + c_2 r^l + \mathcal{O}(r^{l-1}). \tag{3.34}$$

The tidal Love number  $k_2$  is connected to the coefficients  $c_1$  and  $c_2$  in the above equation as follows:

$$k_l^{polar} = \frac{1}{2R_S^{2l+1}} \frac{c_1}{c_2} \tag{3.35}$$

In pure GR, the ratio  $c_1/c_2$  is usually determined by matching at the stellar surface the numerical solution

of  $H$  from the interior of the neutron star to the analytical solution exterior to it. This approach cannot be applied to the case here since the equations for  $H$  and  $\delta\tilde{\varphi}$  are coupled and, in general, there exists no analytical solution outside the star. Since we know that the scalar field is massive, the problem is simplified. Since the scalar field and its perturbation die out exponentially at distances larger than the Compton wavelength of the scalar field  $\lambda_\varphi = 2\pi/m_\varphi = 2\pi\sqrt{6a}$ , the analytical solution of GR can be used. The inner and outer solutions are matched at a radius  $r_{match}$  where the scalar field and its perturbation are negligible rather than at the stellar surface. Since  $r_{match}$  is connected to the Compton wavelength of the scalar field,  $r_{match}$  is not a constant but a function of the parameter  $a$ . For  $l = 2$ , we obtain

$$k_2^{polar} = \frac{8C_1^5}{5}(1 - 2C)^2 [2 + 2C(y - 1) - y] \times \left\{ 2C [6 - 3y + 3C(5y - 8)] + 4C^3 [13 - 11y + C(3y - 2) + 2C^2(1 + y)] + 3(1 - 2C)^2 [2 - y + 2C(y - 1)] \log(1 - 2C) \right\}^{-1} \quad (3.36)$$

Here  $y = rH'/H$ ,  $C_1 = M/R_S$  is the compactness of the star and  $C = M/r_{match}$ . The value of  $y$  is calculated from the numerical solution of equations 3.32 and 3.33 from  $r = 0$  to  $r = r_{match}$ .

To compute this polar tidal love number numerically, we need to solve the simultaneous second order differential equations 3.32 and 3.33 with some initial values for  $H$ ,  $dH/dr$ ,  $\delta\varphi$  and  $d\delta\varphi/dr$  at the center of the neutron star. We have used  $\chi^2$  minimization method to arrive at values for  $\delta\varphi$  at the center of the star such that the perturbation exponentially decays to the neighborhood of zero around the Compton wavelength.

For the values of  $\alpha$ , it is only reasonable to assume that the scalar field's Compton wavelength to be smaller than the orbital separation between merging neutron stars at the time when the ground-based detectors are sensitive to observe and calculate the tidal deformability. Assuming that we can detect the emitted gravitational waves with current instruments when the orbital separation decreases to a few hundreds of kilometers, we chose  $\alpha \leq 100$  which gives a Compton wavelength  $\leq 154$  km.

## Chapter 4

# Understanding Modified Gravity: Insights from Our Results

*"Without data, you're just another person with an opinion."* – W. Edwards Deming.

The cores of NS are believed to contain extremely rare phases of matter ([Dexheimer et al., 2018](#)). When it comes to high density matter, many different phases or compositions may occur, including hyperons, quarks, superconducting matter, or colored superconducting matter. Understanding their internal structure requires a deep understanding of both the behavior of matter at extreme densities and the principles of gravity. Extensive research is underway in the field of astrophysics to investigate the EoS of NS, which plays a crucial role in determining their fundamental properties such as mass, radius, and thermal evolution. Despite significant efforts, our current understanding of fundamental physics remains inadequate at high densities, leading to the absence of a unique EoS for NS ([Somasundaram et al., 2022](#); [Altiparmak et al., 2022](#); [Gorda et al., 2022](#)). Challenges in obtaining precise nuclear physics experimental data, uncertainties in the characteristics of nuclear matter, and limitations in observational data pose significant obstacles in accurately determining the EoS of NS. Nevertheless, recent advancements in multimessenger observations are providing fresh perspectives and valuable insights into the elusive EoS of these celestial objects. Several groups try to infer the EoS of NS by using astrophysical data ([Imam et al., 2022](#); [Malik et al., 2022](#); [Coughlin and Dietrich, 2019](#); [Wesolowski et al., 2016](#); [Landry et al., 2020](#); [Huang et al., 2023](#); [Patra et al., 2022](#)).

Conversely, one area of research that has gained significant attention in recent years is modified gravity theories. These theories propose modifications to Einstein's General Relativity (GR) to explain certain phenomena, such as the accelerated expansion of the universe or compatibility with quantum mechanics ([Sahni and Starobinsky, 2000](#); [Padmanabhan, 2003](#); [Copeland, 2007](#); [Sotiriou and Faraoni,](#)

2010; Birrell and Davies, 1982). One of the key predictions of modified gravity theories is the existence of scalar fields (Babichev and Langlois, 2010; Sotiriou and Faraoni, 2010; Clifton *et al.*, 2012). These scalar fields can affect the properties of a NS, such as its mass-radius relation and its moment of inertia (Cooney *et al.*, 2010; Orellana *et al.*, 2013; Capozziello *et al.*, 2016). The study of NS in the context of modified gravity theories is an active area of research, as it offers the possibility of testing the predictions of these theories against observational data (Arapoğlu *et al.*, 2011; Astashenok, 2014; Yazadjiev *et al.*, 2014; Nobleson *et al.*, 2021). In particular, some modified gravity theories predict that NS can have a different radius than predicted by GR (Yazadjiev *et al.*, 2014; Capozziello *et al.*, 2016; Aparicio Resco *et al.*, 2016; Llanes-Estrada, 2017).

On one hand, our limited knowledge of the constituents of the NS contributes to the uncertainty in mass-radius estimates. On the other hand, the free parameter of the modified gravity also contributes to the degeneracy in mass-radius estimates. Understanding the NS properties of different EoS within the framework of a modified gravity helps us constrain the degeneracies caused by EoS and the free parameter of the modified gravity. Observations of NS can be used to test the predictions of modified gravity theories. For example, measurements of the mass and radius of a NS (Miller *et al.*, 2019; Raaijmakers *et al.*, 2019; Miller *et al.*, 2021), tidal deformability in a coalescing binary NS merger (Abbott *et al.*, 2018; LIGO, 2018) can be used to constrain the properties of the scalar field and to test the theory's predictions. Additionally, measurements of the moment of inertia and tidal deformability of NS can also be used to put the theory's claims about the NS compactness to the test (Yazadjiev *et al.*, 2018; Raithel, 2019).

This chapter discusses our results from three studies of NS in the framework of modified gravity.

## 4.1 Comparison of Methods in $f(R)$

Nobleson, K., A. Ali, and S. Banik, *Comparison of Perturbative and Non-perturbative Methods in  $f(R)$  Gravity*, The European Physical Journal C, 82(1):32 (2022) <sup>1</sup>.

In the literature, we find that there are two methods used to derive the TOV equations that describe the equilibrium configurations of NS: a) perturbative (Cooney *et al.*, 2010; Arapoğlu *et al.*, 2011; Astashenok, 2014) and b) non-perturbative methods (Babichev and Langlois, 2010; Yazadjiev *et al.*, 2014). The perturbative method involves expanding the modified gravity equations in terms of small deviations from GR. This approach assumes that the modifications introduced by the additional term in  $f(R)$  function are relatively small compared to the background GR solution. On the other hand, in the

---

<sup>1</sup>This work was done in collaboration with Amna Ali, Sarmistha Banik, and with useful inputs from Tuhin Malik



non-perturbative method the equations are derived without assuming small deviations from GR. This approach provides a more comprehensive and accurate treatment of the modified theory, considering all nonlinear effects arising from the modified equations of motion. There is an ongoing debate surrounding the accurate method for deriving the TOV equations in  $f(R)$  gravity, which arises from the differences in their underlying assumptions and the limitations of each approach. While the perturbative method offers simplicity and ease of computation, it may not capture the full range of effects introduced by the modification. In contrast, the non-perturbative method provides a more rigorous treatment. In addition, the mass-radius relations are obtained using different types of EoS that are not common in these methods. As a result, a meaningful comparison of the results is not straight forward.

In this study, we compare the  $f(R)$  results from the perturbative and non-perturbative methods using the same EoS in both methods. In the perturbative method, for each EoS, the modified TOV equations are numerically solved using boundary conditions for pressure and mass at the centre and at the surface. The exterior Schwarzschild solution is imposed, which is equivalent to freezing the scalar degree of freedom outside the star. In the non-perturbative method, the interior and exterior equations are solved self-consistently and non-perturbatively. While the perturbative method allows negative values for  $\alpha$ , the non-perturbative method allows for only positive values. To avoid tachyonic instabilities, the values of  $\alpha$  should always be positive (Frusciante *et al.*, 2019). To obtain a fair comparison of the results from these two methods, we analyze the output of these methods using the same EoS. We used  $DD2$ ,  $BHBA\phi$ ,  $FSU2R(FSU)$ , and  $FSUQ$  EoS to demonstrate the variations in the mass and radius estimations from the two methods of solving the TOV equations in  $f(R)$  gravity as described in the sections 3.2.2 and 3.2.3.

#### 4.1.1 Results and Discussions

We begin with plotting the above-mentioned EoS and the corresponding structure profile in GR. In Figure 4.1, the pressure ( $p$ ) versus energy density ( $\rho$ ) is plotted for the the nucleonic EoS  $DD2$  and  $FSU$  in solid lines. The  $DD2$  EoS is named  $BHBA\phi$  as per the original nomenclature when  $\Lambda$ s are added to it. On the other hand,  $FSUQ$  EoS has quarks in addition to the nucleonic  $FSU$  EoS. The strange  $BHBA\phi$ , and  $FSUQ$  EoSs are plotted in dashed and dotted lines respectively.

In GR, a static, spherically symmetric, non-rotating, hydrodynamic equilibrium configuration is obtained by solving the TOV equations 3.2 with the appropriate boundary conditions for pressure and mass at the center and at the surface for each EoS, with the integration performed from the center to the surface of the NS. Of the two nucleonic EoSs considered,  $DD2$  EoS is visibly much stiffer than  $FSU$ .

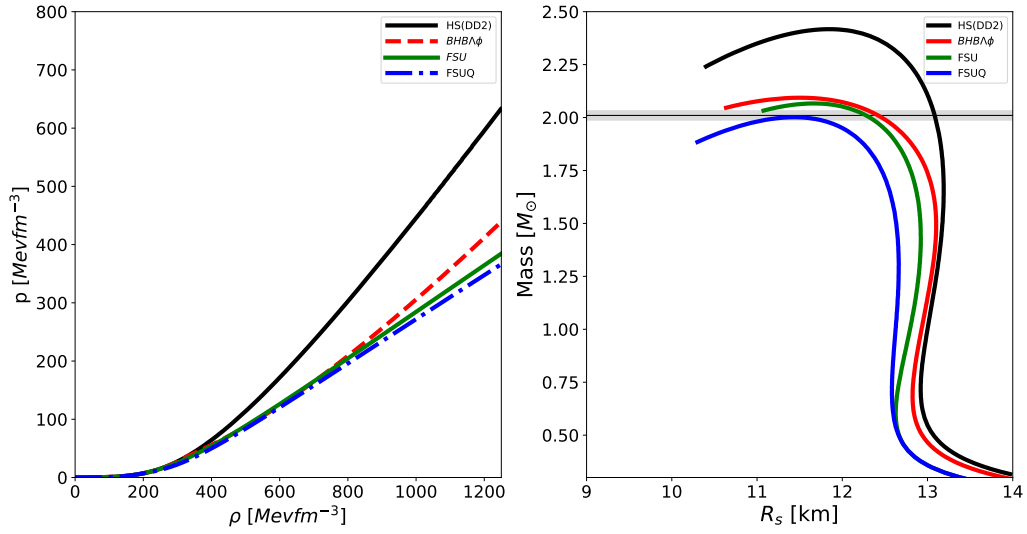


**Figure 4.1:** a) Pressure ( $p$ ) versus energy density ( $\rho$ ) is plotted for the nucleonic EoS  $DD2$  and  $FSU$  in solid lines. Strange [ $BHBL\phi$ ] and quark [ $FSUQ$ ] EoSs are plotted in dashed and dotted lines respectively. b) M-R curves for EoS in the left panel are obtained in GR.

**Table 4.1:** Maximum mass and corresponding radius of the NS for  $a=0$  (GR);  $a = 50$  for non-perturbative (NP)  $f(R)$  and  $a = 0.2$  for perturbative (P)  $f(R)$

EoS	GR		NP $f(R)$		P $f(R)$	
	$M_{max}$ $M_{\odot}$	Radius km	$M_{max}$ $M_{\odot}$	Radius km	$M_{max}$ $M_{\odot}$	Radius km
DD2	2.42	11.85	2.66	13.06	1.99	10.32
$BHBL\phi$	2.09	11.51	2.34	12.53	1.99	9.91
FSU	2.07	11.66	2.31	12.59	1.67	10.11
FSUQ	2.00	11.44	2.24	12.41	1.61	9.91

The addition of hyperons/quarks to nucleonic EoS has made them softer. Also, the quark EoS  $FSUQ$  is softer than strange EoS  $BHBL\phi$ .

The GR mass versus radius for  $DD2$ ,  $BHBL\phi$ ,  $FSU$ , and  $FSUQ$  is shown in Figure 4.1b. Table 4.1 shows the maximum masses for each of them. The section of a curve where  $\frac{dM}{d\rho_c} < 0$  is gravitationally unstable. The black horizontal line indicates the maximum mass constraint from observation of  $2M_{\odot}$  (Antoniadis *et al.*, 2013; Miller *et al.*, 2019, 2021), while the grey band represents measurement error. It is clear that these four EoS meet the maximum mass constraint. When hyperons were added to  $DD2$  EoS, the maximum mass was lowered from  $2.42M_{\odot}$  to  $2.09M_{\odot}$ . With the addition of quarks to  $FSU$  EoS, the maximum mass was lowered from  $2.06M_{\odot}$  to  $2.00M_{\odot}$ . Moreover, the radius corresponding to the maximum mass of all these EoS is between  $11.4 - 11.9$  km, which is well within the NICER (Raaijmakers *et al.*, 2019) values.

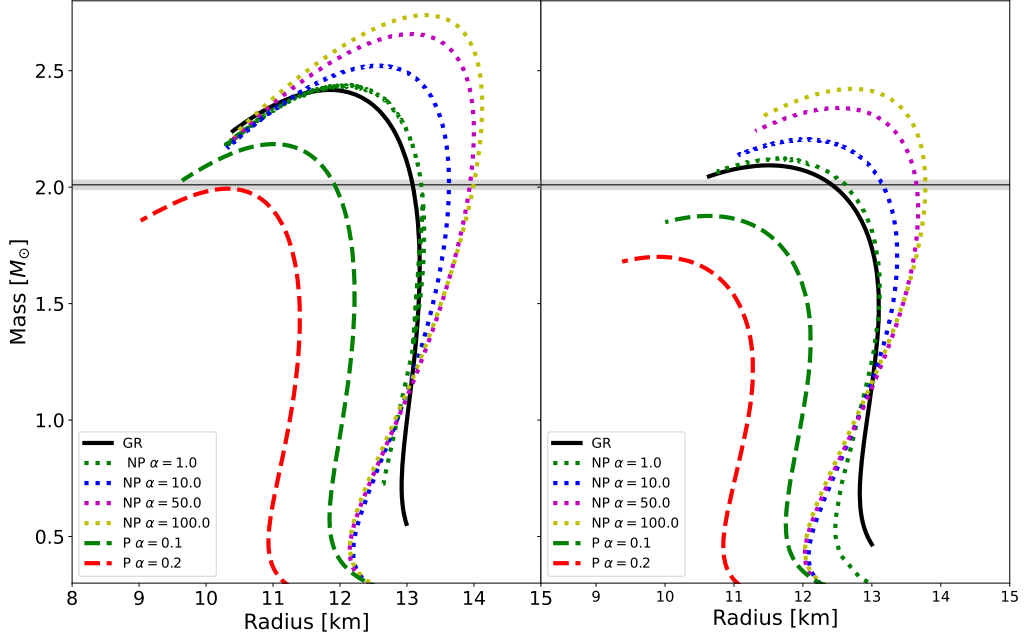


**Figure 4.2:** a) M-R curves of EoS DD2 obtained using both perturbative (dashed lines) and non-perturbative (dotted lines) methods. b) M-R curves of EoS BHBA $\phi$  obtained using both perturbative (dashed lines) and non-perturbative (dotted lines) methods.

The mass versus radius for DD2 EoS is shown in figure 4.2a for both the perturbative (dashed lines) and non-perturbative (dotted lines) methods. In the perturbative method, the maximum mass falls as the value of the free parameter ' $\alpha$ ' increases. When ' $\alpha$ ' is greater than 0.2, the maximum mass decreases below the observational limit. With the non-perturbative method, however, the maximum mass and radius increase with an increase in the parameter ' $\alpha$ '. We investigate values of ' $\alpha$ ' up to 100 in this method, which is the highest limit of sensitivity of current gravitational wave detectors. The mass versus radius for BHBA $\phi$  EoS is shown in Figure 4.2b for both the perturbative (dashed lines) and non-perturbative methods (dotted lines). The maximum mass in the perturbative method drops as the free parameter ' $\alpha$ ' increases, and it falls considerably below the observational limit even with a 0.1 increase in ' $\alpha$ '. However, the maximum mass in the non-perturbative method increases with parameter ' $\alpha$ ' and remains above the observational constraint with a slight increase in radius.

The mass versus radius plot for FSU EoS is shown in Figure 4.3a for both perturbative (dashed lines) and non-perturbative (dotted lines) methods. The maximum mass falls as the value of the free parameter ' $\alpha$ ' increases in the perturbative method. The maximum mass decreases considerably below the observational limit when  $\alpha = 0.1$ . However, for all values of ' $\alpha$ ' up to 100, the maximum mass remains above the observational constraint in the non-perturbative method. The mass versus radius for

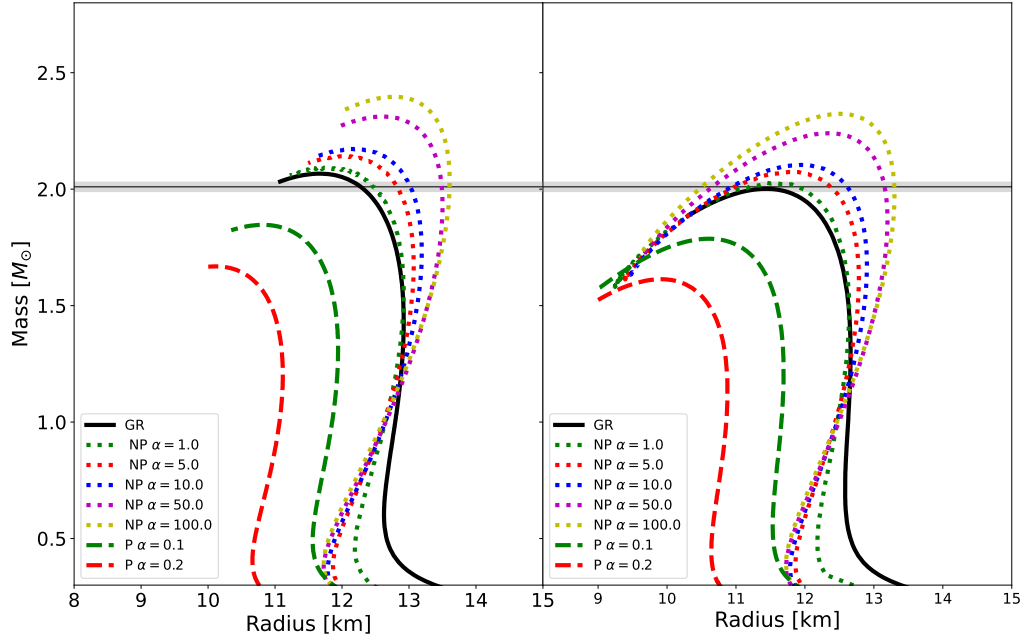


**Figure 4.3:** a) M-R curves of EoS FSU obtained using both perturbative (dashed lines) and non-perturbative (dotted lines) methods. b) M-R curves of EoS FSUQ obtained using both perturbative (dashed lines) and non-perturbative (dotted lines) methods.

*FSUQ* EoS is shown in Figure 4.3b for both perturbative (dashed lines) and non-perturbative (dotted lines) methods. Even with a 0.1 increase in ' $\alpha$ ', the maximum mass in the perturbative method is considerably below the observational limit. The maximum mass in the non-perturbative method, on the other hand, increases with the parameter ' $\alpha$ ' and remains above the observational constraint with a small rise in NS radius.

The variation in compactness with regard to change in ' $\alpha$ ' is depicted in Figure 4.4a for the non-perturbative method. The compactness of the NS is correlated with the stiffness of the EoS for any given ' $\alpha$ ', with the stiffest EoS, *DD2*, having the highest compactness and the softest EoS, *FSUQ*, having the lowest compactness. The presence of hyperons and quarks in the nucleonic EoS decreases NS compactness. When the value of ' $\alpha$ ' grows, the compactness drops at first, then gradually increases. The perturbative approach's compactness versus an is shown in Figure 4.4b. We observe that the stiffness of the EoS is correlated to the NS compactness. However, the overall compactness of the NS in perturbative method is smaller than that of the non-perturbative method, and the compactness decreases as the value of ' $\alpha$ ' increases.

In Figure 4.5a, the compactness of the NS obtained in  $f(R)$  is normalized to the compactness of the NS obtained in GR. With the non-perturbative method, we observe that for  $\alpha < 10$ , the compactness

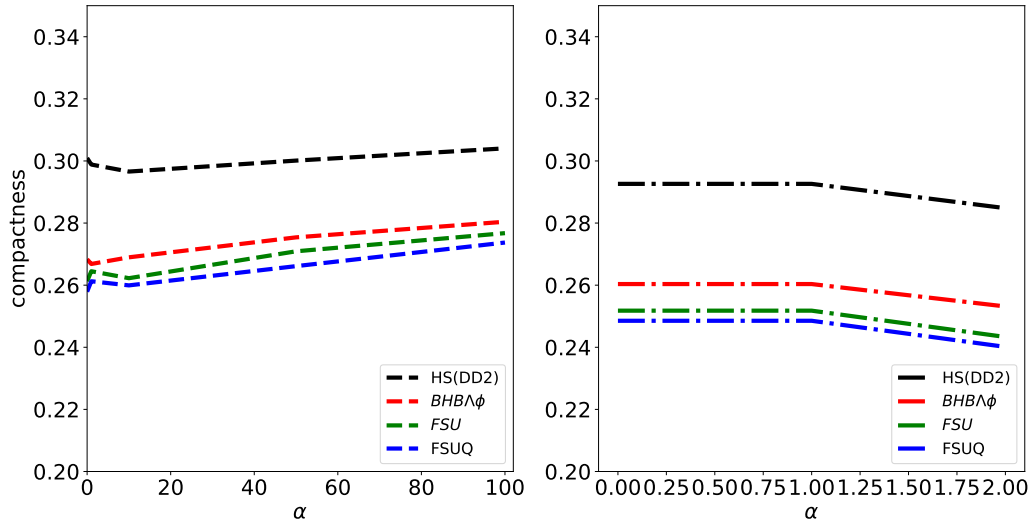


**Figure 4.4:** a) Compactness of NS for different EoS using non-perturbative method. b) Compactness of NS for different EoS using perturbative method..

decreases and then gradually increases. It is worth noting that softer EoS NS are more compact in  $f(R)$  than GR. When ' $\alpha$ ' grows, the inclusion of quarks/hyperons enhances the compactness with regard to GR. In the perturbative method, the compactness diminishes monotonically as ' $\alpha$ ' increases. The compactness of softer EoS is less than that of stiffer EoS.

The maximum allowed deviation from the GR prediction is bound by the requirement that the solutions preserve their perturbative validity for all of the cases studied here with regard to different values of ' $\alpha$ ' in the  $f(R)$  model for the various EoS. To be in the perturbative regime, the first order corrections to the metric must be small. This is measured using

$$|\Delta| = \left| \frac{A_{f(R)}(r)}{A_{GR}(r)} - 1 \right| \quad (4.1)$$

where  $A_{f(R)}(r)$  and  $A_{GR}(r)$  are the  $rr$  components of the metric defined for  $f(R)$  and GR, respectively. This quantity is a function of radius of each star and depends on the EoS. It reaches its highest near the star's core, where density and curvature are high. We evaluate at its maximum since we require the complete solution to be perturbatively close to the GR. The maximum ratio  $|\Delta_{max}| < 1$  is a necessary condition for perturbative validity. Figure 4.6 shows the EoS in the  $f(R)$  gravity model as a function of parameter ' $\alpha$ '. This figure shows that NS in the  $f(R)$  gravity model may be treated perturbatively as long as the magnitude of  $\alpha$  is in the range  $0 < \alpha < 0.2$ .

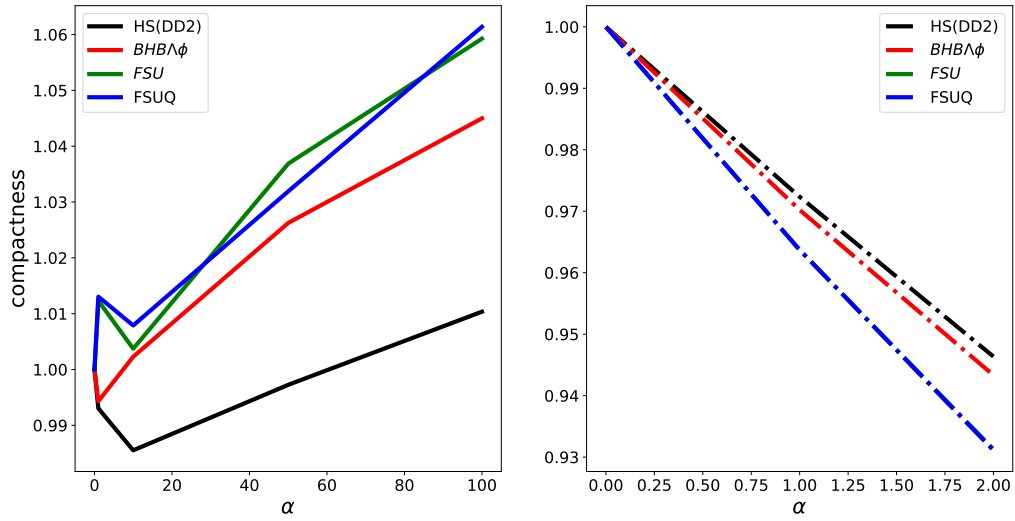


**Figure 4.5:** a) Compactness normalized with respect to the GR compactness for non-perturbative method. b) Compactness normalized with respect to the GR compactness for perturbative method.

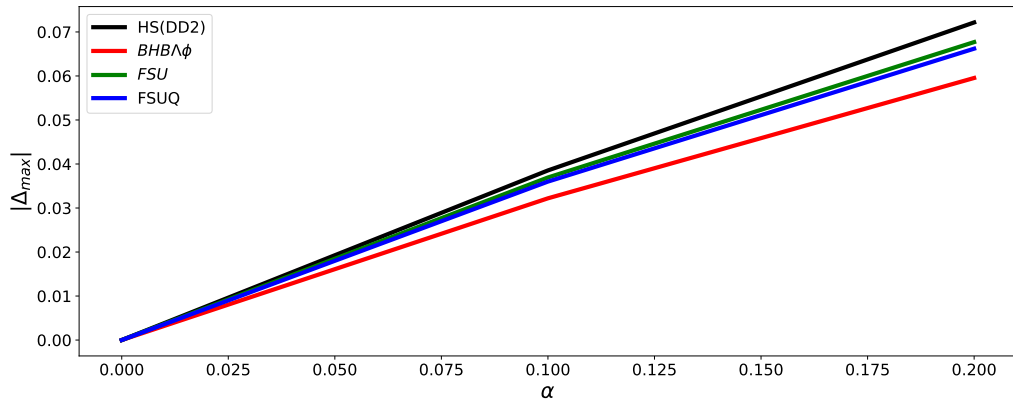


**Figure 4.6:**  $|\Delta_{max}|$  as a function of  $a$  for all EoSs in  $f(R)$ .

## 4.1.2 Conclusions

In this study, we analyze the NS solutions with realistic EoS in GR and in  $f(R)$  gravity model. For this, we choose EoSs that are generated in the framework of relativistic mean field models. The NS core under these EOSs, contains the strange particles in the form of  $\Lambda$  hyperons and quarks as well as nucleons and leptons. With these EOSs, the mass-radius profiles for static NS calculated in GR by solving the TOV equations lie well within the observational limits.

Obtaining the TOV equations from the fourth order field equation is difficult. Commonly two methods are used to solve these equation in case of  $f(R)$  gravity, the perturbative method, where  $f(R)$  theories are considered as a perturbation to GR and the non-perturbative method. We use both these methods in

$f(R)$  gravity and try to figure out which method is more suited to investigate the strong field regime. Our numerical integration using nuclear EoS (*DD2*, *FSU*) and strange EoS (*BHBA $\phi$* , *FSUQ*), constraints the extra degree of freedom parameter  $\alpha$  that arise in  $f(R) = R + \alpha R^2$  gravity. It is to be noted that for  $\alpha = 0$  the maximum mass tends to the corresponding value in GR for the EoS.

For the case of non-perturbative method, a wide range of parameter  $\alpha$  is considered. We notice that, for all  $\alpha$  more massive the star, more is its compactness. The maximum mass of NS is always greater than in case of GR and is larger for large values of  $\alpha$ . The radius of the NS too increases marginally with increase in  $\alpha$ . This trend is same for both nuclear and strange EoS, however, the strange EoS NS are more compact in  $f(R)$  compared to GR. Although, for nonzero values of  $\alpha$  the deviation from GR can be large, they are still admissible, as they satisfy the observational bound of  $2M_{\odot}$  limit. This is why the present observations of the NS masses and radii can not alone put constraints on the value of the parameter  $\alpha$ . We can therefore conclude that  $f(R)$  theory of gravity can bring about remarkable change in the properties of NS. Also,  $f(R)$  can admit the EoS which otherwise do not satisfy the observational limit of  $2M_{\odot}$  in GR.

The perturbative approach in  $f(R) = R + \alpha R^2$  can be used only when the range of  $\alpha$  is  $0 < \alpha < 0.2$ . In this limit, except for EoS DD2 none other EoSs considered satisfy the observational limit of maximum mass ( $2M_{\odot}$ ). This approach therefore does not seem to work in the strong field limit and does not satisfy the astrophysical observations of NS. The main reason for this is that we do not consider the nonlinear terms which might appear in the strong field regime that can impact the structure and the properties of the NS. Many viable modified gravity models have been studied in literature using the perturbative approach (Cooney *et al.*, 2010; Arapoğlu *et al.*, 2011; Astashenok, 2014), where negative values of the free parameter is considered to fit the observations. However studies by Babichev and Langlois (2010); Yazadjiev *et al.* (2014) show that a viable gravity model with negative free parameter is not feasible due to presence of ghost and tachyonic instabilities.

## 4.2 Universal Relation in $f(R)$

Nobleson, K., S. Banik, and T. Malik., *Unveiling a universal relationship between the  $f(R)$  parameter and neutron star properties*. Physical Review D, 107(12):124045(2023)

Several studies in the literature have investigated the effects of using different EoS in  $f(R)$  gravity, but a comprehensive statistical analysis is yet to be done. In general, the properties of a NS, such as its mass and radius, are sensitive to the EoS model. However, interestingly various relationships between the physical properties of NS have been discovered that are insensitive to the EoS model. These are

called universal relationships and they are typically insensitive to EoS models to the  $\mathcal{O}(1\%)$  level. The compactness parameter  $M/R$ , stellar oscillation frequencies, and, I-Love-Q relations that relate mass, moment of inertia, tidal deformability, and the spin-induced quadrupole moment, are some examples. In this study, we use the Bayesian inference method to generate a complete snapshot of the  $f(R)$  model for various EoS. Our primary goal is to understand the relationships between the properties of NS and the free parameter of the  $f(R)$  model while taking the currently known uncertainties of EoS into account. This study provides a comprehensive analysis of the relationship between  $f(R)$  parameter and NS properties. We also found a universal relationship between the  $f(R)$  gravity model parameter and the maximum mass of the NS.

### 4.2.1 Bayesian estimation

Bayesian analysis (Gelman *et al.*, 2013) is a very strong statistical approach that uses probability theory to make predictions and draw conclusions about the NS properties using mass, radius, and tidal deformability data. This way, we can quantify the uncertainty associated with their measurements and predictions, and improve our theoretical understanding. Bayesian analysis is routinely used in other major astrophysics problems, i.e., to analyze gravitational-wave signals (Ashton *et al.*, 2019), properties of short gamma-ray bursts (Biscoveanu *et al.*, 2020), test GR (Keitel, 2019; Ashton and Khan, 2020; Payne *et al.*, 2019) and to study a wide range of properties of NS (Coughlin and Dietrich, 2019; Hernandez Vivanco *et al.*, 2019; Biscoveanu *et al.*, 2019), including their masses, radii, and EoS (Malik and Providência, 2022; Traversi *et al.*, 2020).

The Bayesian approach can do a comprehensive statistical analysis of a model's parameters for a given set of data. It provides the joint posterior distributions of model parameters, allowing one to investigate the distributions of given parameters and the correlations between them. The joint posterior distribution of the parameters  $P(\Theta|D)$  based on the Bayes theorem (Gelman *et al.*, 2013) can be written as

$$P(\Theta|D) = \frac{\mathcal{L}(D|\Theta)P(\Theta)}{\mathcal{Z}} \quad (4.2)$$

where  $D$  and  $\Theta$  are the data and set of model parameters respectively. Here  $P(\Theta)$  is the prior for model parameters,  $\mathcal{L}(D|\Theta)$  is the likelihood function and  $\mathcal{Z}$  is the evidence. The posterior distribution was evaluated by Pymultinest (Buchner *et al.*, 2014) implementation.

### The prior

Our chosen model of  $f(R)$  has only one parameter,  $\alpha$ . We have taken a uniform distribution [3.5, 2000] to determine the prior on  $\alpha$ . The models with  $\alpha < 3.5$  and  $\alpha > 2000$  are very close to the cases of



**Table 4.2:** The constraints imposed in the Bayesian inference: Observed maximum mass of NS, Radius of  $2.08 M_{\odot}$  NS, Radius of  $1.4 M_{\odot}$  NS.

Constraints		
Quantity	Value/Band	Reference
$M_{max}$	$> 2.0 M_{\odot}$	(Miller <i>et al.</i> , 2021)
$R_{2.08}$	$12.4 \pm 1.0$ km	(Miller <i>et al.</i> , 2021)
$R_{1.4}$	$13.02 \pm 1.24$ km	(Miller <i>et al.</i> , 2019)

<sup>1</sup>Note: Please note that the NS maximum mass does not affect the likelihood in our case, and it has been included for completeness only. This is because the  $f(R)$  parameter, denoted as  $\alpha$ , can only increase the mass of NS. Furthermore, the EoS that we have chosen already predict NS with maximum masses above  $2 M_{\odot}$  in GR ( $\alpha = 0$ ).

$\alpha = 0$  and  $\alpha = 2000$ , respectively. Similar behaviour for  $\alpha$  is also reported by Yazadjiev *et al.* (2014). The dimensions of the parameter  $\alpha$  is in terms of  $r_g^2$ , where  $r_g = 1.47664$  km corresponds to one  $1M_{\odot}$ .

### The fit data

The constraints used to fit for the parameter of  $f(R)$  model is based on the NS observational properties, such as maximum mass ( $M_{max}$ ), radius at maximum mass ( $R_{2.08}$ ), and at  $1.4M_{\odot}$  ( $R_{1.4}$ ) listed in Table 4.2

### The Log-Likelihood

The log-likelihood for mass, radius at maximum mass, and radius at  $M_{1.4}$  are defined as follows:

$$\log M_{max} = \log \left[ \frac{1}{\exp \left[ \frac{M_{cal} - M_{obs}}{\Delta M} \right] + 1} \right] \quad (4.3)$$

$$\log R_{2.08} = -0.5 \left[ \frac{R_{2.08calc} - R_{2.08obs}}{\Delta R_{2.08}} \right]^2 + \log [2\pi \Delta R_{2.08}^2] \quad (4.4)$$

$$\log R_{1.4} = -0.5 \left[ \frac{R_{1.4calc} - R_{1.4obs}}{\Delta R_{1.4}} \right]^2 + \log [2\pi \Delta R_{1.4}^2] \quad (4.5)$$

Here  $\Delta R$  and  $\Delta M$  represent the uncertainty in the measurement of mass and radius from the observations.

In figure 4.7, we plot the pressure versus the baryonic number density for the three RMF EoS used in this study: DD2 (black, solid line), FSU2R (blue, dotted line), and SFHx (pink, dashed line). The grey band (hatched grey) is the prediction from the GW170817 event (Abbott *et al.*, 2019). These EoS satisfy the maximum mass and radius constraints from the observation (Riley *et al.*, 2019; Miller *et al.*,

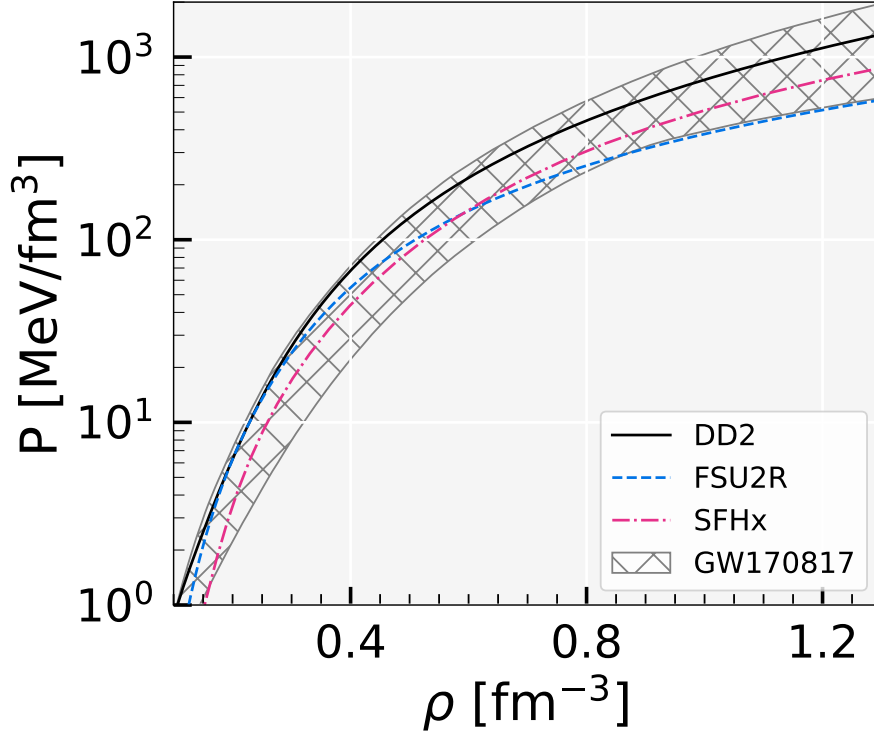


**Figure 4.7:** Pressure versus the baryonic number density for the three different RMF EoS employed for this work: DD2 (black), FSU2R (blue), and SFHx (pink). There is also a band (hatched gray) that has been predicted based on the GW170817 event.

2019; Riley *et al.*, 2021; Miller *et al.*, 2021). The GR maximum mass for DD2, SFHx, and FSU2R are  $2.40M_{\odot}$ ,  $2.13M_{\odot}$ , and  $2.06M_{\odot}$ , respectively.

#### 4.2.2 Results and Discussions

The posterior probability distributions of the  $f(R)$  model parameter  $\alpha$  are analyzed as follows. Our Bayesian approach to estimating the parameter  $\alpha$  utilizes a uniform ("un-informative") prior, as described in the section 4.2.1. To incorporate the well-known uncertainty of nuclear matter EoS, we have employed three distinct nuclear matter EoS models: DD2, FSU2R, and SFHx described in the section 2. Together, these models span the majority of the presently known range of uncertainty for dense matter NS EoS. They allow us to analyse the effect of modified gravity and its dependence, if any, on these EoS.

In Figure 4.8, we present a visual representation of the posterior probability distributions for the  $f(R)$  model parameter  $\alpha$  obtained using three different nuclear matter EoS models. Each distribution is represented by a curve, and the vertical lines indicate the 90% confidence interval for each case. It is interesting to observe the way the distribution's shape varies depending on the stiffness of the EoS. Specifically, the distribution is smaller (i.e., more constrained) for stiffer EoS and larger (i.e., less constrained) for softer EoS. This is due to the fact that  $f(R)$  parameter  $\alpha$  only increases the mass and radius of a NS. For a stiff EoS, the cost we employed for radius measurement from NICER imposes greater

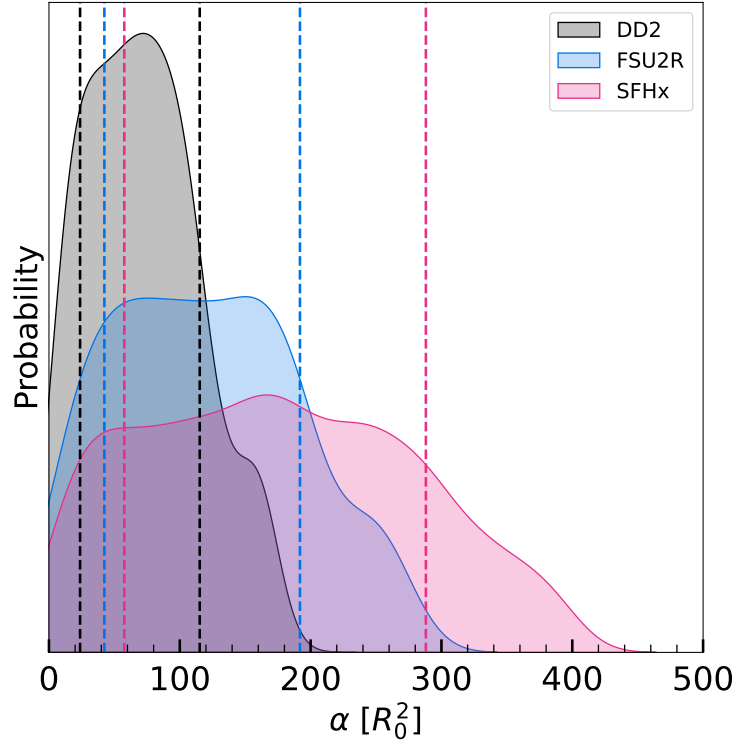


**Figure 4.8:** For three different EoS model, namely DD2, FSU2R, and SFHx, the final posteriors of the parameter  $\alpha$  for  $f(R)$  gravity are plotted. The vertical lines show the  $1\sigma$  (68%) credible intervals (CI).

constraints on the value of  $\alpha$ , i.e., if the calculated value is very large or very small in comparison to the observed value, then such  $\alpha$  value is less preferred. It is important to emphasize that the distributions of  $\alpha$  are heavy-tailed, i.e., goes to zero slower than one with exponential tail. Therefore, the probability values presented in the plot are normalized to the tail of the distribution. Additionally, it is worth noting that the effect of  $\alpha$  on the properties of a NS can only be observed within a certain range of values. Beyond this range, increasing the value of  $\alpha$  has no impact on the star's properties (see section 2.2.1).

The full posterior of  $\alpha$  was used to generate the entire mass-radius domain for three different models, namely DD2, FSU2R, and SFHx in figure 4.9. The grey zones in the figure's lower left corner, which represent the 90% (solid) and 50% (dashed) confidence intervals for the binary components of the GW170817 event (Abbott *et al.*, 2019), serve as a baseline for comparison. Also, the  $1\sigma$  (68%) credible zone of the 2-D posterior distribution in the mass-radius domain obtained from millisecond pulsars PSR J0030+0451 (light green and light blue) (Riley *et al.*, 2019; Miller *et al.*, 2019) and PSR J0740+6620 (light orange) (Riley *et al.*, 2021; Miller *et al.*, 2021) for the NICER X-ray data is plotted. The error bars, both horizontal (radius) and vertical (mass), represent the 1-D marginalised posterior distribution's  $1\sigma$  credible interval. The figure also shows that measurement of NS radius at higher masses can greatly

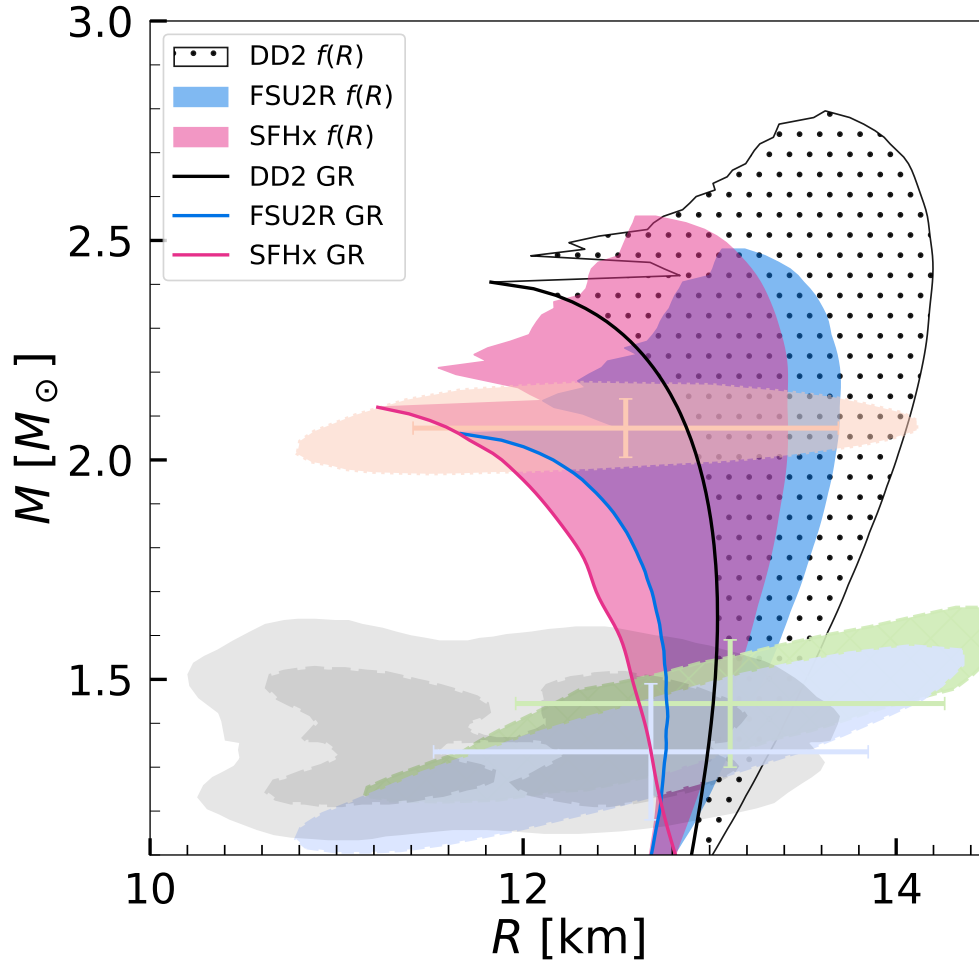


**Figure 4.9:** The entire M-R domain is plotted for three different EoS models, namely DD2, FSU2R, SFHx obtained for the full posteriors of the parameter  $\alpha$  for  $f(R)$  gravity. The gray zones indicate the 90% (solid) and 50% (dashed) credible Interval for the binary components of the GW170817 event. The  $1\sigma$  (68%) credible zone of the 2-D posterior distribution in mass-radii domain from millisecond pulsar PSR J0030+0451 (light green and light blue) as well as PSR J0740+6620 (light orange) are shown for the NICER x-ray data. The horizontal (radius) and vertical (mass) error bars reflect the  $1\sigma$  credible interval derived for the same NICER data's 1-D marginalized posterior distribution.

constrain the  $f(R)$  parameter when compared to lower mass NS. It is worth noting that the  $f(R)$  parameter,  $\alpha$ , can only broaden the M-R curve in higher mass. Observations of NS with high masses can thus provide valuable insights into the fundamental nature of these objects.

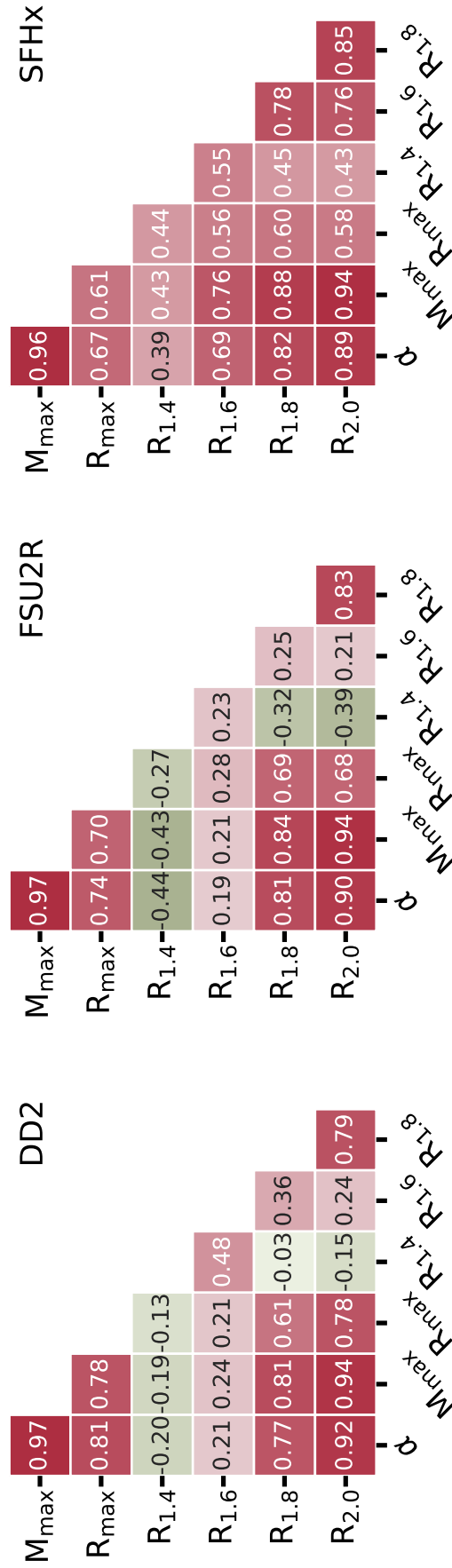


**Figure 4.10:** We plot the Kendall rank correlation coefficients between parameter  $\alpha$  for  $f(R)$  and NS properties of different mass ranges, such as NS maximum mass  $M_{\max}$ , maximum radius  $R_{\max}$ , and radius for 1.4, 1.6 and 1.8  $M_{\odot}$  NS obtained for the final posterior of three different EOSs: (left) DD2, (middle) FSU2R, and (right) SFHx.

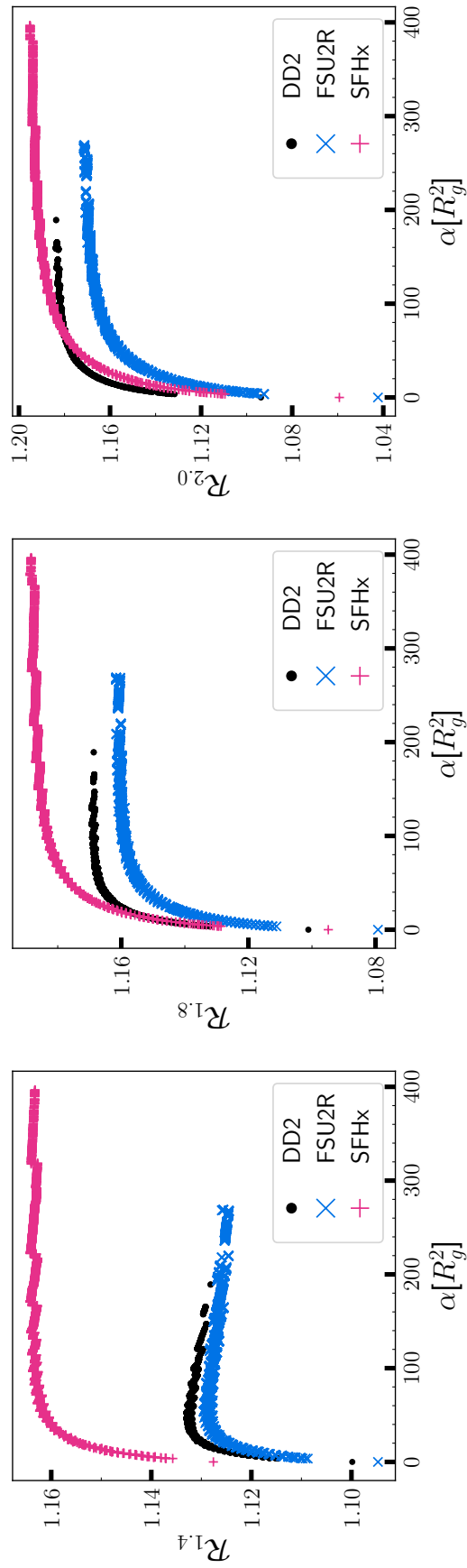


**Figure 4.11:** The dependence of normalized radius on the  $f(R)$  parameter  $\alpha$ , as obtained from the final posterior, is shown for three different models - DD2 (black), FSU2R (blue), and SFHx (pink) - and three different NS masses, ranging from  $1.4$  to  $2.0 M_\odot$  (left to right).

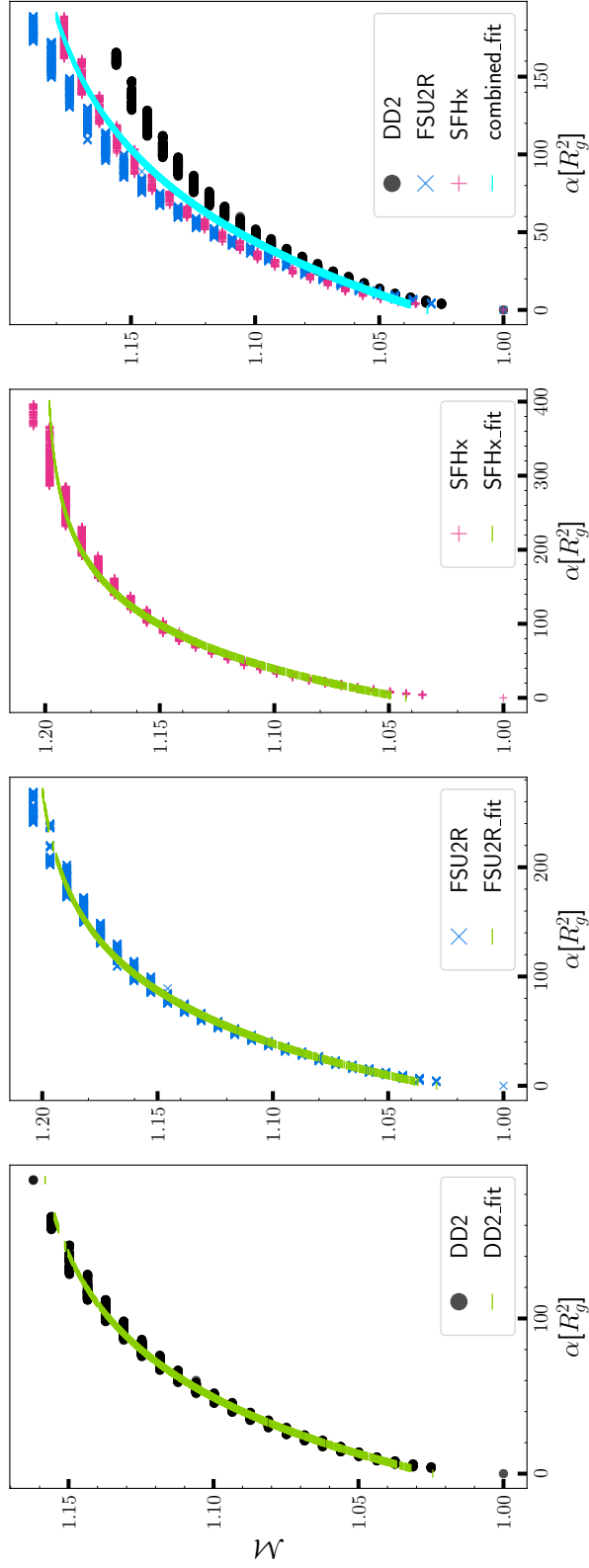


**Figure 4.12:** The dependence of normalized NS maximum mass as a function of  $f(R)$  parameter  $\alpha$ , as obtained from the final posterior, is presented for three different models - DD2 (black), FSU2R (blue), and SFHx (pink). The green curve represents the fit curve for individual EoS. The cyan curve represents the combined fit. (see text for details).

In figure 4.10, a Kendall rank correlation coefficient (Kendall, 1938) is presented, which represents the correlation between the parameter  $\alpha$  for  $f(R)$  and NS properties for different mass ranges. This correlation coefficient is derived from the final posteriors of three different EoS: DD2, FSU2R, and SFHx, for the NS maximum mass ( $M_{max}$ ), maximum radius ( $R_{max}$ ), and radius for 1.4, 1.6, and 1.8  $M_{\odot}$  NS. It is noteworthy that Pearson's correlation coefficient is typically employed in such figures to measure the linear relationship between two variables. However, Kendall's correlation coefficient is used here as it measures a monotonic relationship between two variables. Regardless of the EoS model chosen, the results show that the parameter  $\alpha$  in  $f(R)$  is strongly correlated with the NS maximum mass. Furthermore, there seems to be a strong correlation between the parameter  $\alpha$  and the radius of the NS as the star's mass increases. As the mass of the NS goes from 1.4  $M_{\odot}$  to 2.0  $M_{\odot}$ , the Kendall rank goes from  $-0.20$  to  $0.92$  for DD2,  $-0.44$  to  $0.90$  for FSU2R, and  $0.39$  to  $0.89$  for SFHx. The use of different EoS provides a comprehensive understanding of the correlation between the  $f(R)$  parameter and NS properties.

In figure 4.11, we define normalized radius  $\mathcal{R}_n$  as  $R_{nf(R)}/R_{nGR}$  where 'n' is the mass of the NS, and plot  $\alpha$  versus  $\mathcal{R}_n$  for the three EoS models – DD2 (black), FSU2R (blue), and SFHx (pink) – for NS with mass of 1.4  $M_{\odot}$ , 1.8  $M_{\odot}$ , and 2.0  $M_{\odot}$ . In the left panel of figure 4.11, for NS with mass of 1.4  $M_{\odot}$ , the normalized radius  $\mathcal{R}$  increases as  $\alpha$  increases up to about  $\alpha = 40$ . While for SFHx the value of  $\mathcal{R}$  asymptotically reaches the value of 1.17, for DD2 and FSU2R the value decreases. The value of  $\mathcal{R}$  is comparable for DD2 and FSU2R, whereas, for SFHx the value is significantly higher than the other EoS. In the middle panel, for NS with mass of 1.8  $M_{\odot}$ , the normalized radius  $\mathcal{R}$  increases as  $\alpha$  increases up to about  $\alpha = 50$ . The value of  $\mathcal{R}$  asymptotically reaches 1.16, 1.65, and 1.18 for FSU2R, DD2, and SFHx, respectively. The relative offset between the curves is reduced compared to the plot on the left. In the right panel, for NS with mass of 2.0  $M_{\odot}$ , the normalized radius  $\mathcal{R}$  increases as  $\alpha$  increases up to about  $\alpha = 50$ . The value of  $\mathcal{R}$  asymptotically reaches 1.17, 1.18, and 1.19 for FSU2R, DD2, and SFHx, respectively. The relative offset between the curves is minimum compared to the left and middle plots. At lower mass (left plot), there is an indication of EoS dependence of  $\mathcal{R}$  versus  $\alpha$ . As the mass increases from 1.4  $M_{\odot}$  to 2.0  $M_{\odot}$ , the EoS dependence is reduced significantly.

In figure 4.12, the mass and radius for each EoS are estimated with the posteriors estimated of the parameter  $\alpha$ . The normalized mass  $\mathcal{M} = M_{f(R)}/M_{GR}$  is defined and plotted versus the parameter  $\alpha$ . It can be seen that any given  $\mathcal{M}$  can be generated by a value of  $\alpha$  and a few additional values in a small neighbourhood around it. As  $\mathcal{M}$  increases, the neighbourhood around  $\alpha$  also increases. The following



function is then used to fit the results:

$$\mathcal{M}(\alpha) = a + be^{c\alpha} \quad (4.6)$$

The fitting parameters for EoS DD2, FSU2R, and SFHx and the combined data are presented in Table 4.3.  $Q_{90}$  denotes the maximum percentage of relative uncertainty within a 90% confidence interval. In the first subplot, The normalized mass  $\mathcal{M}$  for DD2 is plotted against the parameter  $\alpha$ .  $\mathcal{M}$  asymptotically reaches to 1.16 as  $\alpha$  increases. In the second subplot,  $\mathcal{M}$  versus  $\alpha$  is plotted for FSU2R.  $\mathcal{M}$  asymptotically reaches to 1.19 as  $\alpha$  increases. In the third one,  $\mathcal{M}$  versus  $\alpha$  is plotted for SFHx.  $\mathcal{M}$  asymptotically reaches to 1.18 as  $\alpha$  increases. In the right most subplot,  $\mathcal{M}$  versus  $\alpha$  for all the three EoS are plotted. A curve is fitted to the combined data which is represented by the cyan curve.  $\mathcal{M}$  asymptotically reaches to 1.18 as  $\alpha$  increases. It is interesting to note that the stiffer EoS has relatively smaller values for 'a' and higher values for 'b'. Using this universal relationship, we can estimate the mass of the NS for any given value of  $\alpha$  within  $Q_{90}$ .

**Table 4.3:** The fit for M-R curves are listed for the EoS DD2, FSU2R, and SFHx as well as a common fit for the combined data. The maximum percentage of relative uncertainty within 90% confidence interval is indicated in  $Q_{90}$

<b>Fit values</b>				
EoS	a	b	c	$Q_{90}$
DD2	1.165	-0.141	-0.0156	< 1%
FSU2R	1.205	-0.176	-0.0134	< 1%
SFHx	1.200	-0.157	-0.0116	< 1%
Combined	1.196	-0.165	-0.0124	< 2%

In earlier works ([Jiang et al., 2022](#); [Malik et al., 2023](#)), the authors showed that in GR there is a strong model independent correlation between the maximum mass star's central density  $\rho_c$  and its radius  $R_{max}$  for various EoS. We want to investigate if there are any such relationships in the  $f(R)$  domain. In figure 4.13, we plot normalized radius  $R_n$  obtained for various  $\alpha$  versus normalized central density  $\rho_n$  at which the maximum mass occurs in  $f(R)$  according to the following expressions.

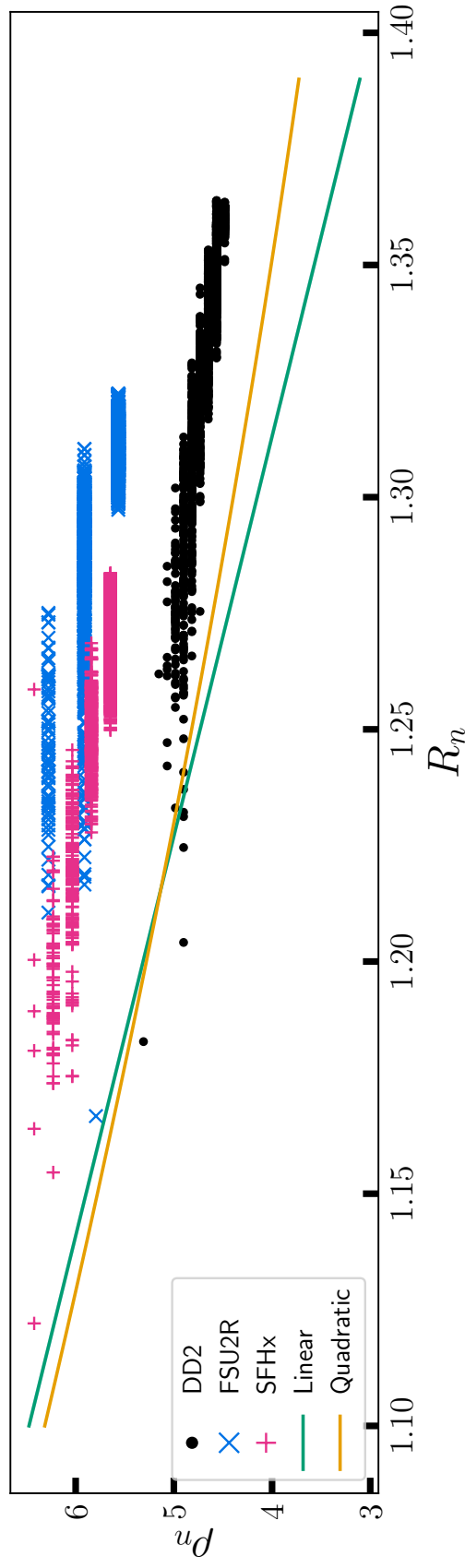


**Figure 4.13:** The correlation between normalized central density and the normalized radius of the maximum mass in  $f(R)$  for the values of the free parameter  $\alpha$  from the posterior for three different models - DD2 (black), FSU2R (blue), and SFHx (pink) are plotted. The green curve represents a linear fit and orange curve represents a quadratic curve (see text for details).

$$\rho_n = \frac{\rho_c}{0.16 \text{ fm}^{-3}}, \quad R_n = \frac{R_{\text{max}}}{10 \text{ km}} \quad (4.7)$$

The authors of [Malik \*et al.\* \(2023\)](#) proposed a linear relation with  $m_0 = -11.618 \pm 0.018$  and  $c_0 = 19.255 \pm 0.019$ . In the figure it is represented by a green curve.

$$\frac{\rho_c}{0.16 \text{ fm}^{-3}} = m_0 \left[ \frac{R_{\text{max}}}{10 \text{ km}} \right] + c_0 \quad (4.8)$$

The authors of [Jiang \*et al.\* \(2022\)](#) proposed a quadratic relation with  $d_0 = 27.6$  and  $d_1 = 7.55$  with a 3.7% standard deviation. This is represented by a orange curve in figure 4.13.

$$\frac{\rho_c}{0.16 \text{ fm}^{-3}} = d_0 \left[ 1 - \frac{R_{\text{max}}}{10 \text{ km}} \right] + d_1 \left[ \frac{R_{\text{max}}}{10 \text{ km}} \right]^2 \quad (4.9)$$

In figure 4.13, unlike GR, the data do not support the existence of a relationship between the variables under consideration in  $f(R)$ .

### 4.2.3 Conclusions

We use the non-perturbative TOV equations for  $f(R)$  gravity in this study and a Bayesian approach to estimate the posterior distributions of model parameters. We explore the impact of  $f(R)$  gravity on the parameters of the NS of three EoS using nucleonic degrees of freedom with varied stiffness and compared it to the results of GR.

We find that the measurement of NS radius at higher masses can significantly constrain the  $f(R)$  parameter as compared to lower mass NS. We also find a strong correlation between the free parameter  $\alpha$  and NS mass, regardless of the EoS used. Furthermore, we see that the  $\mathcal{R}$  of a low-mass NS is highly sensitive to EoS, whereas the high-mass counterparts are not. We establish a universal relationship between  $\alpha$  and normalised mass  $\mathcal{M}$  that allows us to calculate the maximum mass of an NS for any arbitrary  $\alpha$ . In contrast to GR, the data do not support the existence of a relationship between the maximum mass star's central density and its radius in  $f(R)$ .

Overall, this study discusses the significance of understanding the properties of NS in modified gravity theories and provides valuable insights into the nature of these compact objects. In future, this study may be extended to include a variety of EoS classes and verify the validity of this universal relationship. More observations and theoretical models are required in order to completely understand the EoS of NS and to explore the possibilities of modified gravity theories for these objects.

### 4.3 Tidal Deformability in $f(R)$

**Nobleson, K.**, T. Malik, and S. Banik. *Tidal Deformability of Neutron Stars with Exotic Particles Within a Density Dependent Relativistic Mean Field Model in R-squared Gravity*. *Journal of Cosmology and Astroparticle Physics*, 2021(08):012 (2021).

While the first neutron star was discovered in 1967, reliable mass measurements of these stars have only been possible since the last 20 years or so. The only reliable observables until now are its mass and radius measurements. However, since the GW170817 detection of the merger of two orbiting NS ([Ade et al., 2016b](#); [Abbott et al., 2018](#)), additional parameter like tidal deformability ( $\Lambda$ ) ([Hinderer, 2008](#)) is now available to study the interior of the NS.

A compact star's high-density nucleus is theorized to have more degrees of freedom than neutrons, protons, and electrons. In the presence of exotic particles, the EoS softens, resulting in a lower mass NS. As a result, observational mass can constrain EoS. The masses of two massive pulsars,  $1.928 \pm 0.017 M_{\odot}$  ([Fonseca et al., 2016](#)) and  $2.01 \pm 0.04 M_{\odot}$  ([Antoniadis et al., 2013](#)), ruled out the soft EoS, which are unable to sustain such a massive star. A few exotic EoS containing hyperons, antikaons, and quarks, on the other hand, are consistent with the above findings. The first detection of gravitational waves from a binary NS merger, GW170817, has set an upper limit on tidal deformability ([Ade et al., 2016b](#); [Abbott et al., 2018](#)), which several authors utilised to constrain the NS radius. A comprehensive list can be found in Table 1 of the review in [Baiotti \(2019\)](#). [Raithel \(2019\)](#) sets a constraint of  $9.8 < R_{1.4} < 13.2$  km, which is consistent with the radius measurement obtained from X-ray observations. An analysis of pulsar J0030+0451 by [Riley et al. \(2021\)](#) using NASA's Neutron star Interior Composition Explorer (NICER) gives us the mass and radius of the pulsar. These studies ([Raaijmakers et al., 2019](#); [Miller et al., 2019](#)) suggest that the pulsar has a mass of  $1.3 - 1.4 M_{\odot}$  and a radius of  $\sim 12.7 - 13$  km.

The tidal Love number ( $k_2$ ) represents the deformability of a body to external tidal force. The phase evolution of gravitational waves induced by the NS deformation may be decoded using the dimensionless tidal deformability parameter. It is an indicator of how the neutron star reacts to gravitational attraction on its surface and correlates with the pressure gradient inside the NS. It also strongly depends on the internal structure of the NS. With the finding of gravitational waves from the GW170817 event, several authors focused more carefully on the rich relationship between tidal deformability and the dense matter EoS ([Bandyopadhyay et al., 2018](#); [De et al., 2018](#); [Radice et al., 2018](#); [Datta and Char, 2020](#)). Precise measurements of the  $\Lambda$  and radius of NS can be utilised as an effective probe to investigate dense matter EoS ([Malik et al., 2018](#)).

There is currently a significant overlap in the uncertainties caused by our incomplete understanding

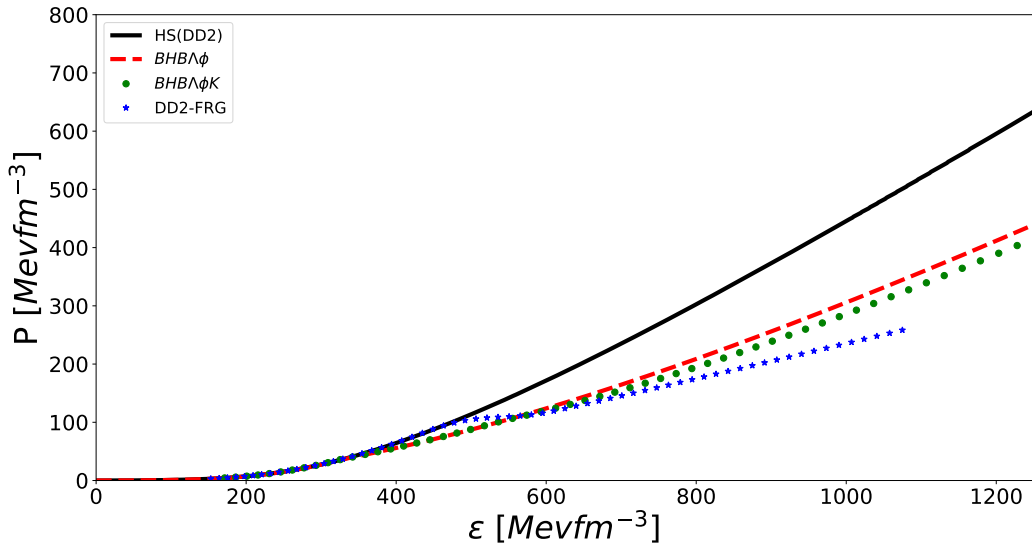


**Figure 4.14:** Neutron star EoSs (energy density ( $\epsilon$ ) versus pressure (P)) for different models – both nucleon only and with additional exotic particles such as  $\Lambda$ ,  $K^-$  condensates and quarks.

of the EoS and the free parameter of modified gravity theories. The EoS of NS is better understood if the free parameter in the modified gravity theory is strongly constrained, and vice versa. In a previous study by [Yazadjiev \*et al.\* \(2014\)](#), they employed EoS such as SLY4 and APR4 to determine the mass, radius, and tidal love number ( $k_2$ ), in non-perturbative  $f(R)$ . In this work, we analyse this further using EoS with various constituents, including quarks and strange particles, and compute the mass and radius for various values of  $\alpha$  while setting an upper bound on  $\alpha$  based on observational constraints.

### 4.3.1 Results and Discussions

Compared to the Fermi energy of the constituent fermions, the internal temperature of the NS is low. As a result, the dense matter relevant to the NS core may be represented using zero temperature EoS. We take into account EoS corresponding to dense matter with either A) only nucleons (*DD2*) or B) nucleons with extra strange components (*BHBA $\phi$* , *BHBA $\phi$ K $^-$* , *DD2 – FRG*). All the models considered in this work obey the mass-radius constraints of astrophysical observations ([Fonseca \*et al.\*, 2016](#); [Antoniadis \*et al.\*, 2013](#); [Demorest \*et al.\*, 2010](#)). The above-mentioned EoSs are plotted in figure 4.14. The nucleonic HS(*DD2*) EoS is denoted by solid black line. The other curves represent EoS containing additional exotic particles such as  $\Lambda$  hyperons (*BHBA $\phi$* ),  $\Lambda$  hyperons and anti(kaon) condensates (*BHBA $\phi$ K $^-$* ) and quarks (*DD2 – FRG*) in the *DD2* model. The addition of strange particles softens the EoS. The *DD2-FRG* is evidently the softest of the lot.

In GR, we derive and solve the TOV equations for a spherically symmetric, non-rotating neutron star with appropriate boundary conditions to obtain the mass and radius of a given EoS. For a chosen central

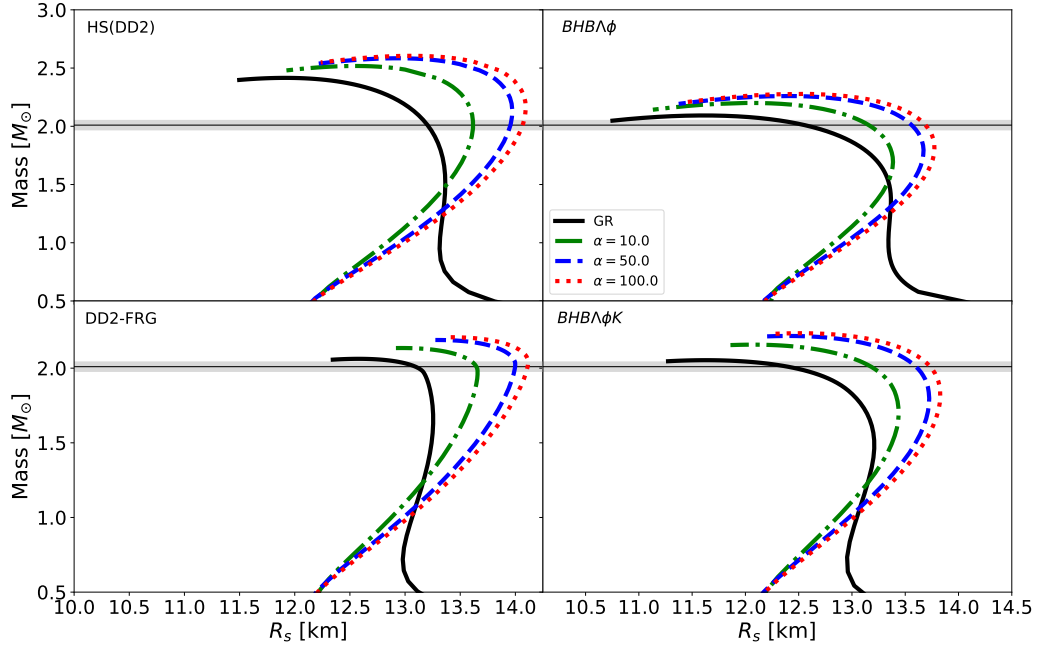


**Figure 4.15:** M-R relation of EoS under study in GR and  $f(R)$  for a range of parameter " $\alpha$ ". The gray band in the figures represent the observational constraints on mass

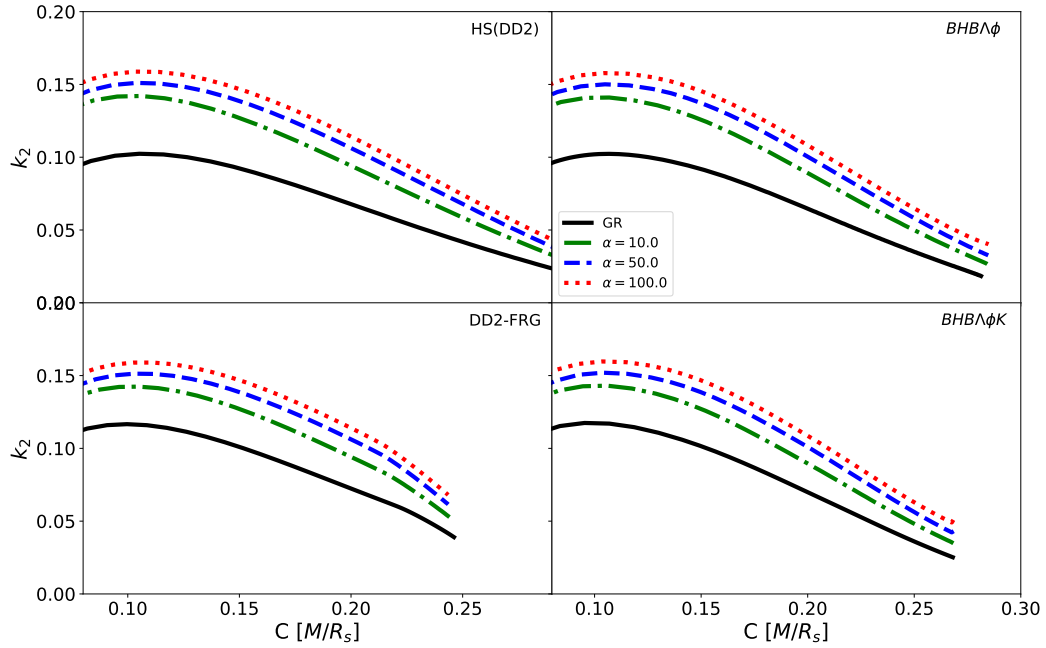
pressure  $P(0)$  and  $\epsilon(0)$ , we integrate from the center of the NS to its surface with boundary conditions of  $[m(0) = 0]$  at the center and  $[P(R_s) = 0]$  on the surface to obtain total mass  $[M = m(R_s)]$  of the NS enclosed within the radius  $R_s$ . In figure 4.15, we represent these using black solid lines. The four panels correspond to the four RMF EoS described above. The impact of strangeness is clearly visible in comparing these four mass-radius curves. The softer the EoS, the lower the maximum mass it can support. The maximum masses for all these EoS are above  $2M_\odot$ , with DD2 having the highest at  $2.41M_\odot$ . The observational constraints (Antoniadis *et al.*, 2013) are shown by the grey band in the figures. In GR, the radius corresponding to the maximum masses ranges from 9.92 to 12.56 km.

For the same set of realistic EoS, the modified TOV equations [3.22-3.25] of the R-squared gravity model for a spherically symmetric and non-rotating configuration are solved in non-perturbative formalism. The coupled differential equations are numerically integrated using the RK4 method with a step size of 0.001 km. To determine the intermediate energy densities, a spline interpolation was used. The mass and radius for each EoS entry are then computed and plotted. This procedure is then repeated for the value of  $\alpha = 10, 50$ , and 100 and the four different EoS used in this study.

When ' $\alpha$ ' increases, the mass and radius of the NS increase in comparison to the GR mass and radius of the corresponding EoS. The radius of NS at  $1.4M_\odot$  [ $R_{S,1.4}$ ] for all  $\alpha$ , as shown in the table

**Table 4.4:** Data table of maximum mass ( $M_{max}$ ), Radius at  $1.4 M_{\odot}$  ( $R_{S,1.4}$ ), and  $\Lambda$  at  $1.4M_{\odot}$  ( $\Lambda_{1.4}$ ).

$\alpha$ ( $r_g^2$ )	$M_{max}$ ( $M_{\odot}$ )				$R_{S,1.4}$ (km)				$\Lambda_{1.4}$			
	0	10	50	100	0	10	50	100	0	10	50	100
DD2	2.41	2.52	2.59	2.61	13.10	13.31	13.53	13.59	627.05	846.59	1011.52	1087.11
BHBA $\phi$	2.09	2.20	2.26	2.28	13.04	13.24	13.45	13.64	648.33	781.99	933.53	1003.85
DD2-FRG	2.06	2.13	2.19	2.21	13.23	13.34	13.54	13.62	620.22	888.47	1061.15	1139.76
BHBA $\phi$ K	2.05	2.16	2.22	2.23	13.20	13.33	13.54	13.62	689.27	807.68	964.54	1036.10


**Figure 4.16:** Tidal Love Number ( $k_2$ ) versus Compactness ( $C$ ) for density-dependent EoS under study

4.4, is likewise well within the limits of NICER observations  $[13.02^{+1.24}_{-1.06}]$  (Miller *et al.*, 2019). The difference in maximum mass of NS with  $\alpha = 10$  and the GR maximum mass ranges from  $0.072 - 0.109 M_{\odot}$ , whereas the increase in radius  $R_{S,1.4}$  ranges from  $0.12 - 0.31$  km. For  $\alpha = 50$ , the maximum mass varies from  $0.126 - 0.174 M_{\odot}$ , while the increase in radius  $R_{S,1.4}$  is within  $0.32 - 0.54$  km; and for  $\alpha = 100$ , maximum mass varies from  $0.144 - 0.196 M_{\odot}$ , while the increase in radius  $R_{S,1.4}$  is within  $0.39 - 0.61$  km. DD2 has the highest mass among the EoS, both in GR and  $f(R)$ . In GR, introducing  $\Lambda$  hyperon,  $K^-$ , and quarks to the EoS significantly decreases the maximum mass. Similar behaviour is seen for different values of  $\alpha$  in  $f(R)$ .

Figure 4.16 shows the relationship between  $k_2$  and  $C$  (dimensionless compactness) for each EoS. The graphs show that when  $\alpha$  grows, the  $k_2$  value related to compactness rises substantially compared to the GR values. Given a fixed EoS, the value of  $k_2$ , compared to the GR value, can range between

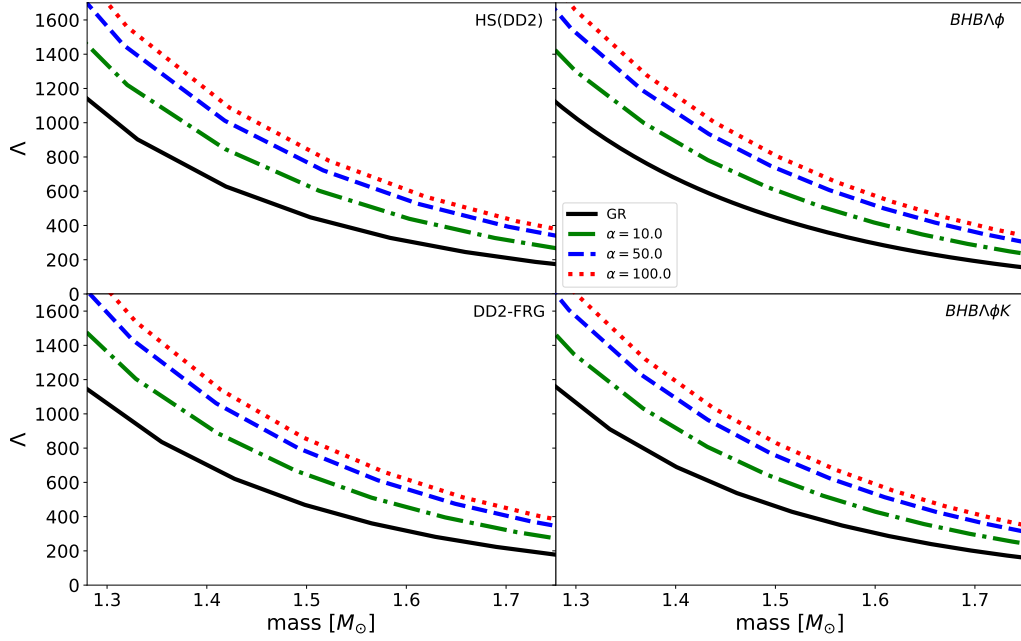


**Figure 4.17:** The neutron star tidal deformability ( $\Lambda$ ) versus mass for the EoSs under study

24 – 62% for the analyzed range of  $\alpha$  values. In the case of GR, the value of  $k_2$  at  $1.4M_\odot$  [ $k_{2,1.4}$ ] is in the 0.089 – 0.098 range. However, when  $\alpha$  increases, we notice that for  $\alpha = 10$ ,  $k_{2,1.4}$  ranges from 0.120 – 0.124, which is a 24 – 37% increase; for  $\alpha = 50$ ,  $k_{2,1.4}$  ranges from 0.133 – 0.137, which is a 38 – 52% increase; for  $\alpha = 100$ ,  $k_{2,1.4}$  ranges from 0.142 – 0.145, which is a 46 – 62% increase. In GR, the introduction of  $\Lambda$  hyperon,  $K^-$ , and quarks to the EoS increases the value of  $k_{2,1.4}$ . In  $f(R)$ , however, although adding quarks to the EoS increases the value of  $k_{2,1.4}$ , adding  $\Lambda$  hyperon,  $K^-$  reduces the value of  $k_{2,1.4}$  for various values of  $\alpha$ .

Figure 4.17 depicts the tidal deformability versus mass for each EoS. The figures show that when  $\alpha$  grows, so does the value of  $\Lambda$  corresponding to mass at  $1.4M_\odot$  [ $\Lambda_{1.4}$ ], in comparison to the similar values in GR. The difference in  $\Lambda_{1.4}$  of NS with  $\alpha = 10$  compared to GR  $\Lambda_{1.4}$  is 118.41 – 268.25, which amounts to a 17 – 43% rise. For  $\alpha = 50$ , the  $\Lambda_{1.4}$  ranges from 275.27 to 440.94, corresponding to a 40 – 71% increase; and for  $\alpha = 100$ , it varies from 346.83 to 519.54, corresponding to a 50 – 84% increase. While all  $\alpha$  up to 100 were permitted by the constraints on mass and radius, we observe that GW170817 constraint on the tidal deformability indicates that value of  $\alpha$  should be less than 10 for all EoSs.

The addition of quark matter to nucleons only EoS decreases the value of  $\Lambda_{1.4}$  in the case of GR, but increases the value in the case of  $f(R)$ . Among all the EoS, the quark EoS has the greatest values



of  $\Lambda_{1.4}$  in  $f(R)$ . The addition of kaons and hyperons to nucleons only EoS, increases the value of  $\Lambda_{1.4}$  within GR, but decreases for various values of  $\alpha$  in  $f(R)$ .

### 4.3.2 Conclusions

In this work, we studied spherically symmetric, non-rotating neutron stars using the TOV equations derived from the non-perturbative  $f(R)$  gravity method (Yazadjiev *et al.*, 2014). For this purpose, we used relativistic mean field EoS with density-dependent couplings  $DD2$  model EoS. We considered EoS based on the  $DD2$  model since we aim to study the influence of exotic particles (such as  $\Lambda$ ,  $K^-$ , and quark) under modified gravity. The nucleonic and exotic EoS fulfil the NS maximum mass constraints. We investigated the mass versus radius, compactness versus tidal Love number ( $k_2$ ), and mass versus tidal deformability relations for EoS.

We observed that, while the addition of exotic particles decreases the maximum mass for all  $\alpha > 0$ , the addition of  $\Lambda$  and  $K^-$  decreases the  $\Lambda_{1.4}$  for all  $\alpha > 0$ . However, adding quarks increases the  $\Lambda_{1.4}$ . The maximum-mass constraint permits a large range of  $\alpha$  (from 0 – 100) values in  $f(R)$  gravity. To improve this, we investigated the acceptable range of values for  $\alpha$  using tidal deformability in light of GW170817 results (Abbott *et al.*, 2018). We are able to constrain the value of  $\alpha$  to be smaller than 10 for the type of EoS that this research investigated. We focused on the EoS based on a density-dependent relativistic mean field model with nucleonic and exotic degrees of freedom. Tidal deformability in  $f(R)$  is always greater than in GR for every given  $\alpha > 0$ . In  $f(R)$ , some very soft EoS, excluded in GR, may fulfill the observable constraints of tidal deformability. They, however, never achieve the maximum mass criterion and thus be ruled out.

## Chapter 5

# Role of Pulsars in Gravitational Wave Science

*"Research is the process of going up alleys to see if they are blind."* – Marston Bates

## 5.1 Introduction

Gravitational waves (GW) are perturbations in the fabric of spacetime that result from the motion of massive bodies including compact objects such as black holes and neutron stars, as predicted by Einstein's theory of general relativity. The first indirect detection of GW was made from observing a binary pulsar system PSR 1913 + 16 (Hulse, 1994; Weisberg and Taylor, 1981; Weisberg *et al.*, 2010). The first direct detection was made from a merger of inspiraling black holes (Abbott *et al.*, 2016). Pulsars can be useful in detecting GW. They are rapidly rotating neutron stars that emit electromagnetic radiation beams. Radio telescopes on Earth can detect these beams and their regular pulses make them useful for precise timing measurements. When a GW travels through the Earth, it produces a very minor stretching and squeezing of spacetime, causing a slight change in the arrival times of the pulsar's pulses. This change, known as a "gravitational wave-induced timing perturbation," is measurable and can be utilized to detect GW. Pulsar timing arrays are particularly sensitive to GW in the low-frequency range (nanohertz).

### 5.1.1 Gravitational Wave Spectrum

The discovery of GW signalled the beginning of a new era in astronomy. GW are a new class of tools for exploring new frontiers in astronomy and fundamental physics. The GW spectrum is believed to be in the range of  $10^{-17} - 10^3$  Hz.

**Table 5.1:** Each gravitational wave detector uses different principles to sense the tiny distortions in spacetime caused by passing gravitational waves

Type of Detector	Frequency Range (Hz)	Reference
Cosmic Microwave Background Polarisation	$10^{-17} - 10^{-15}$	<a href="#">Kamionkowski and Kovetz (2016)</a> <a href="#">Ade et al. (2016b,a)</a>
Pulsar Timing Arrays	$10^{-8} - 10^{-6}$	<a href="#">Lentati et al. (2015)</a> <a href="#">Shannon et al. (2013)</a> <a href="#">Demorest et al. (2013)</a>
Laser-Interferometer Space Antenna	$10^{-6} - 10$	<a href="#">Amaro-Seoane et al. (2017)</a>
Advanced Laser Interferometer Gravitational wave Observatory	$10 - 10^3$	<a href="#">Abbott et al. (2016)</a>

### 5.1.2 Pulsar Timing Arrays

The ground-and space-based experiments like LIGO and LISA measure GW by observing the changing path lengths in the arms of laser interferometers. In 1979, Detweiler theorised that an Earth-pulsar baseline can work as a GW antenna, potentially sensitive to GW of frequencies in the nanohertz range ([Detweiler, 1979](#)). A collection of such galactic millisecond pulsars (MSPs) distributed evenly across the sky is called a Pulsar Timing Array (PTA). In 1983, Hellings & Downs ([Hellings and Downs, 1983](#)) constrained the background of GW radiation using the cross-correlations in pulsar signals. They were able to predict that, depending on the type of GW source, the correlations would be a function of the angular separation of the pulsars. This enables stochastic gravitational wave background (SGWB) to be detected as the source of certain correlated signals across an array of pulsars.

Under the aegis of The International Pulsar Timing Array (IPTA: [Hobbs et al., 2010](#); [Perera et al., 2019](#)) PTAs ([Foster and Backer, 1990](#)) like the European Pulsar Timing Array (EPTA: [Kramer and Champion, 2013](#); [Desvignes et al., 2016](#); [Chen et al., 2021](#)), the Indian Pulsar Timing Array (InPTA: [Joshi et al., 2018](#)), the North American Nanohertz Observatory for Gravitational Waves (NANOGrav: [McLaughlin, 2013](#); [Demorest et al., 2013](#); [Arzoumanian et al., 2015, 2018](#); [Alam et al., 2020a,b](#)), and the Parkes Pulsar Timing Array (PPTA: [Hobbs, 2013](#); [Manchester et al., 2013](#); [Kerr et al., 2020](#)) are experiments that use an ensemble of MSPs as a galaxy-sized astrophysical detector to detect GW in the nanohertz frequency range. These efforts, in tandem with rapidly developing PTA campaigns in China ([Lee, 2016](#)) and South Africa ([Bailes et al., 2016](#)), are expected to kick off the area of nHz GW astronomy in the near future ([Goncharov et al., 2021](#); [Arzoumanian et al., 2021](#); [Chen et al., 2021](#)).

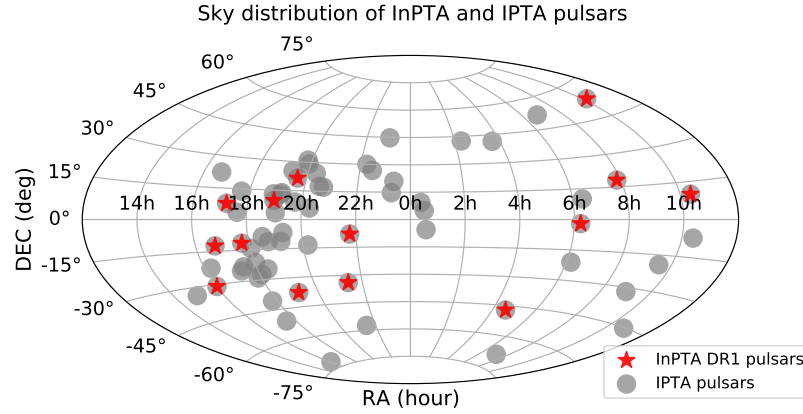


**Figure 5.1:** The sky distribution of those 14 pulsars observed during the InPTA experiment that are included in the present data release is indicated by red stars, whereas that used in the IPTA Data Release 2 is marked with grey circles.

### 5.1.3 The InPTA Experiment

The Indian Pulsar Timing Array experiment<sup>1</sup> started as a pilot campaign using the legacy GMRT and the Ooty Radio Telescope (ORT: [Swarup \*et al.\*, 1971](#)) in 2015. The experiment is conducted by an Indo-Japanese collaboration of about 40 researchers hailing from various institutions. During this pilot phase of the experiment, we tested our observation and data analysis strategies, defined the pulsar sample, and obtained preliminary timing solutions for folding the pulsar time-series data. The InPTA started using the new capabilities of the upgraded GMRT since April 2018. The initial sample for the experiment consisted of 22 pulsars which were observed once every 15 days. As the collaboration experimented with different observing strategies, the number of observed pulsars ranged from 5 to 22. A discussion of these limitations during the initial phases of the experiment is beyond the scope of this thesis. All such observation strategies are elaborated in [Joshi \*et al.\* \(2022\)](#). The sky distribution of the 14 selected pulsars from the full InPTA sample that are included in the data release is shown in Figure 5.1 in comparison with the sample used in the International Pulsar Timing Array Data Release 2 (IPTA DR2: [Perera \*et al.\*, 2019](#)). Except for a hiatus of 6 months during 2019, at least 5 pulsars have been routinely observed for the last three and a half years using the uGMRT since the beginning of the main InPTA experiment. The first data release of the InPTA, consisting of data products for 14 pulsars, is made publicly available. The details of the InPTA observations and data analysis are presented in the forthcoming sections.

### 5.1.4 Brief Introduction to Pulsar Timing

In general, pulsars are very faint objects. For the vast majority of pulsars, single pulses are often almost hard to detect. As a result, the pulse train is phase-wrapped throughout the whole period of

<sup>1</sup><https://inpta.iitr.ac.in/>

observations in order to get the signal-to-noise ratio (S/N) ratio of the pulse profile for detection. The fact that the neutron star's revolutions can be counted is the basis of pulsar timing, and each detected pulse may thus be assigned an integer (Lorimer and Kramer, 2012). The spin frequency  $f$  in the pulsar's reference frame in a Taylor expansion can be written as follows:

$$f(t) = f(t_0) + \dot{f}_0(t - t_0) + \frac{1}{2}\ddot{f}_0(t - t_0)^2 + \dots \quad (5.1)$$

where  $f(t_0)$  is the spin frequency and  $\dot{f}_0$  and  $\ddot{f}_0$  are the derivatives at some reference epoch  $t_0$ . The higher derivatives of  $f$  are generally ignored unless there is a significant spin down evolution for any particular pulsar. Since spin frequency  $f$  is the rate of change of pulse number  $N$ , from 5.1 we can write

$$N = N_0 + f_0(t - t_0) + \frac{1}{2}\dot{f}_0(t - t_0)^2 + \dots \quad (5.2)$$

where  $N_0$  is the pulse number at the reference epoch  $t_0$ .

The non-inertial frame of the Earth-based observatory, the orbit of a binary pulsar, and the intervening interstellar medium account for the majority of the uncertainties in the timing model. Each of these introduces delays and alters the transformed time of arrivals (ToAs) observed at the observatory. These delays can be parameterized into few observational quantities, such as the sky position of the pulsar, its parallax (distance) and proper motion, the Keplerian orbital parameters, and the column density of free electrons along the line of sight to the pulsar, also known as dispersion measure (DM). A timing model is then constructed out of these parameters.

This radiation traversing the intervening interstellar medium (ISM) gets dispersed due to the presence of free electrons. The interstellar dispersion alters the group-velocity of the electromagnetic signal, retarding the arrival of pulses by a time  $t_{DM}$  (relative to an infinite frequency signal) according to the cold-plasma dispersion law

$$t_{DM} = \frac{\mathcal{D} \times DM}{\nu^2} \quad (5.3)$$

where dispersion measure integrated column density of electrons in the line of sight of a pulsar

$$DM = \int_0^d n_e dl \quad (5.4)$$

is usually expressed in  $\text{cm}^{-3}\text{pc}$  and the dispersion constant (Lorimer and Kramer, 2012)

$$\mathcal{D} = \frac{e^2}{2\pi m_e c} = 4.148808(3) \times 10^3 \text{MHz}^2 \text{cm}^3 \text{pc}^{-1} \text{s} \quad (5.5)$$

Since the dispersion is inversely proportional to the frequency, radio signals are affected the most due to the ISM. Traditional timing experiments observe pulsars in the gigahertz frequencies due to a steep power-law spectrum at these frequencies and also to avoid the propagation effects that arise due to the signal travelling through the ISM.

The parameters of the timing model can be constrained to a very high precision based on several measurements of the observed ToAs. After generating the ToAs, the ToA predictions from the timing model can be subtracted, leaving the 'timing residuals'. Following that, the timing model can be revised or expanded to minimise these timing residuals.

### **Narrowband analysis**

To obtain accurate measurements of pulsar timing residuals, pulsar data is often divided into different frequency bands. A template-matching method is applied to calculate the band-averaged ToA from a one-dimensional template profile (Manchester *et al.*, 2013; Desvignes *et al.*, 2016). The relative phase offsets of the template and observed pulse profiles can be determined using cross-correlation, allowing the ToA to be calculated. Various cross-correlation techniques can be utilised, primarily dependent on the S/N of the observation. Another common method is to create "subbanded" ToAs by keeping some of the frequency resolution of the profile data and measuring a ToA in each subband or channel with the same, constant one-dimensional template profile to take care of profile evolution to some extent (Arzoumanian *et al.*, 2015; Demorest *et al.*, 2013; Arzoumanian *et al.*, 2018). These types of analyses were used in the early days of the timing experiment when the observations were made in bandwidths on the order of 100 MHz or less, and these methods do not make use of all of the information contained in the current broadband observations.

### **Wideband analysis**

Wideband receivers and backends are becoming more widely available, opening up new potential for high precision timing using wideband timing (WT) techniques (Pennucci *et al.*, 2014; Liu *et al.*, 2014). These high precision measurements are critical for PTAs, like the EPTA, InPTA, NANOGrav, and PPTA, and IPTA which integrates data and resources from several PTA projects to search for nanohertz gravitational waves. Not only does this technique provide high precision ToAs, but it also produces simultaneous estimates of the DM variations for the MSPs being timed. The WT technique has been used

on datasets such as the 12.5-year NANOGrav dataset (Alam *et al.*, 2020b). In this work, we present the first application of this technique to low frequency (below 400 MHz) observations, which complements the recent application in the 400-800 MHz frequency range utilising CHIME and GBT-L data (Fonseca *et al.*, 2021).

Here are some technical details of the methodology used in the `PulsePortraiture` package, which is the workhorse behind the WT analysis used in this work. More details can be found in Pennucci *et al.* (2014); Pennucci (2019). The wideband data processing can be divided into three stages using the following modules: `ppalign`, `ppspline`, and `pptoas`. We now describe each of these modules below.

- `ppalign`: The first step in `PulsePortraiture` involves creating a two-dimensional template, containing the pulse amplitude as a function of the frequency and phase. This step is done in the `ppalign` module. Each phase-frequency sub-integration in the data set is called a data “portrait”. The starting point in constructing this portrait is nearly the same as in the traditional analysis, which consists of an iterative procedure of co-adding all the significant total intensity profiles at all frequencies in a given band (Demorest, 2007). The only difference is that instead of aligning each data portrait compared to a constant profile portrait using only a phase shift, each profile is rotated by a factor proportional to the inverse-square of its frequency. By doing so, we can minimize the dispersive delays caused by DM changes, which could smear the average portrait. This iterative process is carried out multiple times to create a final average portrait. Regardless of averaging, the choice of alignment is covariant with the absolute DM. In our analysis, we used a single epoch data to construct the portrait since the signal to noise ratio was reasonably high.
- `ppspline`: This module does the principal component analysis (PCA) decomposition of the average portrait, followed by reconstruction of the template profile based on the significant eigenvectors. We apply PCA to the average portrait profiles, whose dimensions are  $n_{chan} \times n_{bin}$ , where  $n_{chan}$  are the total number of frequency bins and  $n_{bin}$  are the total number of phase bins, which encompass the observed bandwidth and pulsar profile, respectively. Unlike conventional PCA, we do not select the optimum basis vectors (here referred to as eigenprofiles) based on the largest eigenvalues, in order to avoid getting contaminated by radiometer noise. Instead, we choose the top 10 eigenprofiles ranked according to their S/N. In order to determine the S/N, the mean profile as well as the eigenprofiles were first smoothed using Stationary Wavelet Transform based denoising, and the S/N was then calculated using the definition in Arzoumanian *et al.* (2015).

The mean-subtracted profiles are projected onto each of the eigenprofiles to obtain a set of coordinate coefficients. A low-degree spline function is fitted to these coefficients, which is parameterized by frequency and encompasses the evolution of the pulse profile shape. By linearly combining the eigenprofiles  $e_i$  using the spline coefficients  $B_i$  and adding it to the mean profile  $\tilde{p}$ , a template profile  $T(\nu)$  at any frequency  $\nu$  can be created as follows:

$$T(\nu) = \sum_{i=1}^{n_{eig}} B_i(\nu) \hat{e}_i + \tilde{p} \quad (5.6)$$

- `pptoa`: In this step, the DMs and ToAs are calculated. The ToA and DM pair from each observation are obtained by minimizing the  $\chi^2$  value as follows (Pennucci *et al.*, 2014),

$$\chi^2 = \sum_{n,k} \frac{|d_{nk} - a_n t_{nk} e^{-2\pi i k \phi_n}|^2}{\sigma_n^2}. \quad (5.7)$$

Equation 5.7 takes the same form as the conventional ToA likelihood used in the Fourier-domain phase-gradient shift algorithm (Taylor, 1992), except here there is an additional index  $n$ , which labels the frequency channel with center frequency  $\nu_n$ .  $k$  is the index corresponding to the Fourier frequency, which is conjugate to the rotational phase or time. The other terms in the equation are as follows:  $d_{nk}$  is the discrete Fourier transform of the data profiles,  $\sigma_n^2$  are their corresponding Fourier domain noise levels,  $t_{nk}$  is the discrete Fourier transform of the template profiles,  $a_n$  are the scaling amplitudes for each template profile, and  $\phi_n$  are the phase shifts applied to each template profile. The two fitted parameters of interest,  $\phi_0$  (which corresponds to the ToA) and the DM, arise because the phase offsets  $\phi_n$  for each profile are constrained to follow the cold-plasma dispersion law:

$$\phi_n(\nu_n) = \phi_0 + \frac{\mathcal{D} \times \text{DM}}{P_s} (\nu_n^{-2} - \nu_{\phi_0}^{-2}), \quad (5.8)$$

where  $P_s$  is the instantaneous spin period of the pulsar,  $\mathcal{D}$  is the dispersion constant ( $4.148808(3) \times 10^3 \text{ MHz}^2 \text{ cm}^3 \text{ pc}^{-1} \text{ s}$ ). The ToAs and DMs are simultaneously fit for in such a way that there is zero covariance between them. The ToAs and DMs are then written to a file.

A likelihood that is implemented in the pulsar timing software package TEMPO (Nice *et al.*, 2015) effectively uses the wideband DM measurements from the ToAs as priors on the DM model parameters.



Details of this procedure can be found in Appendix B of [Alam \*et al.\* \(2020b\)](#). Therefore, the wideband analysis of InPTA data simultaneously yields a DM timeseries as well as the residuals with respect to the fitted ephemeris. These are shown in Figures 5.4 and 5.5. The spin parameters – namely the rotational frequency ( $F_0$ ), its first derivative ( $F_1$ ), and the orbital Keplerian parameters – namely the orbital period ( $P_b$ ), the projected pulsar semi-major axis ( $a_p \sin i$ ), longitude and the epoch of periastron passage ( $\omega, T_0$ ) are fitted. As we do not expect to improve the positional parameters of the pulsar over the six-month time-span of our data, these are not fitted. We also did not fit the solar wind model. The Barycentric Dynamical Time (TDB) ([Guinot and Seidelmann, 1988](#)) is specifically designed to account for the effects of both special and general relativity on the measurement of time. DE436 ([Folkner and Park, 2016](#)) ephemeris is a set of mathematical models and data tables used to calculate the positions and velocities of celestial bodies in our solar system. TDB and DE436 are used throughout the analysis. The parameter files used in this analysis are taken from the NANOGrav 12.5-year data release (NG: [Alam \*et al.\*, 2020b](#)).

## 5.2 Application of Wideband Method to Low-Frequency Observations

**Nobleson, K., et al.** *Low-Frequency Wideband Timing of InPTA Pulsars Observed With the uGMRT*. Monthly Notices of the Royal Astronomical Society, 512(1):1234 (2022). <sup>2</sup>

Pulsars are bright at frequencies less than 1 GHz. MSPs' higher signal-to-noise ratio (S/N) at these frequencies may result in higher precision ToAs. However, at such low frequencies, the electron distribution in the ISM has a major effect on the pulse shape and arrival time of the pulsed signal from these pulsars (Cordes *et al.*, 2016). ISM scattering not only broadens the pulsed signal, but also delays it by a factor roughly proportional to its width, resulting in incorrect timing measurements (Levin *et al.*, 2016). Furthermore, because of the dynamic nature of the ISM, the time variability of the DM introduces correlated noise into the GW analysis (Shannon and Cordes, 2017). The signature of the stochastic gravitational wave background (SGWB), produced by an incoherent superposition of GWs from an ensemble of supermassive black hole binaries, is covariant with this ISM noise (Romano and Cornish, 2017). PTAs have traditionally employed higher frequency observations for the search of nanohertz GWs, despite a greater S/N at low radio frequencies, because the magnitude of this noise is significantly larger at low frequencies.

Because ISM noise affects higher frequency observations, PTA experiments often use DM estimations obtained from quasi-simultaneous narrow band observations at two or three widely separated observing frequencies to correct high frequency ToAs (You *et al.*, 2007; Keith *et al.*, 2013; Alam *et al.*, 2020a). In such measurements, the alignment of the fiducial point of the pulse at different observing frequencies is crucial. This can cause systematic bias in observed DMs as well as other pulsar timing parameters (Lentati *et al.*, 2017). Or, one can get precise measurements of the DM by measuring the pulse time of arrivals (ToAs) simultaneously at different frequencies. Furthermore, extreme scattering events (Lentati *et al.*, 2017), DM events (Lam *et al.*, 2018), and profile changes in some of the pulsars, such as PSR J1713+0747, have been observed (Singha *et al.*, 2021; Xu *et al.*, 2021; Meyers and Chime/Pulsar Collaboration, 2021), complicating the GW analysis of the PTA data.

Alternatively, PPTA has used wideband receivers between 700–4000 MHz for more precision DM measurements (Johnston *et al.*, 2021). Wideband techniques applied to such data provide a robust method for correcting profile evolution with frequency as well as ISM noise, including data corruption caused by abrupt ISM events. If a Kolmogorov turbulence is assumed for the ISM, the dispersive delay varies as  $\nu^{-2}$ , whilst the pulse scatter broadening varies as  $\nu^{-4.4}$  (Rickett, 1977; Cordes *et al.*, 1986). While this substantial frequency dependence makes low frequency PTA observations difficult, using wideband

---

<sup>2</sup>This work was done in collaboration with members of Indian Pulsar Timing Array (InPTA)

approaches to observations between 300 – 800 MHz can, in theory, better account for these effects and yield very precise ToAs. Thus, applying this technique to frequencies ranging from 300 to 800 MHz has the potential to make low radio frequency PTA observations just as useful as high frequency observations.

InPTA uses coherently dedispersed wideband observations with the upgraded Giant Metrewave Radio Telescope’s (uGMRT: [Gupta et al., 2017](#)) 300-500 MHz band. We present a proof-of-principle application of the wideband timing technique `PulsePortraiture`<sup>3</sup> ([Pennucci et al., 2016](#)) to such observations for five pulsars in this work. This complements the DM measurements reported in the [Krishnakumar et al. \(2021\)](#), which were computed using the `DMcalc` package.

### 5.2.1 Observations and Data Reduction

The five pulsars used in this study (PSRs J1643–1224, J1713+0747, J1909–3744, J1939+2134, and J2145–0750) are observed since 2018 with a cadence of around 15 days, using the uGMRT. These observations were carried out by dividing uGMRT’s 30 antennas into two sub-arrays. These pulsars are observed in Band 3 (300-500 MHz) and Band 5 (1060-1460 MHz) simultaneously using separate sub-arrays. The nearest 10 central square antennas were included in the Band 3 sub-array, where the data were coherently dedispersed in real-time ([De and Gupta, 2016](#)) and recorded using the GMRT Wideband Backend (GWB: [Reddy et al., 2017](#)) with a 200 MHz band-pass. The number of sub-bands for the recording vary between 64 to 1024 with the sampling time used ranging from 5 to 40  $\mu$ s, respectively. The observation time per pulsar is typically about 55 minutes.

The recorded data were reduced offline using an automated data reduction pipeline `pinta` ([Sobhanan et al., 2021](#)), developed for the InPTA data. Using the known pulsar ephemeris (IPTA DR2: [Perera et al., 2019](#)), this pipeline partially folds the data from all the sub-bands into sub-integrations of 10-second duration to archive files in the `TIMER` format ([van Straten and Bailes, 2011](#)). Radio-frequency interference mitigation was performed by `RFIClean` ([Maan et al., 2021](#)). Before our analysis, all the reduced data were further collapsed in time to a single integration, with 64 sub-bands. In this work, we report the results for the aforementioned five pulsars observed in Cycle 39 of uGMRT covering the period between November 2020 to April 2021. Since our goal is to demonstrate the application of WT at low frequencies, only Band 3 data were used for the work presented here. The selection of these pulsars was made based on the different pulse morphology and a range of observed scatter-broadening in the pulse profiles. PSR J1909–3744 shows systematic changes in DM but also has the best achievable timing solution. PSRs J1643–1224 ([Lentati et al., 2017](#)) and J1939+2134 ([Ramachandran et al., 2006](#)) show large systematics due to a variation in the pulse scatter broadening. PSRs J1713+0747 ([Dolch](#)

---

<sup>3</sup><https://github.com/pennucci/PulsePortraiture>

*et al.*, 2014) and J2145–0750 (Löhmer *et al.*, 2004) are bright pulsars in our sample, which also show scatter broadening, profile evolution, and scintillation in our frequency range apart from epoch to epoch DM variations. Amongst these pulsars, J1909–3744 and J2145–0750 are the best timed pulsars. This diversity of frequency dependent effects in this sample of pulsars is useful to evaluate the efficacy and the systematic errors in the wideband technique.

### 5.2.2 Our Findings

The main goal of this work is to measure the wideband ToAs and DMs for the low-frequency pulsar data in order to study its suitability for PTA experiments. We applied this technique to a sample of five pulsars, which were observed by InPTA, and obtained DM estimates as well as timing residuals.

In a nutshell, Figure 5.4 displays the DM estimations from WT and a comparison to DM values obtained using `DMcalc` (Krishnakumar *et al.*, 2021). The WT DM estimates obtained by measuring each WT ToA are plotted here. Figure 5.5 demonstrates the WT ToAs with a precision of less than  $1 \mu\text{s}$  and rms post-fit residuals of  $1 \mu\text{s}$  or better. The eigenprofiles corresponding to the PCA decomposition of the PSR J1939+2134 data are shown in Figure 5.6. The DM uncertainties obtained using WT and `DMcalc` methods are compared in Figure 5.7. Table 5.2 summarises the results of WT method, whereas Table 5.3 compares the WT and narrowband timing (NT) solutions.

The DM estimations were done by independent WT analyses with varying the number of eigenprofiles, the number of phase bins, as well as the epoch data used to make the average portrait, to understand their effect on the results. We draw the following conclusions based on these tests:

1. In Figure 5.6 (left panel), we show how the DM estimates correlate with the number of eigenprofiles for PSR J1939+2134. With one and two eigenprofiles, the DM value is underestimated. The first two eigenprofiles span only about 94% of the profile evolution. The first, second, and third eigenprofiles together span about 99% of the profile evolution. When the number of eigenprofiles is three or above, the DM values are consistent within the error bars. On the right panel, the mean profile and eigenprofiles corresponding to the PCA decomposition of PSR J1939+2134 data are plotted for visual reference. The grey points are the computed values from the data and the dark lines are the smoothed curves that comprise the model. Based on similar analysis, the optimum number of eigenprofiles, required for accurate DM estimations for the five pulsars in our sample, are as follows: For PSRs J1643–1224, J1713+0747, and J1939+2134 the DM estimates with  $n_{eig} = 3$  or more are consistent with each other. Therefore, DM estimation can be done with a minimum of three eigenprofiles. For J1909–3744 and J2145–0750, the DM estimates with  $n_{eig} = 2$  or more

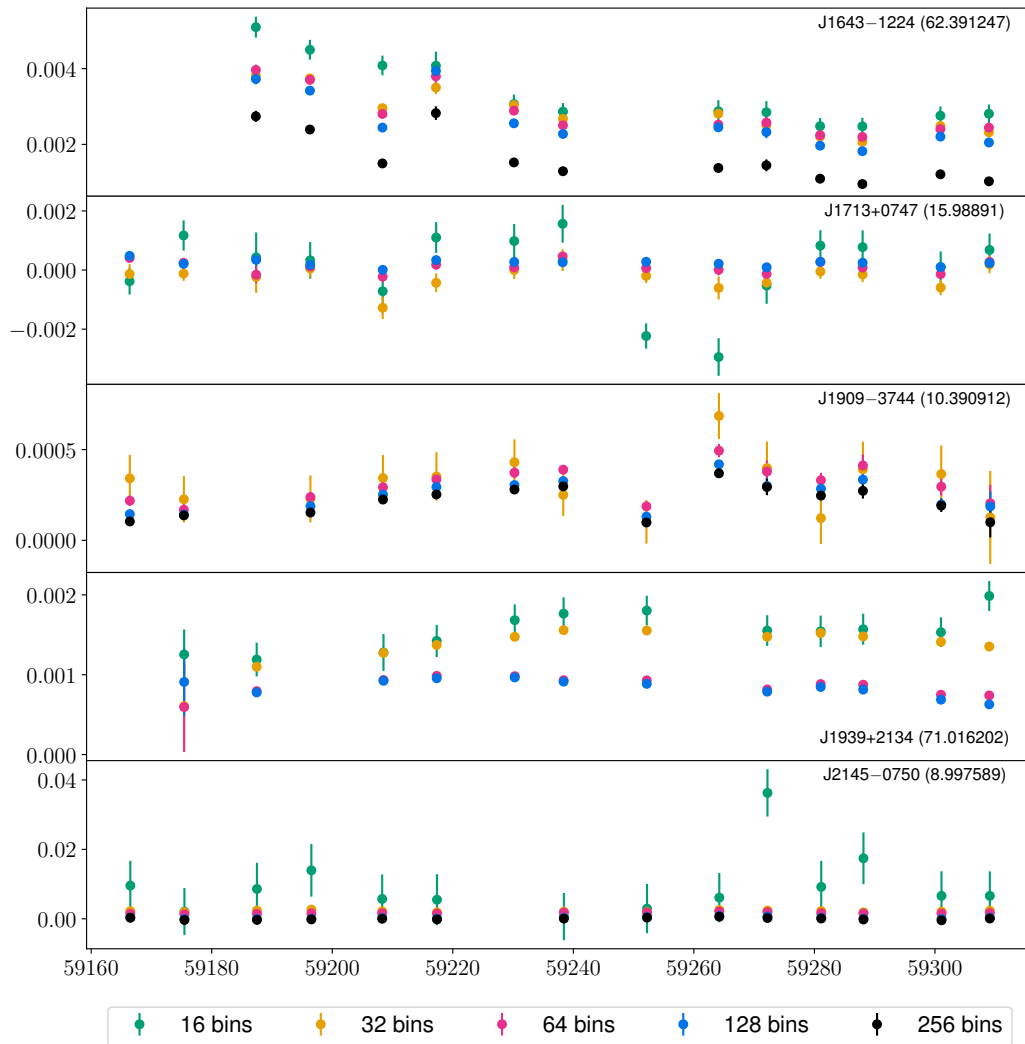


**Figure 5.2:** The fiducial DM-subtracted DM variations are plotted for the pulsars in our sample. Within each subplot, the fiducial DMs that are subtracted are given. The nbins ranges from 16 to 256 in multiples of 2. The DM uncertainties are lower for higher nbins and higher for lower nbins.

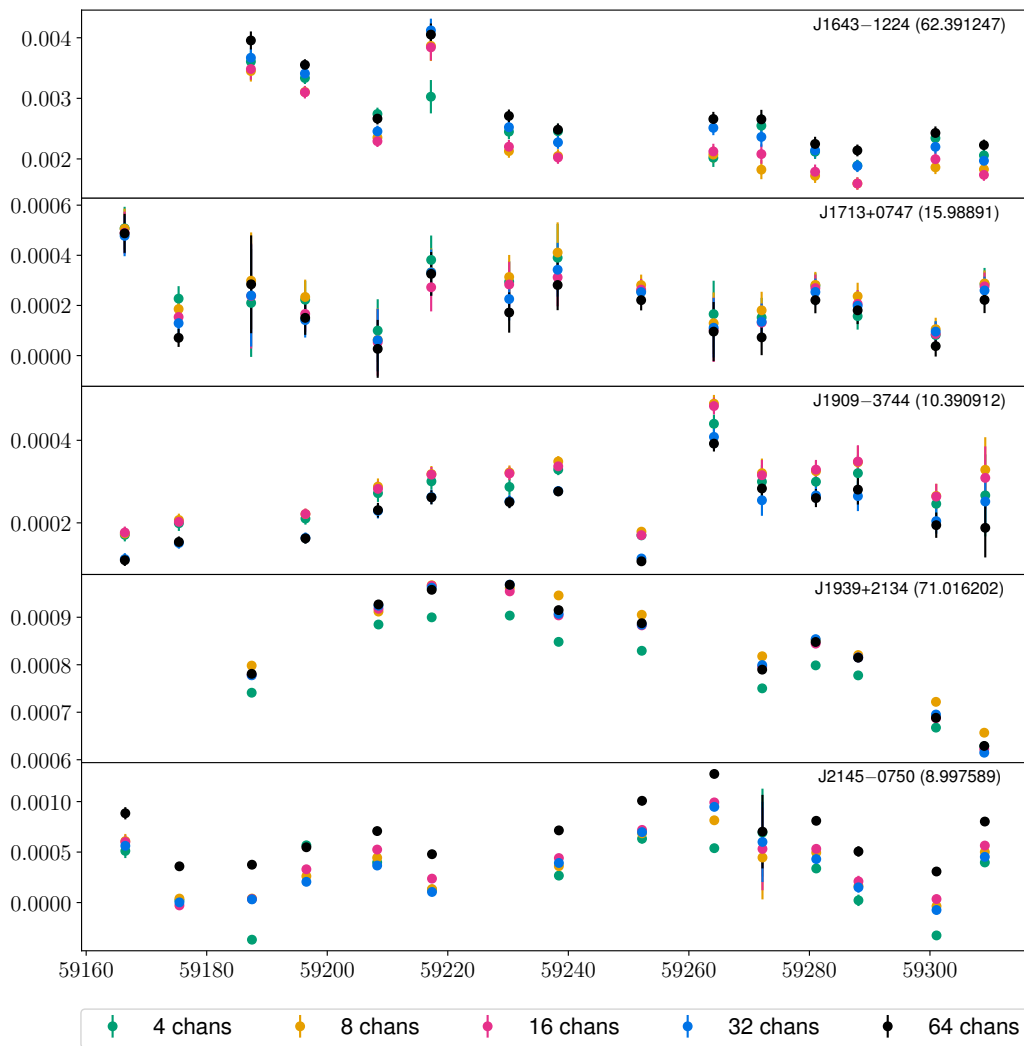


**Figure 5.3:** The fiducial DM-subtracted DM variations are plotted for the pulsars in our sample. Within each subplot, the fiducial DMs that are subtracted are given. The nchan ranges from 4 to 64 in multiples of 2. The DM uncertainties are lower for higher nchan and higher for lower nchan.

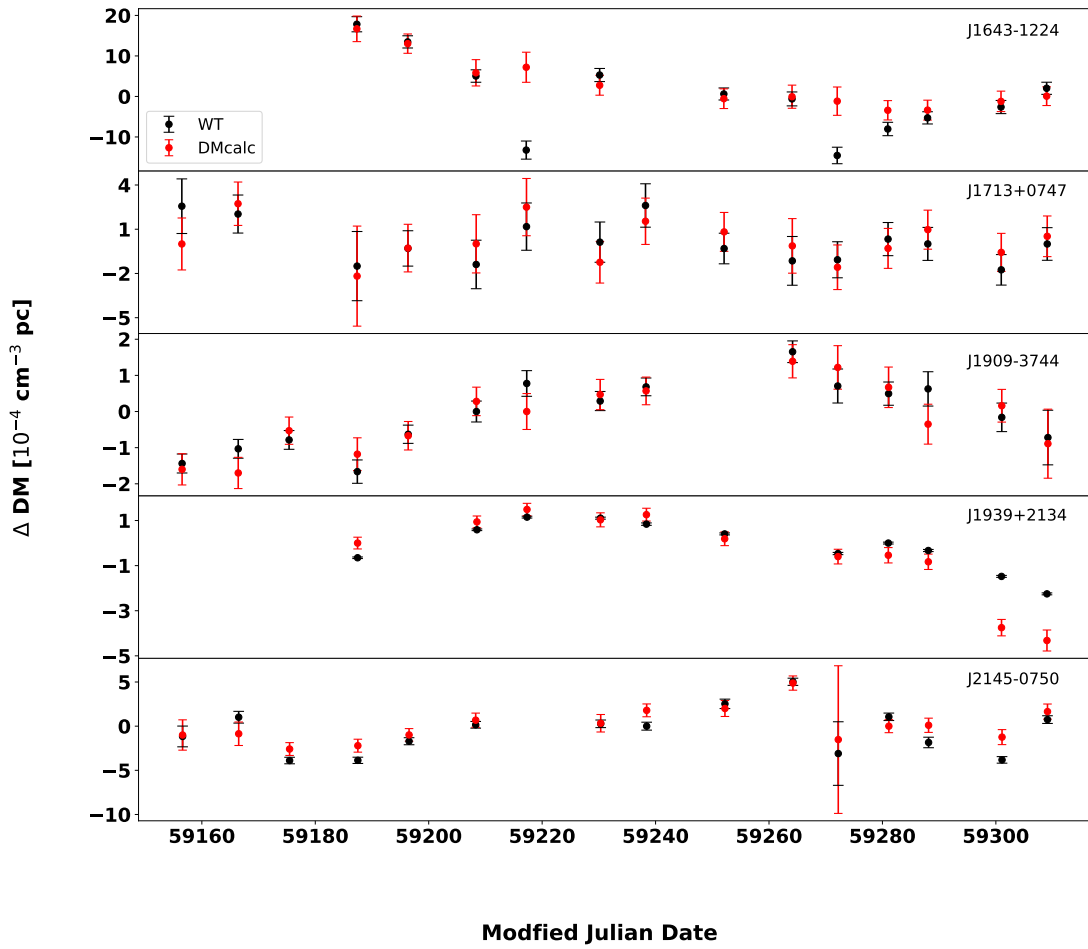


**Figure 5.4:** The median-subtracted DM variations are plotted for the pulsars in our sample observed at uGMRT (400 MHz with 200 MHz bandwidth) from November 2020 to April 2021. The black points correspond to WT and the red points correspond to DMcalc. The median DM uncertainties range from  $3 \times 10^{-6}$  to  $1 \times 10^{-4} \text{ cm}^{-3} \text{ pc}$ . The median DM values and corresponding uncertainties for each pulsar are listed in the Table 5.2.

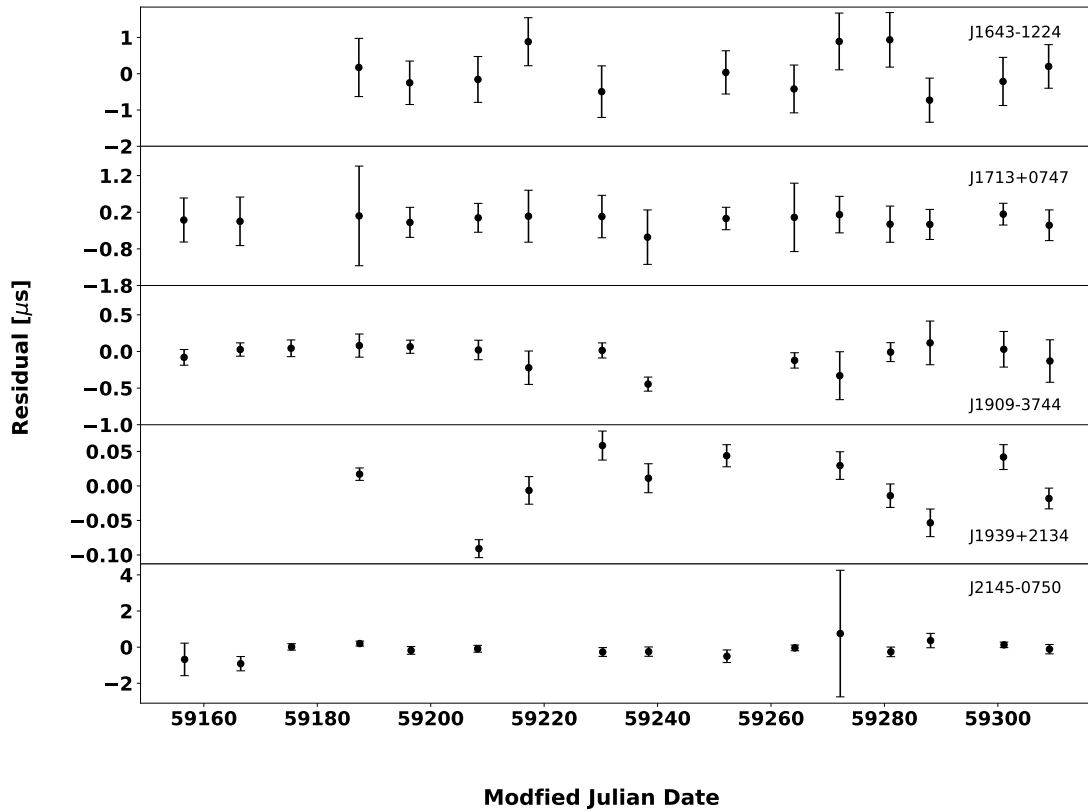


**Figure 5.5:** The timing residuals are plotted for the pulsars in our sample observed at uGMRT (400 MHz with 200 MHz bandwidth) from November 2020 to April 2021. The first three points in PSRs J1643–1224 and J1939+2134 are missing because of non-detection of pulsars in these epochs. The median ToA uncertainties range from 0.02 to 0.66  $\mu\text{s}$ . The ToA uncertainty and postfit rms for each pulsar are listed in the Table 5.2.



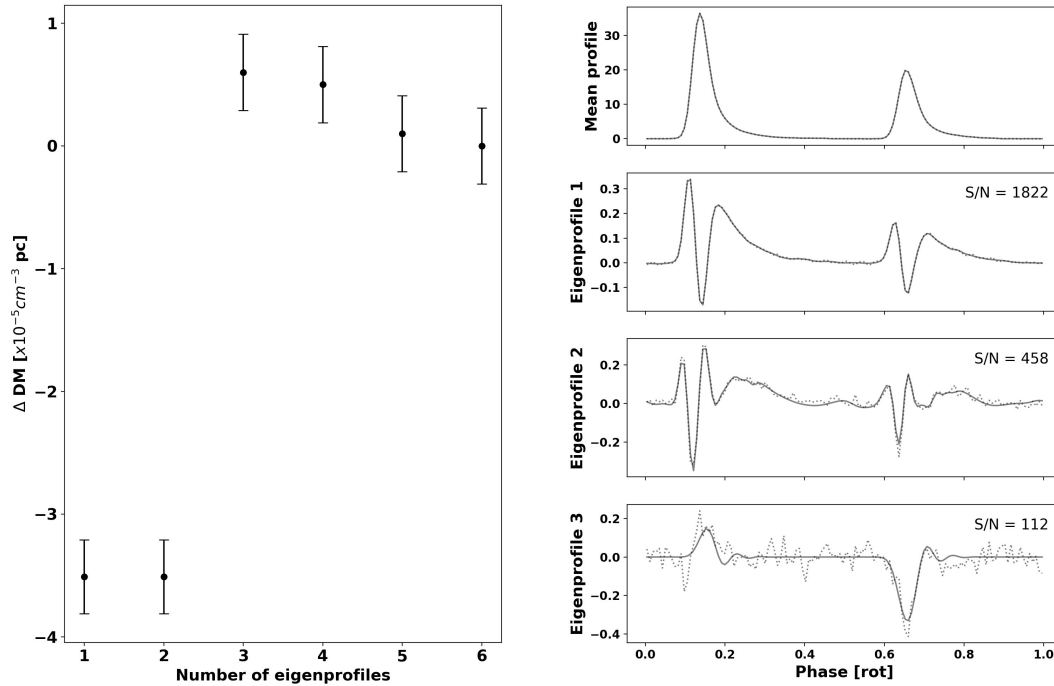


**Figure 5.6:** The plot on the left depicts how the DM estimation varies with the number of eigenprofiles chosen for J1939+2134. On the Y-axis, difference in DM (each result is subtracted from the DM estimate derived using six eigenprofiles) is plotted. A portrait is created using the data from the template epoch. `ppspline` is used to process the portrait by varying the number of eigenprofiles. The DM estimate and the DM uncertainty for each variation is then obtained after processing with `pptoas`. With three or more eigenprofiles, the DM estimates tend to converge. The profile evolution was modelled using three eigenprofiles, the others are presented for illustration purposes. The error bars correspond to the uncertainty in the DM measurement. The mean profile and the eigenprofiles corresponding to the PCA decomposition of PSR J1939+2134 data are presented for visual reference on the right panel. The top three highest S/N profiles are shown here. The median DM is 71.017317. The grey points represent the data's computed values, while the dark lines are the smoothed curves that comprise part of the model.

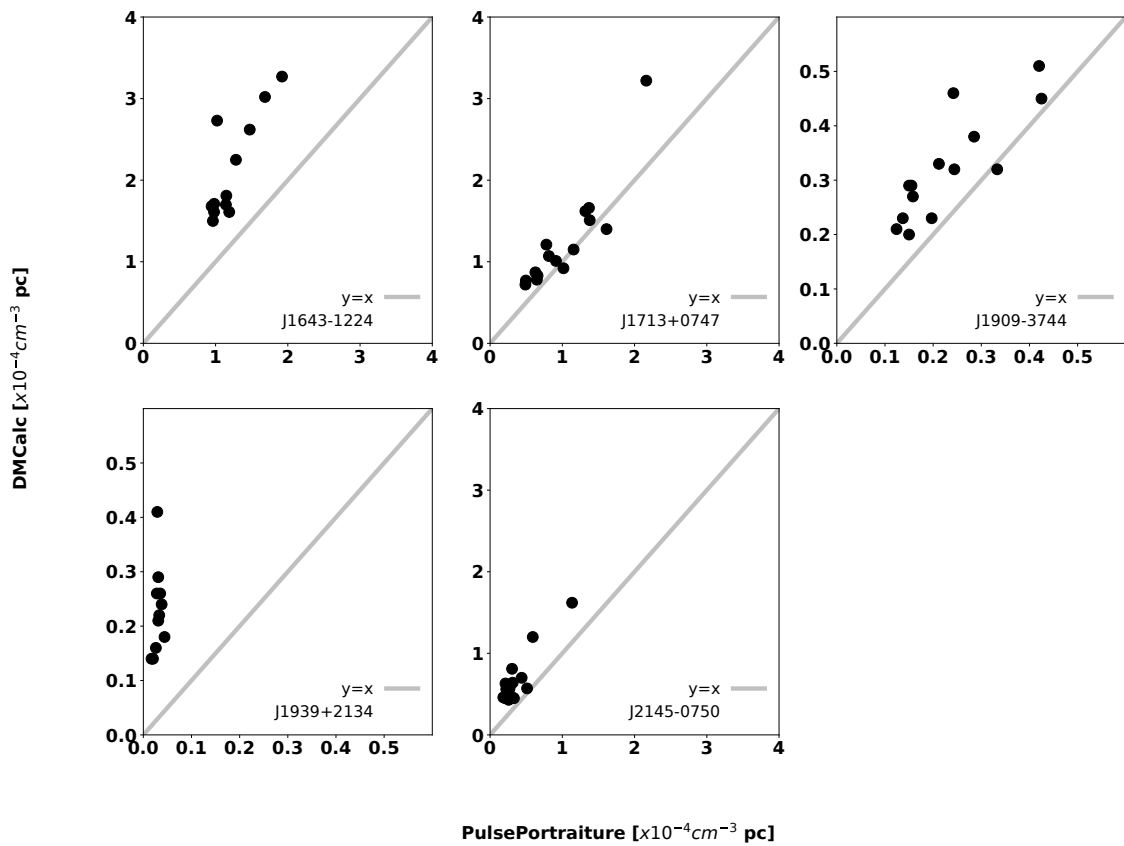


**Figure 5.7:** This plot shows the comparison of the DM uncertainties obtained with DMcalc and PulsePortraiture for the pulsars in our study. With the exception of J1939+2134 and J1643-1224, the uncertainty from both the methods are consistent.

are consistent within the error bars. Therefore, for these pulsars a minimum of 2 eigenprofiles are required.

2. The DM uncertainties are smaller with larger number of phase bins compared to those with smaller number of phase bins. For example, in the case of J1643-1224, the median DM uncertainty with 16 phase bins is  $0.000255 \text{ pc cm}^{-3}$  whereas for 256 phase bins the median DM uncertainty is  $0.000109 \text{ pc cm}^{-3}$ . This is consistent across all the five pulsars in our sample. Also, the timeseries with least number of phase bins has a greater offset from the rest of the timeseries (see figure 5.2).
3. The DM uncertainties are smaller with larger number of frequency channels, compared to those with smaller number of frequency channels. This is consistent across all the five pulsars in our sample (see figure 5.3).
4. The DM estimates obtained using the different averaged portraits have an offset among them. However, the median subtracted DMs are consistent with each other within the error bars. This is consistent across all the five pulsars in our sample.

For our WT analysis, we reduced the data to 64 channels, and one sub-integration for all the pulsars in our sample. PSRs J1643–1224, J1713+0747, and J1909–3744, data have 256 bins; J1939+2134 data have 128 bins; and J2145–0750 data have 1024 bins. The WT results for all the pulsars are summarized in Table 5.2.

Conventional NT ToAs and DM estimation were performed with 4 subbands for J1643–1224, and 16 subbands for J1713+0747, J1909–3744, J1939+2134 and J2145–0750. Frequency-resolved templates were created for each pulsar using a wavelet smoothing algorithm (Demorest *et al.*, 2013), implemented as the `psrsmooth` command in PSRCHIVE (Hotan *et al.*, 2004), on the same epoch data with the same number of bins as used for the wideband templates. These templates were aligned using the same fiducial DMs as the ones used to align the wideband templates. The ToAs were computed from the frequency-resolved profiles using the Fourier Phase Gradient algorithm (Taylor, 1992) available in the `pat` command of PSRCHIVE. The resulting ToAs were then fitted for the DM, spin-down parameters  $F_0$  and  $F_1$ , and the binary parameters orbital period (PB), projected pulsar semi-major axis of the orbit (A1), and epoch of periastron passage of the orbit (T0), Epoch of ascending node passage (TASC) (where applicable) using TEMPO2 (Edwards *et al.*, 2006; Hobbs *et al.*, 2006). In addition, the epoch-by-epoch DM variations were modeled by fitting for the ‘DMX’ parameters in the pulsar ephemeris. DMX is a piecewise-constant representation of the DM variability that is included in the timing model. A separate

DM is estimated for each DMX epoch range based on the  $\nu^{-2}$  dependence of the ToAs that fall within that epoch range. These DMX model parameters are fitted simultaneously together with the rest of the timing model free parameters. Note that we do not fit for the overall DM simultaneously with the DMX parameters as they are covariant with each other.

To compare and contrast the results from WT, we also used `DMcalc` to obtain the DMs at each epoch. `DMcalc` is a script written to automate many of the steps in obtaining DM from each epoch using the PSRCHIVE Python interface and `TEMP02`. In this method, we use a high S/N, frequency resolved template to obtain the ToAs and estimate DM using them for every epoch. Huber regression is used to remove the large outlier ToAs before estimating the DM using `TEMP02`. We made a high S/N template for each pulsar by using the `psrsmooth` program of PSRCHIVE. Similar to WT, the data from the same epoch and same channel resolution (64 channels) are used. The data of each of these pulsars are passed through `DMcalc` along with the above created high S/N templates and the parameter files as used in WT method (without the DMX values and after updating the DM value to the one with which the template is aligned). The DM timeseries of each of the epochs is obtained. The DM estimates from WT, NT, and `DMcalc` have offsets among them. J1939+2134 has the smallest difference in median DMs, which is  $2.7 \times 10^{-5} \text{ cm}^{-3} \text{ pc}$ , between WT and `DMcalc`. The maximum offset is seen for J1643–1224, which is  $1.4 \times 10^{-2} \text{ cm}^{-3} \text{ pc}$ , between WT and `DMcalc`.

We now check how the DM estimates from WT compare with the DM estimates derived from the recently published `DMcalc` method. To establish a correlation (if any) between the general trends in `DMcalc` DM estimates and WT DM estimates, we performed a Spearman’s rank correlation test (Ivezić *et al.*, 2014). The correlation coefficients and  $p$ -values for each pulsar are listed in Table 5.2. The  $p$ -values are computed assuming that the null hypothesis corresponds to no correlation between the pair of datasets. Since the  $p$ -values are  $< 10^{-2}$ , it implies that the DM values between the two measurements are correlated. In Figure 5.4, the median subtracted DM timeseries for WT and `DMcalc` for the five pulsars are shown. It can be seen that the DM precision obtained, in general, is about  $\mathcal{O}(10^{-4}) \text{ cm}^{-3} \text{ pc}$  or better. The timing residuals after fitting the selected parameters for each of the pulsars are shown in Figure 5.5. The results of the ephemeris fit and comparison between WT and NT methods are consolidated in Table 5.3.

PSR	ToA uncertainty ( $\mu\text{s}$ )	Postfit rms ( $\mu\text{s}$ )	Median DM ( $\text{cm}^{-3} \text{pc}$ )	DM precision ( $\times 10^{-4} \text{cm}^{-3} \text{pc}$ )	Best DM precision ( $\times 10^{-5} \text{cm}^{-3} \text{pc}$ )	DMcalc PulseProfile Spearman Coefficient ( $\rho$ )	$p$ -value
J1643–1224	0.66	0.53	62.40859	1.1	9.4	0.67	$1 \times 10^{-2}$
J1713+0747	0.50	0.13	15.98957	0.9	4.9	0.58	$2 \times 10^{-2}$
J1909–3744	0.13	0.07	10.39113	0.2	1.2	0.84	$8 \times 10^{-5}$
J1939+2134	0.02	0.04	71.017317	0.03	0.2	0.92	$4 \times 10^{-5}$
J2145–0750	0.26	0.20	8.99820	0.3	1.8	0.82	$2 \times 10^{-4}$

**Table 5.2:** Summary of the results of the PulseProfile analysis. Column 2 shows the median of the ToA uncertainties for each pulsar. J1939+2134 has the best ToA uncertainty in our sample. Column 3 shows the postfit rms for each pulsar. J1939+2134 has the best postfit rms in our sample. Column 4 shows the median of the DM obtained for each pulsar. Column 5 contains the median of all the DM uncertainties. Column 6 contains the best DM precision for each pulsar (precision refers to the uncertainty in the measurements). J1939+2134 has the best DM precision in the  $\mathcal{O}(10^{-6})$ . Column 7 shows the Spearman’s rank correlation coefficient for the comparison between DMcalc and PulseProfile. The last column shows the  $p$ -value corresponding to the null hypothesis of no correlation. J1939+2134 shows the highest correlation and J1713+0747 shows the least correlation between the two methods.

A comparison of the results for each of the pulsars is summarized below.

**1. PSR J1643–1224**

For this pulsar, the median DM estimate from the WT analysis is  $62.40859 \text{ cm}^{-3} \text{ pc}$ . The DMcalc median DM estimate is  $62.39397 \text{ cm}^{-3} \text{ pc}$ . The DM measurements obtained with these two methods are correlated with a correlation coefficient of 0.67 and  $p$ -value of  $1 \times 10^{-2}$ . The median S/N of this pulsar is 343. The median ToA uncertainty from WT is  $0.66 \mu\text{s}$  with a postfit rms of about  $0.53 \mu\text{s}$ . In comparison, NG reports a median ToA uncertainty of  $0.46 \mu\text{s}$  at 1.4 GHz. Our precision is just a factor of 1.5 lower than NG.

**2. PSR J1713+0747**

For this pulsar, the median DM estimate from WT analysis is  $15.98957 \text{ cm}^{-3} \text{ pc}$ . The median DM estimate from DMcalc is  $15.99003 \text{ cm}^{-3} \text{ pc}$ . The DM measurements obtained with these two methods are correlated with a correlation coefficient of 0.58 and  $p$ -value of  $2 \times 10^{-2}$ . The median S/N of this pulsar is 178, which is the least in our sample. The median ToA uncertainty from WT is  $0.50 \mu\text{s}$  with a postfit rms of about  $0.13 \mu\text{s}$ . In contrast, NG reports a median ToA uncertainty of  $0.043 \mu\text{s}$  at 1.4 GHz. Our precision is a factor of 12 lower than NG.

**3. PSR J1909–3744**

For this pulsar, the median DM estimate from WT analysis is  $10.39113 \text{ cm}^{-3} \text{ pc}$ . The median DM estimate from DMcalc is  $10.39085 \text{ cm}^{-3} \text{ pc}$ . The DM measurements obtained with these two methods are highly correlated with a correlation coefficient of 0.84 and  $p$ -value of  $8 \times 10^{-5}$ . The median S/N for this pulsar is 261. This pulsar has a sharp pulse profile with no scatter broadening. The median ToA uncertainty from WT is  $0.13 \mu\text{s}$  with a postfit rms of about  $0.07 \mu\text{s}$ . In contrast, NG reports a median ToA uncertainty of  $0.086 \mu\text{s}$  at 1.4 GHz. Our precision is just a factor of 1.5 lower than NG.

**4. PSR J1939+2134**

For this pulsar, the median DM estimate from WT analysis is  $71.017317 \text{ cm}^{-3} \text{ pc}$ . The median DM estimate from DMcalc of  $71.017344 \text{ cm}^{-3} \text{ pc}$ . The DM measurements obtained with these two methods are highly correlated with a correlation coefficient of 0.92 and  $p$ -value of  $4 \times 10^{-5}$ . The median S/N for this pulsar is 1175, which is the best in our sample. The median ToA uncertainty from WT is  $0.02 \mu\text{s}$  with a postfit rms of about  $0.04 \mu\text{s}$ . In contrast, NG reports a median ToA uncertainty of  $0.01 \mu\text{s}$  at 1.4 GHz. Our precision is a factor of 2 lower than NG.

### 5. PSR J2145–0750

For this pulsar, the median DM estimate from WT analysis is  $8.99820 \text{ cm}^{-3} \text{ pc}$ . The median DM estimate from `DMcalc` is  $9.00315 \text{ cm}^{-3} \text{ pc}$ . The DM measurements obtained with these two methods are highly correlated with a correlation coefficient of 0.82 and  $p$ -value of  $2 \times 10^{-4}$ . The median S/N for this pulsar is 851. The median ToA uncertainty from WT is  $0.26 \mu\text{s}$  with a postfit rms of about  $0.20 \mu\text{s}$ . In comparison, NG reports a median ToA uncertainty of  $0.48 \mu\text{s}$  at 1.4 GHz. Our precision is a factor of 1.8 better than NG.

After submitting this work for peer-review, we continued to work on further refining the method of DM estimation and found that dedispersing the template with an updated DM measurement, flagging the channels which contained radio frequency interference (RFI) improved the correlations and the DM trends.

Parameters	WT	WTU	NT	NTU	NT-WT	(NT-WT)/NTU	WTU/NTU
						dimensionless	dimensionless
<b>J1643–1224</b>							
$F_0$ (Hz)	216.3733404539	$3.35 \times 10^{-10}$	216.3733404535	$1.32 \times 10^{-9}$	$-4.14 \times 10^{-10}$	0.315	0.255
$A_1$ (1s)	25.072541	$5.32 \times 10^{-6}$	25.072556	$2.07 \times 10^{-5}$	$1.54 \times 10^{-5}$	0.748	0.258
$P_b$ (d)	147.01721	$2.68 \times 10^{-5}$	147.01726	$1.03 \times 10^{-4}$	$5.37 \times 10^{-5}$	0.521	0.260
Reduced $\chi^2$	30.5						
Dof	6						
<b>J1713+0747</b>							
$F_0$ (Hz)	218.811843783	$6.60 \times 10^{-9}$	218.811843781	$8.02 \times 10^{-9}$	$-2.78 \times 10^{-9}$	0.347	0.824
$F_1$ (Hz/s)	$-3.98 \times 10^{-16}$	$2.14 \times 10^{-17}$	$-3.89 \times 10^{-16}$	$2.60 \times 10^{-17}$	$9.16 \times 10^{-18}$	0.353	0.823
$A_1$ (1s)	32.3424241	$9.42 \times 10^{-7}$	32.3424270	$1.11 \times 10^{-6}$	$2.90 \times 10^{-6}$	2.622	0.852
$P_b$ (d)	67.8251289	$5.42 \times 10^{-7}$	67.8251293	$5.72 \times 10^{-7}$	$3.84 \times 10^{-7}$	0.672	0.948
Reduced $\chi^2$	2.2						
Dof	9						
<b>J1909–3744</b>							
$F_0$ (Hz)	339.315692408	$2.38 \times 10^{-9}$	339.315692396	$4.52 \times 10^{-9}$	$-1.16 \times 10^{-8}$	2.565	0.526
$F_1$ (Hz/s)	$-1.66 \times 10^{-15}$	$7.62 \times 10^{-18}$	$-1.62 \times 10^{-15}$	$1.45 \times 10^{-17}$	$3.69 \times 10^{-17}$	2.550	0.526
$A_1$ (1s)	1.8979913	$2.67 \times 10^{-7}$	1.8979907	$5.20 \times 10^{-7}$	$-6.13 \times 10^{-7}$	1.179	0.513
$P_b$ (d)	1.533449455	$1.09 \times 10^{-9}$	1.533449442	$1.92 \times 10^{-9}$	$-1.30 \times 10^{-8}$	6.765	0.571
Reduced $\chi^2$	8.37						
Dof	9						
<b>J1939+2134</b>							
$F_0$ (Hz)	641.9282322513	$8.48 \times 10^{-10}$	641.9282322461	$9.85 \times 10^{-9}$	$-5.25 \times 10^{-9}$	0.533	0.086
$F_1$ (Hz/s)	$-4.32 \times 10^{-14}$	$2.96 \times 10^{-18}$	$-4.32 \times 10^{-14}$	$3.13 \times 10^{-17}$	$1.60 \times 10^{-17}$	0.513	0.086
Reduced $\chi^2$	192.78						
Dof	9						
<b>J2145–0750</b>							
$F_0$ (Hz)	62.2958888039	$9.37 \times 10^{-10}$	62.2958887957	$3.14 \times 10^{-9}$	$-8.24 \times 10^{-9}$	2.626	0.299
$F_1$ (Hz/s)	$-1.37 \times 10^{-16}$	$2.99 \times 10^{-18}$	$-1.10 \times 10^{-16}$	$9.99 \times 10^{-18}$	$2.62 \times 10^{-17}$	2.624	0.299
$A_1$ (1s)	10.1641104	$5.36 \times 10^{-7}$	10.1641082	$1.72 \times 10^{-6}$	$-2.13 \times 10^{-6}$	1.241	0.312
$P_b$ (d)	6.838902542	$6.92 \times 10^{-9}$	6.838902502	$2.26 \times 10^{-8}$	$-4.04 \times 10^{-8}$	1.784	0.306
Reduced $\chi^2$	19.07						
Dof	10						

**Table 5.3:** Comparison of the WT and NT postfit parameters of the pulsars in our sample are tabulated here. WTU is the wideband timing uncertainty and NTU is the narrowband timing uncertainty.  $F_0$  is the pulsar rotation frequency,  $F_1$  is the pulsar rotation frequency first derivative,  $A_1$  is the projected pulsar semi-major axis in light seconds (1s),  $P_b$  is the period of the binary orbit, and dof is the degrees of freedom (difference between the number of data points and the number of fitted parameters). In the seventh column, the absolute difference is divided by NTU.



### 5.2.3 Conclusions and Discussions

In this work, we demonstrated the application of wideband timing using `PulsePortraiture` on low-frequency (300–500 MHz) data for five millisecond pulsars: PSRs J1643–1224, J1713+0747, J1909–3744, J1939+2134, and J2145–0750, observed at uGMRT as part of the InPTA program. These pulsars show different morphologies in pulse shapes and varying degrees of broadening in their pulse profiles. DM estimates with this technique are consistent with techniques, such as `DMcalc`, which use data with narrow sub-bands. At the same time, this technique simultaneously provides high precision ToAs. PCA analysis, employed for this technique, indicates that we require a minimum of three eigenprofiles for PSRs J1643–1224, J1713+0747, and J1939+2134; and two eigenprofiles for PSRs J1909–3744 and J2145–0750 to capture the profile evolution with frequency. We obtained DM precision ranging between  $3 \times 10^{-6} \text{ cm}^{-3}\text{pc}$  for PSR J1939+2134 to  $1 \times 10^{-4} \text{ cm}^{-3}\text{pc}$  for PSR J1643–1224. Using this method, we get sub-microsecond post-fit average residuals. We achieved the best post-fit residuals of about 40 ns for PSR J1939+2134.

Using the dispersion formula

$$\Delta t = 4.148808 \text{ ms} \times \left[ \left( \frac{f_{lo}}{\text{GHz}} \right)^{-2} - \left( \frac{f_{hi}}{\text{GHz}} \right)^{-2} \right] \times \left( \frac{DM}{\text{cm}^{-3}\text{pc}} \right),$$

(See Appendix A 2.4 [Lorimer and Kramer, 2012](#)), it can be shown that the precision in DM measurements obtained over our 200 MHz bandwidth (e.g., 300–500 MHz)  $\mathcal{O}(10^{-5})$  is at least an order of magnitude better than that over a wide high frequency band (e.g., 700–4000 MHz)  $\mathcal{O}(10^{-4}) \text{ cm}^{-3}\text{pc}$  (for assumed typical  $1 \mu\text{s}$  ToA errors). These 300–500 MHz observations provide a S/N comparable to GHz bandwidth observations at high frequencies as pulsars are much brighter at 400 MHz. In addition, our results show that the application of WT to our band can provide post-fit residuals comparable to high frequency data by taking care of ISM effects considerably. Thus, WT of such low frequency observations is capable of not only providing more accurate DM estimates, but also high precision ToAs directly. An interesting study is to make a direct comparison between the analysis of low and high frequency PTA data in a future IPTA data combination to investigate this further.

We compare these low-frequency ToA residuals and DM uncertainties with the results published in the literature for the same pulsars, both at low `DMcalc` and high frequencies (NG: [Alam et al., 2020b](#)). In the low frequency band, our DM estimates show a strong correlation with the results from `DMcalc`. Now, WT technique has considerable advantages over the traditional timing techniques. Firstly, WT is more amenable to automation with a one-step analysis. In contrast, analysis methods using sub-bands, such as

traditional narrowband analysis or `DMcalc`, require a multi-step iterative approach with DM estimation followed by timing in an iterative loop. Secondly, traditional analysis either ignores profile evolution or pulse broadening or at best approximates it. In contrast, WT incorporates this as an essential ingredient of analysis. In Figure 5.7, we compare the uncertainties from both the methods for these five pulsars. With the exception of PSR J1643-1224 and PSR J1939+2134, the uncertainty from both the methods are consistent. The inconsistency could be related to the fact that we only considered profile evolution and not scattering effects and these pulsars show significant pulse broadening at low frequencies. We plan to investigate this further in a future work. Lastly, the WT technique utilizes the S/N of the entire wideband observations to provide high precision ToA unlike the narrowband technique. This also results in a single high S/N band- averaged ToA rather than 16 to 32 lower S/N ToAs. This significantly reduces the dimensionality of subsequent Bayesian analysis, which is employed for detection of GWs. Thus, the consistency of the DM estimates between the WT and traditional methods provides support for a preferential use of WT technique at low frequencies, in particular, and hint at an increasing reliance on WT technique for future PTA and IPTA data release, in general.

A comparison of the timing solutions obtained from WT and traditional NT are presented in Table 5.3. As is evident from the table, WT produces timing solutions consistent with NT, with typical uncertainties in fitted parameters smaller than NT.

In our application, the pulse broadening was assumed to be stable over the observation epochs. This may not be the case for all the pulsars. An example is PSR J1643–1224, where variable pulse broadening at a given frequency was reported earlier ([Shannon \*et al.\*, 2016](#)). Epoch to epoch variation of the profile evolution with frequency has also been reported in PSR J1713+0747 ([Singha \*et al.\*, 2021](#)). An extension of WT to include such a variation will be interesting and is planned in future. Similar extension to combine widely separated multiple bands is currently underway ([Paladi \*et al.\*, 2023](#)).

A comparison with the median ToA uncertainties at high frequencies, such as those obtained by NG at 1.4 GHz, indicates that our ToA uncertainties are of the same order (1.5 to 2 times), except for one pulsar (PSR J1713+0747). These findings suggest that low frequency data, analysed with WT technique, can provide a precision similar to high frequency data for gravitational wave detection experiments. Given the steep spectrum of radio pulsars, this not only enables high precision measurements with smaller observation duration per pulsar at low frequency (as pulsars are much brighter at these frequencies), but also a higher cadence than currently employed with the same telescope time. Additionally, several weaker MSPs can be included in the PTA ensemble. Not only this can provide a more uniform sky coverage for useful sampling of the Hellings and Downs overlap reduction function ([Hellings and Downs,](#)

1983), but also significantly increase the sensitivity (Siemens *et al.*, 2013) to the stochastic gravitational wave background. Thus, our results suggest that wideband low frequency observations can play at least an equal, if not better role, in PTA experiments.

With the Square Kilometer Array (SKA: Carilli and Rawlings, 2004) telescope becoming available in the near future, wideband observations with SKA-low (200–350 MHz) and SKA-mid (350–1000 MHz) promise to provide high quality data not only for nanohertz gravitational wave discovery, but also for post discovery gravitational wave science. Wideband techniques are likely to play a very important role in analysis of these data from SKA.

### 5.3 Wideband Method in InPTA Data Release 1

Tarafdar, P., Nobleson, K., et al. *The Indian Pulsar Timing Array: First Data Release*. Publications of the Astronomical Society of Australia, 39:e053 (2022).<sup>4</sup>

The work in this paper can be broadly categorized into:

1. Wideband DM timeseries and ToAs (*led by Nobleson K and Prerna Rana*)
2. Narrowband timing residuals (*led by Jaikhomba Singha*)
3. Wideband timing residuals (*led by Jaikhomba Singha and Nobleson K*)
4. DM structure function analysis (*led by Avinash Kumar Paladi*)
5. Investigation of frequency dependence of DM (*led by Prerna Rana*)

Majority of my contributions are focused on obtaining Wideband DM timeseries and Wideband timing residuals. From the experience gained from the pilot study, we extend the application of the WT to 14 pulsars observed using uGMRT ([Gupta et al., 2017](#)).

#### 5.3.1 Observations and Data Processing

In this work, we use observations of 14 pulsars conducted using the uGMRT as part of the InPTA experiment from 2018 to 2021 typically with a bi-weekly cadence. These observations were carried out during observing cycles 34–35 and 37–40 of the uGMRT, where the 30 uGMRT antennae were divided into multiple phased subarrays, simultaneously observing the same source in multiple bands in total intensity mode. During cycles 34–35, the observations were carried out using three subarrays in Band 3 (400–500 MHz), Band 4 (650–750 MHz), and Band 5 (1360–1460 MHz) of the uGMRT with 100 MHz bandwidth, whereas in cycles 37–40, the observations were carried out using two subarrays in Band 3 (300–500 MHz) and Band 5 (1260–1460 MHz) with 200 MHz bandwidth. As observations in Band 4 were carried out only in the earliest two cycles with 100 MHz of bandwidth, this dataset is not included in the present data release. The Band 3 data in all cycles as well as the Band 5 data in cycles 34–35 (except observations between Oct. 20, 2018 and Nov. 14, 2018) were coherently dedispersed using a real-time pipeline ([De and Gupta, 2016](#)) to the known DM of each pulsar. The setup and command files for the observation sessions are prepared using automated scripts developed and maintained by the InPTA members.

The channelized time series data generated by the uGMRT were recorded using the GMRT Wideband Backend (GWB: [Reddy et al., 2017](#)) in a binary raw data format, along with the timestamp at the

---

<sup>4</sup>This work was done in collaboration with members of Indian Pulsar Timing Array (InPTA).

start of the observation in a separate ASCII file. We used a pipeline named `pinta` (Susobhanan *et al.*, 2021) to convert these raw data files into partially folded PSRFITS archives, which can be further analyzed using popular pulsar softwares such as PSRCHIVE (Hotan *et al.*, 2004). The time series data were folded using pulsar ephemerides derived from the IPTA DR2 (Perera *et al.*, 2019). `pinta` accommodates two different methods for RFI mitigation, out of which we use `RFIClean` (Maan *et al.*, 2021) in this work.

All profiles are pre-processed by time-collapsing and applying frequency offset corrections<sup>5</sup> before ToA and DM estimations. Additionally, backend delays introduced by the GWB that depend on the observation settings, described in Reddy *et al.* (2021), must be corrected for to achieve high-precision timing. These corrections are incorporated in the PSRFITS archive headers using the `be:delay` field<sup>6</sup>. The `pat` and `pptoa`<sup>7</sup> commands apply the appropriate corrections to the ToAs generated from such archives.

## Wideband technique

The high precision measurement of DMs and ToAs are crucial to the PTA experiments for nanohertz gravitational wave detection. Various PTAs are now using wideband receivers and associated backends while implementing real-time coherent dedispersion (Gupta *et al.*, 2017; Hobbs *et al.*, 2020), to acquire more precise ToAs. Such wideband measurement helps in incorporating the effects of pulse profile evolution with frequency and DM variations. Hence, it is essential to use a method that estimates ToAs, while including a frequency-dependent model of the average pulse profile. Pennucci *et al.* (2014) and Liu *et al.* (2014) first provided algorithms for the simultaneous measurement of DMs and ToAs from wideband pulsar data, called the "wideband timing technique". The algorithm proposed in Pennucci *et al.* (2014) has been developed into a comprehensive package named `PulsePortraiture`. Further details regarding this technique can be found in Pennucci (2019). The application of this technique has been undertaken on various datasets (Alam *et al.*, 2020b; Fonseca *et al.*, 2021; Nobleson *et al.*, 2022; Kaur *et al.*, 2022; Sharma *et al.*, 2022).

Here, we apply this technique on the InPTA uGMRT dataset of 14 pulsars for estimating the DMs and ToAs. We also compare our results with that of the narrowband technique described in Section 5.1.4. The uGMRT provides a unique advantage to study the effects of ISM in the low-frequency (300-500

---

<sup>5</sup>See Susobhanan *et al.* (2021) for discussion on the frequency labels for uGMRT data implemented in `pinta`. For uGMRT observations carried out between 18/10/2019 and 29/07/2021 using the TGC control system, the frequency labels require an additional +10 kHz correction.

<sup>6</sup>These offset corrections are implemented in the latest version of `pinta` used in this work, although it was not present in the earlier version.

<sup>7</sup>See Section 5.3.1 for more details.

MHz) range. It was recently shown in [Nobleson \*et al.\* \(2022\)](#) that high-precision DMs and ToAs can be obtained using wideband analysis of Band 3 uGMRT observations. Hence, we focus on carrying out the wideband analysis only in Band 3. The implemented procedure is as follows:

1. *Template generation*: In order to estimate DMs and ToAs from our observations, we begin by creating a noise-free template for each pulsar. For this purpose, we identify a high-S/N observation for each pulsar from the latest uGMRT cycle (cycle 41), which lies outside the span of the present data release. We do not add multiple epochs together since the uncorrected DM variations can introduce significant smear in the shape of the average profile, especially at low frequencies. We use the same epoch data file for template generation as used in the narrowband analysis. Upon careful investigation, we also found that it is important to excise frequency channels with any residual RFI from the template epoch, otherwise, we see noisy eigenprofiles upon PCA decomposition of the frequency-resolved template epoch data in the wideband analysis. Hence, we excise the RFI channels from the template epoch using `pazi` command of PSRCHIVE package.
2. *Fiducial DM*: We dedisperse the data from all the epochs, including the template used for cross-correlation, using the fiducial DM estimated in the narrowband technique with an iterative procedure. This is to ensure that the narrowband and wideband procedures use the same fiducial value of DM.
3. *Number of frequency channels*: As mentioned earlier, during the uGMRT Cycles 34 and 35, the InPTA observations were carried out with 100 MHz bandwidth, whereas the later cycles used 200 MHz bandwidth observations. The number of channels (sub-bands) used for the InPTA observations is usually large, and some of these sub-bands may contain a very weak pulsed signal. So, we choose to partially collapse the number of sub-bands such that there is reasonable S/N in each sub-band. On the other hand, we also try to retain the information on profile evolution by not using a significantly low number of sub-bands. Hence, the optimal number of sub-bands determined in our analysis for different pulsars are 16, 32, or 64 for 200 MHz data, and 16 or 32 for 100 MHz data.
4. *Number of eigenprofiles*: For each pulsar, we determined the number of eigenprofiles that are required in the wideband analysis to accurately model the profile evolution. The procedure we followed to select the number of eigenprofiles includes a careful check of the following four points - a) we first look at the eigenprofiles and choose an initial guess for the number of eigenprofiles including all eigenprofiles, which show significant pulsed S/N; b) we then select the most dominant

normalized cumulative eigenvalues augmenting the number chosen in step (a). This ensures that the maximum amount of information on profile evolution is included with the selected eigenprofiles; c) we also make sure that the eigenvectors show significant variation with respect to the radio frequency by checking the parameterized coordinate curve vs. frequency plot [refer to Figure 4 and Equations 5 & 7 of Pennucci (2019)] for all the eigenprofiles; d) finally, we confirm that the DM estimate saturates or matches within the one sigma range for the selected number of eigenprofiles for three randomly chosen epochs. This reaffirms that the choice of the number of eigenprofiles is reasonable to account for the profile evolution.

5. *DM and ToA generation:* Once the number of eigenprofiles are determined, the ToAs and DM timeseries are generated using the `pptoas` module of `PulsePortraiture`.

The wideband timing residuals are generated using the wideband likelihood method described in Appendix B of Alam *et al.* (2020b). This wideband likelihood is implemented in the `TEMPO` (Nice *et al.*, 2015) pulsar timing software package. The wideband DM measurements from the ToAs are used as priors on the DM model parameters. The `par` file obtained in the Narrowband method is transformed to a `TEMPO`-compatible `par` file using `transform` plugin of `TEMPO2`. The same parameters that are fitted in narrowband timing are also fitted in wideband timing for each pulsar. The `EFAC` and `DMEFAC` parameters are used to scale the ToA uncertainties. These parameters are tuned iteratively until the reduced  $\chi^2$  is close to 1.0.

### 5.3.2 Conclusions

In this work, we have presented the first data release of InPTA, which includes the pulse arrival times and DMs for 14 millisecond pulsars observed simultaneously at 300–500 MHz and 1260–1460 MHz bands using the uGMRT. The ToAs and DMs have been calculated using two independent methods: narrowband method as well as the wideband technique. These ToAs and DMs were further used to obtain the timing solutions of these pulsars by fitting the spin, astrometric, and binary parameters in both the narrowband and wideband framework. A comparison showing a broad agreement in the results from the two different techniques has also been demonstrated.

The main contribution of this release is high precision DM estimates. It is possible to minimise the DM noise from 1260–1460 MHz pulse arrival times by correcting these by using the DM estimates from our simultaneous observations. The pulse arrival times in this data release may also be useful in deriving better Gaussian process DM noise models as employed by EPTA and PPTA. Lastly, the direct use of DM time series in DM noise models is a work in progress. The current data sets from the MeerKat and the

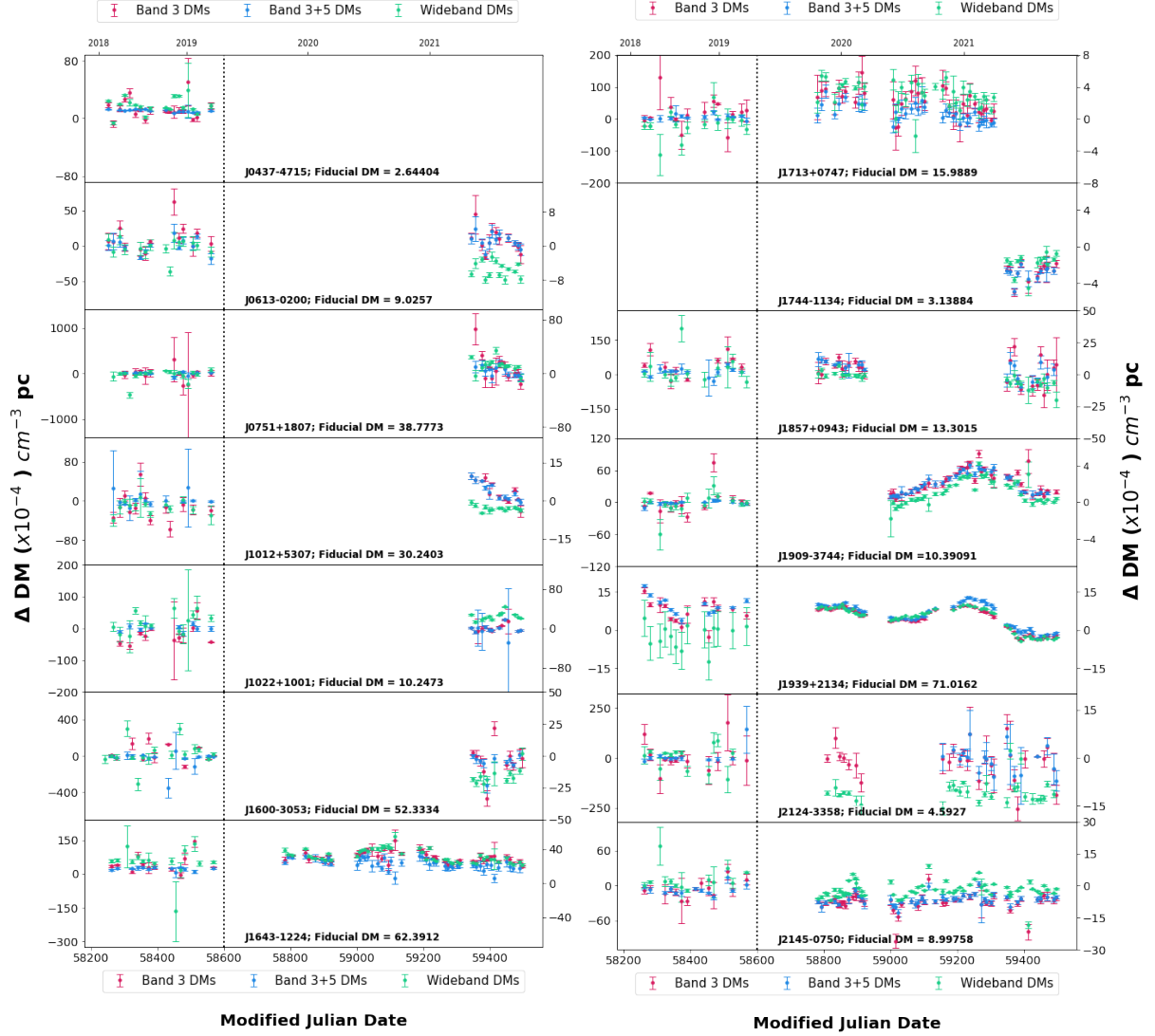


**Figure 5.8:** DM time-series for 14 pulsars. The differences ( $\Delta\text{DM}$  in units of  $10^{-4} \text{ pc cm}^{-3}$ ) between the fiducial DM and the corresponding estimated DMs for each pulsar estimated by (i) fitting only Band 3 narrowband ToAs (red points), (ii) fitting Band 3 and Band 5 narrowband ToAs together (blue points) and (iii) by applying the wideband technique on Band 3 data (green points), are overlaid for comparison. The values depicted on the vertical axis are DMs relative to the fiducial DMs for the respective pulsars that are obtained using an iterative method. Since the precision of DM estimation from 200 MHz bandwidth data is higher than that from 100 MHz bandwidth data, the horizontal axes are split into two parts at MJD 58600 with dotted vertical lines, where epochs on the left side of the dotted line in each panel represent 100 MHz bandwidth, and epochs on the right side of the dotted vertical lines in each panel represent 200 MHz bandwidth. The vertical axes in each panel are also scaled differently for 100 MHz bandwidth (left axis) and 200 MHz bandwidth (right axis) epochs such that the DM variations are clearly visible. Pulsar names and their respective fiducial DM values are mentioned at the bottom of each respective panel. The time span in terms of the years is also denoted at the top for convenience.

FAST are also likely to be DM noise limited like other PTAs, and may benefit from this data release. These data are likely to improve the quality of the proposed IPTA Data Release 3 thereby helping in the detection of GWs in the near future.

Our data for 14 pulsars are now publicly available. Further monitoring of all these pulsars is in



progress as part of the InPTA efforts. We have recently included 3 additional millisecond pulsars to the InPTA sample and are observing a total of 17 pulsars during the ongoing uGMRT cycle. We plan to extend the sample further with simultaneous multi-target observations using multiple phased subarrays. The Target-of-Opportunity proposals are active to follow up on transients such as glitches, profile mode changes, or extreme scattering events in any of the IPTA pulsars observable by the uGMRT. Pulsar-specific proposals with scientific goals that require a higher cadence are being discussed. The 3.5-year dataset for 14 millisecond pulsars that we make available through this first InPTA data release is being pooled along with data from other IPTA telescopes and used to search for nanohertz gravitational waves as well as a whole plethora of auxiliary science.

## Chapter 6

# Conclusions

### 6.1 Summary

Neutron stars are one of the densest stellar objects with matter in extremely high gravitational field regimes, making them useful tools for testing alternative gravity theories. The study of neutron stars is crucial in relativistic astrophysics because it is essential for understanding the final stages of stellar evolution. In the context of modified theories of gravity, the Tolman-Oppenheimer-Volkoff (TOV) equations of stellar hydrostatic equilibrium in neutron stars are modified. This modification has a significant impact on the neutron stars' observational properties. The uncertainty in the equation of state of matter at the enormously high-density core of neutron stars, combined with the new parameters of the modified theory of gravity under consideration, results in a completely new phenomenology for the typical predictions of stable stellar structure models, such as maximum masses and mass-radius relations. They can then be added to the astrophysical observations to constrain the feasibility of the modified gravity model.

In this dissertation, in the theoretical section, we compared the perturbative method and nonperturbative method and showed that the nonperturbative method is the preferred method to derive the TOV equations in  $f(R)$  gravity. We found a universality relationship between the  $f(R)$  gravity model parameter  $\alpha$  and the maximum mass of neutron stars. We also showed that the free parameter in the  $f(R) = R + \alpha R^2$  can be constrained to a value less than 10 (in the units of  $R_g^2$ ) if we account for the observational evidence of tidal deformability from the GW170817 neutron star-neutron star merger event.

In the observational section, we were the first team to demonstrate the application of Pulse Portraiture low-frequency (300-500 MHz) pulsar data and we obtained high precision in DM measurements with precisions of the order of  $10^{-6} \text{ cm}^{-3} \text{ pc}$ . We also estimated the wideband pulse arrival times and high-precision dispersion measure estimates for 14 millisecond pulsars observed simultaneously using the upgraded Giant Metrewave Radio Telescope (uGMRT) in the 300-500 MHz and 1260-1460 MHz

frequency ranges. The data spans 3.5 years (2018-2021), and it is the first official data release from the Indian Pulsar Timing Array collaboration.

Apart from the above works included in this dissertation, contributions were made in other research topics, such as, *Noise analysis in the Indian Pulsar Timing Array Data Release I*, *Multi-band Extension of the Wideband Timing Technique*. I was also part of collaborative studies done between European Pulsar Timing Array and Indian Pulsar Timing Array which showed signs of stochastic gravitational wave background in the nanohertz range. The results are published in the following papers:

- Antoniadis, J., **Nobleson, K.**, et al. *The second data release from the European Pulsar Timing Array II: Customised pulsar noise models for spatially correlated gravitational waves* (2023a), <https://arxiv.org/abs/2306.16225>.
- Antoniadis, J., **Nobleson, K.**, et al. *The second data release from the European Pulsar Timing Array III: Search for gravitational wave signals* (2023b), <https://arxiv.org/abs/2306.16214>.
- Antoniadis, J., **Nobleson, K.**, et al. *The second data release from the European Pulsar Timing Array IV: Search for continuous gravitational wave signals* (2023c), <https://arxiv.org/abs/2306.16226>.
- Antoniadis, J., **Nobleson, K.**, et al. *The second data release from the European Pulsar Timing Array: V: Implications for massive black holes, dark matter and the early Universe* (2023d) <https://arxiv.org/abs/2306.16227>.

## 6.2 Future Scope of Work

The study of neutron stars in  $f(R)$  gravity has provided insights into distribution characteristics of the free parameter  $\alpha$  for a select subset of EoS. However, there exists an opportunity for an investigation that encompasses a broader spectrum of EoS presently available. This holds the potential to ascertain the universality of the currently established relationship across a diverse set of EoS. Furthermore, as precise measurements of maximum mass, radii, and tidal deformability of neutron stars are made available by new observations, this presents an avenue for further refinement of constraint on the free parameter  $\alpha$ .

In the future, we would like to extend this work in a model-independent approach by examining different families of EoS to analyze various universal relations, such as the "I-Love-Q" and "C-Love" (Yagi and Yunes, 2013; Chan *et al.*, 2014) relationships in the context of  $f(R)$  gravity as these are already well investigated in GR.

In this present investigation, we have implemented the wideband method in the Band 3 frequency range (300-500 MHz) of uGMRT. Given the diverse frequency bands used in pulsar observations, an intriguing opportunity emerges to enhance the precision of DM through the combination of two or more non-contiguous frequency bands within the wideband framework.

# Bibliography

- Abbott, B. P., *et al.* (LIGO Scientific Collaboration and Virgo Collaboration). *Observation of Gravitational Waves from a Binary Black Hole Merger*. Phys. Rev. Lett., 116:061102. doi:10.1103/PhysRevLett.116.061102 (2016).
- Abbott, B. P., *et al.* *GW170817: Measurements of Neutron Star Radii and Equation of State*. Physical Review Letters, 121(16):161101. doi:10.1103/PhysRevLett.121.161101 (2018). ISSN 0031-9007.
- Abbott, B. P. *et al.* (LIGO Scientific, Virgo). *Properties of the Binary Neutron Star Merger GW170817*. Phys. Rev. X, 9(1):011001. doi:10.1103/PhysRevX.9.011001 (2019).
- Ade, P. A. R., *et al.* (Keck Array and BICEP2 Collaborations). *Improved Constraints on Cosmology and Foregrounds from BICEP2 and Keck Array Cosmic Microwave Background Data with Inclusion of 95 GHz Band*. Phys. Rev. Lett., 116:031302. doi:10.1103/PhysRevLett.116.031302 (2016a).
- Ade, P. A. R., *et al.* *Planck 2015 Results*. Astronomy & Astrophysics, 594:A13. doi:10.1051/0004-6361/201525830 (2016b). ISSN 0004-6361.
- Alam, M. F., *et al.* *The NANOGrav 12.5-Yr Data Set: Observations and Narrowband Timing of 47 Millisecond Pulsars*. The Astrophysical Journal Supplement Series, 252(1):4. doi:10.3847/1538-4365/abc6a0 (2020a). ISSN 1538-4365.
- Alam, M. F., *et al.* *The NANOGrav 12.5-Yr Data Set: Wideband Timing of 47 Millisecond Pulsars*. The Astrophysical Journal Supplement Series, 252(1):5. doi:10.3847/1538-4365/abc6a1 (2020b). ISSN 1538-4365.
- Altıparmak, S., C. Ecker, and L. Rezzolla. *On the Sound Speed in Neutron Stars*. The Astrophysical Journal Letters, 939(2):L34. doi:10.3847/2041-8213/ac9b2a (2022). ISSN 2041-8205.
- Amaro-Seoane, P., *et al.* *Laser Interferometer Space Antenna*. arXiv preprint arXiv:1702.00786 (2017).

- Antoniadis, J., *et al.* *A Massive Pulsar in a Compact Relativistic Binary.* *Science*, 340(6131). doi: 10.1126/science.1233232 (2013). ISSN 0036-8075.
- Aparicio Resco, M. *et al.* *On Neutron Stars in  $f(R)$  Theories: Small Radii, Large Masses and Large Energy Emitted in a Merger.* *Phys. Dark Univ.*, 13:147. doi:10.1016/j.dark.2016.07.001 (2016).
- Arapoğlu, S., C. Deliduman, and K. Y. Ekşi. *Constraints on Perturbative  $f(R)$  Gravity via Neutron Stars.* *Journal of Cosmology and Astroparticle Physics*, 2011(07):020. doi:10.1088/1475-7516/2011/07/020 (2011). ISSN 1475-7516.
- Arzoumanian, Z., *et al.* *The NANOGrav Nine-Year Data set: Observations, Arrival Time Measurements, and Analysis of 37 Millisecond Pulsars.* *The Astrophysical Journal*, 813(1):65. doi: 10.1088/0004-637X/813/1/65 (2015). ISSN 1538-4357.
- Arzoumanian, Z., *et al.* *The NANOGrav 11-Year Data Set: High-precision Timing of 45 Millisecond Pulsars.* *The Astrophysical Journal Supplement Series*, 235(2):37. doi:10.3847/1538-4365/aab5b0 (2018). ISSN 1538-4365.
- Arzoumanian, Z., *et al.* (NANOGrav Collaboration). *Searching for Gravitational Waves from Cosmological Phase Transitions with the NANOGrav 12.5-Year Dataset.* *Phys. Rev. Lett.*, 127:251302. doi: 10.1103/PhysRevLett.127.251302 (2021).
- Ashton, G. and S. Khan. *Multiwaveform Inference of Gravitational Waves.* *Physical Review D*, 101(6):064037. doi:10.1103/PhysRevD.101.064037 (2020). ISSN 2470-0010.
- Ashton, G. *et al.* *Bilby: A User-friendly Bayesian Inference Library for Gravitational-wave Astronomy.* *The Astrophysical Journal Supplement Series*, 241(2):27. doi:10.3847/1538-4365/ab06fc (2019). ISSN 1538-4365.
- Astashenok, A. V. *Neutron Star Models in Frames of  $f(R)$  Gravity.* In *AIP Conference Proceedings*, pages 99–104 (2014). doi:10.1063/1.4891121.
- Astashenok, A. V., S. Capozziello, and S. D. Odintsov. *Nonperturbative Models of Quark Stars in  $f(R)$  Gravity.* *Physics Letters B*, 742:160. doi:10.1016/j.physletb.2015.01.030 (2015). ISSN 03702693.
- Baade, W. and F. Zwicky. *On Super-Novae.* *Proceedings of the National Academy of Sciences*, 20(5):254. doi:10.1073/pnas.20.5.254 (1934). ISSN 0027-8424.

- Babichev, E. and D. Langlois. *Relativistic Stars in  $f(R)$  and Scalar-Tensor Theories*. Physical Review D, 81(12):124051. doi:10.1103/PhysRevD.81.124051 (2010). ISSN 1550-7998.
- Bailes, M., *et al.* *MeerTime - The MeerKAT Key Science Program on Pulsar Timing*. In *Proceedings of Science*, page 011. Sissa Medialab, Trieste, Italy (2016). ISSN 18248039. doi:10.22323/1.277.0011.
- Baiotti, L. *Gravitational Waves From Neutron Star Mergers and Their Relation to the Nuclear Equation of State*. Progress in Particle and Nuclear Physics, 109:103714. doi:10.1016/j.ppnp.2019.103714 (2019). ISSN 01466410.
- Bandyopadhyay, D., *et al.* *Moment of Inertia, Quadrupole Moment, Love Number of Neutron Star and Their Relations with Strange-Matter Equations of State*. The European Physical Journal A, 54(2):26. doi:10.1140/epja/i2018-12456-y (2018). ISSN 1434-6001.
- Banik, S. and D. Bandyopadhyay. *Third Family of Superdense Stars in the Presence of Antikaon Condensates*. Physical Review C, 64(5):055805. doi:10.1103/PhysRevC.64.055805 (2001). ISSN 0556-2813.
- Banik, S. and D. Bandyopadhyay. *Density Dependent Hadron Field Theory for Neutron Stars with Antikaon Condensates*. Physical Review C, 66(6):065801. doi:10.1103/PhysRevC.66.065801 (2002). ISSN 0556-2813.
- Banik, S., M. Hempel, and D. Bandyopadhyay. *New Hyperon Equations of State for Supernovae and Neutron Stars in Density-Dependent Hadron Field Theory*. The Astrophysical Journal Supplement Series, 214(2):22. doi:10.1088/0067-0049/214/2/22 (2014). ISSN 1538-4365.
- Bauswein, A., *et al.* *Neutron star Radius Constraints from GW170817 and Future Detections*. The Astrophysical Journal, 850(2):L34. doi:10.3847/2041-8213/aa9994 (2017). ISSN 2041-8213.
- Bekenstein, J. and R. Sanders. *A Primer to Relativistic MOND Theory*. EAS Publications Series, 20:225. doi:10.1051/eas:2006075 (2006). ISSN 1633-4760.
- Bertotti, B., F. De Felice, and A. Pascolini. *10th International Conference on General Relativity and Gravitation. Contributed Papers* (1983).
- Birrell, N. D. and P. C. W. Davies. *Quantum Fields in Curved Space*. Cambridge Monographs on Mathematical Physics. Cambridge University Press (1982). doi:10.1017/CBO9780511622632.

- Biscoveanu, S., E. Thrane, and S. Vitale. *Constraining Short Gamma-Ray Burst Jet Properties with Gravitational Waves and Gamma-Rays*. The Astrophysical Journal, 893(1):38. doi:10.3847/1538-4357/ab7eaf (2020). ISSN 1538-4357.
- Biscoveanu, S., S. Vitale, and C.-J. Haster. *The Reliability of the Low-latency Estimation of Binary Neutron Star Chirp Mass*. The Astrophysical Journal, 884(2):L32. doi:10.3847/2041-8213/ab479e (2019). ISSN 2041-8213.
- Blanchet, L. *Gravitational Radiation from Post-Newtonian Sources and Inspiralling Compact Binaries*. Living Reviews in Relativity, 17(1):2. doi:10.12942/lrr-2014-2 (2014). ISSN 2367-3613.
- Brans, C. and R. H. Dicke. *Mach's Principle and a Relativistic Theory of Gravitation*. Physical Review, 124(3):925. doi:10.1103/PhysRev.124.925 (1961). ISSN 0031-899X.
- Buchner, J. *et al.* *X-ray Spectral Modelling of the AGN Obscuring Region in the CDFS: Bayesian Model Selection and Catalogue*. Astronomy & Astrophysics, 564:A125. doi:10.1051/0004-6361/201322971 (2014). ISSN 0004-6361.
- Capozziello, S. and G. Lambiase. *The emission of Gamma Ray Bursts as a test-bed for modified gravity*. Physics Letters B, 750:344. doi:10.1016/j.physletb.2015.09.048 (2015). ISSN 03702693.
- Capozziello, S. *et al.* *Mass-Radius Relation for Neutron Stars in  $f(R)$  Gravity*. Physical Review D, 93(2):23501. doi:10.1103/PhysRevD.93.023501 (2016). ISSN 24700029.
- Carilli, C. L. and S. Rawlings. *Science With the Square Kilometer Array: Motivation, key Science Projects, Standards and Assumptions*. New Astron. Rev., 48:979. doi:10.1016/j.newar.2004.09.001 (2004).
- Chan, T. K., *et al.* *Multipolar Universal Relations Between  $f$ -mode Frequency and Tidal Deformability of Compact Stars*. Physical Review D, 90(12):124023. doi:10.1103/PhysRevD.90.124023 (2014). ISSN 1550-7998.
- Char, P. and S. Banik. *Massive Neutron Stars With Antikaon Condensates in a Density-Dependent Hadron Field Theory*. Physical Review C, 90(1):015801. doi:10.1103/PhysRevC.90.015801 (2014). ISSN 0556-2813.
- Chen, W.-C. and J. Piekarewicz. *Building Relativistic Mean Field Models for Finite Nuclei and Neutron Stars*. Physical Review C, 90(4):044305. doi:10.1103/PhysRevC.90.044305 (2014). ISSN 0556-2813.



- Chen, W.-C. and J. Piekarewicz. *Searching for isovector signatures in the neutron-rich oxygen and calcium isotopes*. Physics Letters B, 748:284. doi:10.1016/j.physletb.2015.07.020 (2015). ISSN 03702693.
- Chen, S., *et al.* *Common-red-Signal Analysis With 24-Yr High-precision Timing of the European Pulsar Timing Array: Inferences in the Stochastic Gravitational-wave Background Search*. Monthly Notices of the Royal Astronomical Society, 508(4):4970. doi:10.1093/mnras/stab2833 (2021). ISSN 0035-8711.
- Clifton, T. *et al.* *Modified Gravity and Cosmology*. Physics Reports, 513(1-3):1. doi:10.1016/j.physrep.2012.01.001 (2012). ISSN 03701573.
- Cooney, A., S. DeDeo, and D. Psaltis. *Neutron Stars in  $f(R)$  Gravity with Perturbative Constraints*. Physical Review D, 82(6):064033. doi:10.1103/PhysRevD.82.064033 (2010). ISSN 1550-7998.
- Copeland, E. J. *Dynamics of Dark Energy*. In *AIP Conference Proceedings*, volume 957, pages 21–29 (2007). ISBN 9780735404717. ISSN 0094243X. doi:10.1063/1.2823765.
- Cordes, J. M., A. Pidwerbetsky, and R. V. E. Lovelace. *Refractive and Diffractive Scattering in the Interstellar Medium*. The Astrophysical Journal, 310:737. doi:10.1086/164728 (1986). ISSN 0004-637X.
- Cordes, J. M., R. M. Shannon, and D. R. Stinebring. *Frequency-Dependent Dispersion Measures and Implication for Pulsar Timing*. The Astrophysical Journal, 817(1):16. doi:10.3847/0004-637x/817/1/16 (2016).
- Coughlin, M. W. and T. Dietrich. *Can a Black Hole–Neutron Star Merger explain GW170817, AT2017GFO, and GRB170817A?* Physical Review D, 100(4):043011. doi:10.1103/PhysRevD.100.043011 (2019). ISSN 2470-0010.
- Danielewicz, P., R. Lacey, and W. G. Lynch. *Determination of the Equation of State of Dense Matter*. Science, 298(5598):1592. doi:10.1126/science.1078070 (2002). ISSN 0036-8075.
- Datta, S. and P. Char. *Effect of Superfluid Matter of a Neutron Star on the Tidal Deformability*. Physical Review D, 101(6):064016. doi:10.1103/PhysRevD.101.064016 (2020). ISSN 2470-0010.
- De, K. and Y. Gupta. *A Real-Time Coherent Dedispersion Pipeline for the Giant Metrewave Radio*

- Telescope*. *Experimental Astronomy*, 41(1-2):67. doi:10.1007/s10686-015-9476-8 (2016). ISSN 15729508.
- De, S., *et al.* *Tidal Deformabilities and Radii of Neutron Stars from the Observation of GW170817*. *Physical Review Letters*, 121(9):091102. doi:10.1103/PhysRevLett.121.091102 (2018). ISSN 0031-9007.
- De Felice, A. and S. Tsujikawa. *f(R) Theories*. *Living Reviews in Relativity*, 13(1):3. doi:10.12942/lrr-2010-3 (2010). ISSN 2367-3613.
- Demorest, P. B. *Measuring the Gravitational Wave Background Using Precision Pulsar Timing*. Ph.D. thesis, University of California, Berkeley (2007).
- Demorest, P. B., *et al.* *A Two-Solar-Mass Neutron Star Measured Using Shapiro Delay*. *Nature*, 467(7319):1081. doi:10.1038/nature09466 (2010). ISSN 0028-0836.
- Demorest, P. B., *et al.* *Limits on the Stochastic Gravitational Wave Background From the North American Nanohertz Observatory for Gravitational Waves*. *The Astrophysical Journal*, 762(2):94. doi:10.1088/0004-637X/762/2/94 (2013). ISSN 0004-637X.
- Desvignes, G., *et al.* *High-Precision Timing of 42 Millisecond Pulsars with the European Pulsar Timing Array*. *Monthly Notices of the Royal Astronomical Society*, 458(3):3341. doi:10.1093/mnras/stw483 (2016). ISSN 13652966.
- Detweiler, S. *Pulsar Timing Measurements and the Search for Gravitational Waves*. *The Astrophysical Journal*, 234:1100 (1979).
- Dexheimer, V. *et al.* *Phase Transitions in Neutron Stars*. *International Journal of Modern Physics E*, 27(11):1830008. doi:10.1142/S0218301318300084 (2018). ISSN 0218-3013.
- Dirkes, A. *Gravitational waves — A review on the theoretical foundations of gravitational radiation*. *International Journal of Modern Physics A*, 33(14n15):1830013. doi:10.1142/S0217751X18300132 (2018). ISSN 0217-751X.
- Dolch, T., *et al.* *A 24-Hr Global Campaign to Assess Precision Timing of the Millisecond Pulsar J1713+0747*. *The Astrophysical Journal*, 794(1):21. doi:10.1088/0004-637x/794/1/21 (2014).
- Dover, C. *Hyperon-Nucleus Potentials*. *Progress in Particle and Nuclear Physics*, 12:171. doi:10.1016/0146-6410(84)90004-8 (1984). ISSN 01466410.

- Edwards, R. T., G. B. Hobbs, and R. N. Manchester. *TEMPO2, a new pulsar timing package - II. The timing model and precision estimates*. Monthly Notices of the Royal Astronomical Society, 372(4):1549. doi:10.1111/j.1365-2966.2006.10870.x (2006). ISSN 00358711.
- Einstein, A. *The Foundation of the General Theory of Relativity*. Annalen Phys., 49(7):769. doi:10.1002/andp.19163540702 (1916).
- Einstein, A. *Zum Kosmologischen Problem der Allgemeinen Relativitätstheorie*. Albert Einstein: Akademie-Vorträge: Sitzungsberichte der Preußischen Akademie der Wissenschaften 1914–1932, pages 361–364 (1931).
- Eisenstein, D. J., et al. *Detection of the Baryon Acoustic Peak in the Large-Scale Correlation Function of SDSS Luminous Red Galaxies*. The Astrophysical Journal, 633(2):560. doi:10.1086/466512 (2005). ISSN 0004-637X.
- Faraoni, V. *Illusions of General Relativity in Brans-Dicke Gravity*. Physical Review D, 59(8):084021. doi:10.1103/PhysRevD.59.084021 (1999). ISSN 0556-2821.
- Folkner, W. and R. Park. *JPL Planetary and Lunar Ephemeris DE436 JUNO/kernels/spk/de436s. bsp. lbl*. Tech. rep., Jet Propulsion Laboratory, Pasadena, CA (2016).
- Fonseca, E., et al. *The NANOGrav Nine-Year Data set: Mass and Geometric Measurements of Binary Millisecond Pulsars*. The Astrophysical Journal, 832(2):167. doi:10.3847/0004-637X/832/2/167 (2016). ISSN 1538-4357.
- Fonseca, E., et al. *Refined Mass and Geometric Measurements of the High-mass PSR J0740+6620*. The Astrophysical Journal Letters, 915(1):L12. doi:10.3847/2041-8213/ac03b8 (2021). ISSN 2041-8205.
- Fortin, M., et al. *Neutron Star Radii and Crusts: Uncertainties and Unified Equations of State*. Physical Review C, 94(3):035804. doi:10.1103/PhysRevC.94.035804 (2016). ISSN 2469-9985.
- Foster, R. S. and D. C. Backer. *Constructing a Pulsar Timing Array*. The Astrophysical Journal, 361:300. doi:10.1086/169195 (1990). ISSN 0004-637X.
- Frusciante, N., et al. *The role of the tachyonic instability in Horndeski gravity*. Journal of Cosmology and Astroparticle Physics, 2019(02):029. doi:10.1088/1475-7516/2019/02/029 (2019). ISSN 1475-7516.
- Gelman, A. et al. *Bayesian Data Analysis, Third Edition*. Chapman & Hall/CRC Texts in Statistical Science. Taylor & Francis (2013). ISBN 9781439840955.

- Glendenning, N. K. *Compact stars: Nuclear Physics, Particle Physics and General Relativity*. Springer-Verlag New York (1997).
- Goncharov, B., *et al.* *On the Evidence for a Common-Spectrum Process in the Search for the Nanohertz Gravitational-wave Background with the Parkes Pulsar Timing Array*. *The Astrophysical Journal Letters*, 917(2):L19. doi:10.3847/2041-8213/ac17f4 (2021). ISSN 2041-8205.
- Gorda, T., O. Komoltsev, and A. Kurkela. *Ab-initio QCD Calculations Impact the Inference of the Neutron-Star-Matter Equation of State* (2022).
- Guinot, B. and P. K. Seidelmann. *Time Scales - Their History, Definition and Interpretation*. *Astronomy & Astrophysics*, 194(1-2):304 (1988).
- Gupta, Y., *et al.* *The Upgraded GMRT: Opening new Windows on the Radio Universe*. *Current Science*, 113(4):707. doi:10.18520/cs/v113/i04/707-714 (2017). ISSN 00113891.
- Gusakov, M. E., E. M. Kantor, and D. D. Ofengeim. *Magnetic field evolution time-scales in superconducting neutron stars*. *Monthly Notices of the Royal Astronomical Society*, 499(3):4561. doi:10.1093/mnras/staa3160 (2020). ISSN 0035-8711.
- Guth, A. H. *Inflationary Universe: A Possible Solution to the Horizon and Flatness Problems*. *Physical Review D*, 23(2):347. doi:10.1103/PhysRevD.23.347 (1981). ISSN 0556-2821.
- Hellings, R. and G. Downs. *Upper Limits on the Isotropic Gravitational Radiation Background From Pulsar Timing Analysis*. *The Astrophysical Journal*, 265:L39 (1983).
- Hempel, M. and J. Schaffner-Bielich. *A Statistical Model for a Complete Supernova Equation of State*. *Nuclear Physics A*, 837(3-4):210. doi:10.1016/j.nuclphysa.2010.02.010 (2010). ISSN 03759474.
- Hernandez Vivanco, F. *et al.* *Measuring the Neutron Star Equation of State with Gravitational Waves: The First Forty Binary Neutron Star Merger Observations*. *Physical Review D*, 100(10):103009. doi:10.1103/PhysRevD.100.103009 (2019). ISSN 2470-0010.
- Hessels, J. W. T., *et al.* *A Radio Pulsar Spinning at 716 Hz*. *Science*, 311(5769):1901. doi:10.1126/science.1123430 (2006). ISSN 0036-8075.
- Hewish, A., *et al.* *Observation of a Rapidly Pulsating Radio Source*. *Nature*, 217(5130):709. doi:10.1038/217709a0 (1968). ISSN 0028-0836.

- Hinderer, T. *Tidal Love Numbers of Neutron Stars*. The Astrophysical Journal, 677(2):1216. doi: 10.1086/533487 (2008). ISSN 0004-637X.
- Hobbs, G. *Pulsars and Gravitational Wave Detection*. Publications of the Astronomical Society of Australia, 22(3):179. doi:10.1071/AS04063 (2005). ISSN 1323-3580.
- Hobbs, G. *Pulsars as gravitational wave detectors*. pages 229–245 (2011). doi:10.1007/978-3-642-17251-9\_20.
- Hobbs, G. *The Parkes Pulsar Timing Array*. Classical and Quantum Gravity, 30(22):224007. doi: 10.1088/0264-9381/30/22/224007 (2013). ISSN 02649381.
- Hobbs, G. B., R. T. Edwards, and R. N. Manchester. *TEMPO2, a new Pulsar-Timing Package - I. An Overview*. Monthly Notices of the Royal Astronomical Society, 369(2):655. doi:10.1111/j.1365-2966.2006.10302.x (2006).
- Hobbs, G., et al. *The International Pulsar Timing Array Project: Using Pulsars as a Gravitational Wave Detector*. Classical and Quantum Gravity, 27(8):084013. doi:10.1088/0264-9381/27/8/084013 (2010). ISSN 02649381.
- Hobbs, G., et al. *An Ultra-wide Bandwidth (704 to 4032 MHz) Receiver for the Parkes Radio Telescope*. Publications of the Astronomical Society of Australia, 37:e012. doi:10.1017/pasa.2020.2 (2020). ISSN 1323-3580.
- Hotan, A. W., W. Van Straten, and R. N. Manchester. *PSRCHIVE and PSRFITS: An Open Approach to Radio Pulsar Data Storage and Analysis*. Publications of the Astronomical Society of Australia, 21(3):302. doi:10.1071/AS04022 (2004). ISSN 14486083.
- Huang, C. et al. *Constraining Fundamental Nuclear Physics Parameters Using Neutron Star Mass-Radius Measurements I: Nucleonic Models* (2023).
- Hulse, R. A. *The discovery of the binary pulsar*. Reviews of Modern Physics, 66(3):699. doi:10.1103/RevModPhys.66.699 (1994). ISSN 0034-6861.
- Huterer, D. and M. S. Turner. *Prospects for Probing the Dark Energy via Supernova Distance Measurements*. Physical Review D, 60(8):081301. doi:10.1103/PhysRevD.60.081301 (1999). ISSN 0556-2821.

- Imam, S. M. A. *et al.* *Bayesian Reconstruction of Nuclear Matter Parameters From the Equation of State of Neutron Star Matter*. *Phys. Rev. C*, 105(1):015806. doi:10.1103/PhysRevC.105.015806 (2022).
- Ivezić, Ž., *et al.* *Statistics, Data Mining, and Machine Learning in Astronomy*. Princeton University Press (2014).
- Jiang, J.-L., C. Ecker, and L. Rezzolla. *Bayesian Analysis of Neutron-Star Properties With Parameterized Equations of State: The Role of the Likelihood Functions* (2022).
- Jiménez Forteza, X., *et al.* *Impact of High-order Tidal Terms on Binary Neutron-Star Waveforms*. *Physical Review D*, 98(12):124014. doi:10.1103/PhysRevD.98.124014 (2018). ISSN 2470-0010.
- Johnston, S., *et al.* *Two Years of Pulsar Observations With the Ultra-wide-band Receiver on the Parkes Radio Telescope*. *Mon. Not. Roy. Astron. Soc.*, 502(1):1253. doi:10.1093/mnras/stab095 (2021).
- Joshi, B. C., *et al.* *Precision Pulsar Timing with the ORT and the GMRT and its Applications in Pulsar Astrophysics*. *Journal of Astrophysics and Astronomy*, 39(4):51. doi:10.1007/s12036-018-9549-y (2018).
- Joshi, B. C., *et al.* *Nanohertz Gravitational Wave Astronomy During the SKA Era: An InPTA Perspective*. *Journal of Astrophysics and Astronomy*, 10 (2022).
- Kamionkowski, M. and E. D. Kovetz. *The Quest for B Modes from Inflationary Gravitational Waves*. *Annual Review of Astronomy and Astrophysics*, 54(1):227. doi:10.1146/annurev-astro-081915-023433 (2016). ISSN 0066-4146.
- Kanakis-Pegios, A., P. S. Koliogiannis, and C. C. Moustakidis. *Speed of sound constraints from tidal deformability of neutron stars*. *Physical Review C*, 102(5):055801. doi:10.1103/PhysRevC.102.055801 (2020). ISSN 2469-9985.
- Kaur, D., *et al.* *Detection of Frequency-dependent Dispersion Measure Toward the Millisecond Pulsar J2241-5236 From Contemporaneous Wideband Observations*. *The Astrophysical Journal Letters*, 930(2):L27. doi:10.3847/2041-8213/ac64ff (2022).
- Kazanas, D. *Dynamics of the Universe and Spontaneous Symmetry Breaking*. *The Astrophysical Journal*, 241:L59. doi:10.1086/183361 (1980). ISSN 0004-637X.
- Keitel, D. *Multiple-Image Lensing Bayes Factor for a set of Gravitational-Wave Events*. *Research Notes of the AAS*, 3(3):46. doi:10.3847/2515-5172/ab0c0b (2019). ISSN 2515-5172.

- Keith, M. J., *et al.* *Measurement and Correction of Variations in Interstellar Dispersion in High-Precision Pulsar Timing*. *Monthly Notices of the Royal Astronomical Society*, 429(3):2161. doi:10.1093/mnras/sts486 (2013).
- Kendall, M. G. *A new Measure of Rank Correlation*. *Biometrika*, 30(1-2):81. doi:10.1093/biomet/30.1-2.81 (1938). ISSN 0006-3444.
- Kerr, M., *et al.* *The Parkes Pulsar Timing Array Project: Second Data Release*. *Publications of the Astronomical Society of Australia*, 37:e020. doi:10.1017/pasa.2020.11 (2020). ISSN 1323-3580.
- Kramer, M. and D. J. Champion. *The European Pulsar Timing Array and the Large European Array for Pulsars*. *Classical and Quantum Gravity*, 30(22):224009. doi:10.1088/0264-9381/30/22/224009 (2013). ISSN 02649381.
- Krishnakumar, M. A., *et al.* *High Precision Measurements of Interstellar Dispersion Measure With the Upgraded GMRT*. *Astronomy & Astrophysics*, 651:A5. doi:10.1051/0004-6361/202140340 (2021).
- Lagos, M., *et al.* *A General Theory of Linear Cosmological Perturbations: Scalar-Tensor and Vector-Tensor Theories*. *Journal of Cosmology and Astroparticle Physics*, 2016(08):007. doi:10.1088/1475-7516/2016/08/007 (2016). ISSN 1475-7516.
- Lam, M. T., *et al.* *A Second Chromatic Timing Event of Interstellar Origin toward PSR J1713+0747*. *The Astrophysical Journal*, 861(2):132. doi:10.3847/1538-4357/aac770 (2018).
- Landry, P., R. Essick, and K. Chatziioannou. *Nonparametric Constraints on Neutron Star Matter With Existing and Upcoming Gravitational Wave and Pulsar Observations*. *Phys. Rev. D*, 101(12):123007. doi:10.1103/PhysRevD.101.123007 (2020).
- Large, M. I., A. E. Vaughan, and B. Y. Mills. *A Pulsar Supernova Association?* *Nature*, 220(5165):340. doi:10.1038/220340a0 (1968). ISSN 0028-0836.
- Lee, K. J. *Prospects of Gravitational Wave Detection Using Pulsar Timing Array for Chinese Future Telescopes*. In L. Qain and D. Li, editors, *Frontiers in Radio Astronomy and FAST Early Sciences Symposium 2015*, volume 502 of *Astronomical Society of the Pacific Conference Series*, page 19. *Astronomical Society of the Pacific* (2016).
- Lentati, L., *et al.* *European Pulsar Timing Array Limits on an Isotropic Stochastic Gravitational-Wave*

- Background*. Monthly Notices of the Royal Astronomical Society, 453(3):2577. doi:10.1093/mnras/stv1538 (2015). ISSN 0035-8711.
- Lentati, L., *et al.* *Robust Estimation of Scattering in Pulsar Timing Analysis*. Monthly Notices of the Royal Astronomical Society, 468(2):1474. doi:10.1093/mnras/stx580 (2017).
- Levin, L., *et al.* *The NANOGrav Nine-Year Data set: Monitoring Interstellar Scattering Delays*. The Astrophysical Journal, 818(2):166. doi:10.3847/0004-637x/818/2/166 (2016).
- LIGO. *GW170817: Measurements of Neutron Star Radii and Equation of State* The LIGO Scientific Collaboration and The Virgo Collaboration. Physical review letters, 121(16):161101 (2018).
- Liu, K., *et al.* *Measuring Pulse Times of Arrival From Broad-Band Pulsar Observations*. Monthly Notices of the Royal Astronomical Society, 443(4):3752. doi:10.1093/mnras/stu1420 (2014).
- Llanes-Estrada, F. J. *Constraining Gravity With Hadron Physics: Neutron Stars, Modified Gravity and Gravitational Waves*. EPJ Web Conf., 137:01013. doi:10.1051/epjconf/201713701013 (2017).
- Löhmer, O., *et al.* *The Parallax, Mass and age of the PSR J2145-0750 Binary System*. Astronomy & Astrophysics, 426:631. doi:10.1051/0004-6361:20041031 (2004).
- Lommen, A. N. *Pulsar timing arrays: the promise of gravitational wave detection*. Reports on Progress in Physics, 78(12):124901. doi:10.1088/0034-4885/78/12/124901 (2015). ISSN 0034-4885.
- Lorimer, D. R. and M. Kramer. *Handbook of Pulsar Astronomy*. Cambridge University Press (2012).
- Lugones, G. *Magnetic Fields in High-Density Stellar Matter*. In *AIP Conference Proceedings*, volume 784, pages 253–262. AIP (2005). ISSN 0094243X. doi:10.1063/1.2077189.
- Maan, Y., J. van Leeuwen, and D. Vohl. *Fourier Domain Excision of Periodic Radio Frequency Interference*. Astronomy & Astrophysics, 650:A80. doi:10.1051/0004-6361/202040164 (2021). ISSN 0004-6361.
- Malik, T., B. K. Agrawal, and C. Providência. *Inferring the Nuclear Symmetry Energy at Suprasaturation Density From Neutrino Cooling*. Phys. Rev. C, 106(4):L042801. doi:10.1103/PhysRevC.106.L042801 (2022).
- Malik, T., S. Banik, and D. Bandyopadhyay. *Equation-of-state Table with Hyperon and Antikaon for Supernova and Neutron Star Merger*. The Astrophysical Journal, 910(2):96. doi:10.3847/1538-4357/abe860 (2021). ISSN 0004-637X.



- Malik, T. and C. Providência. *Bayesian Inference of Signatures of Hyperons Inside Neutron Stars*. Physical Review D, 106(6):063024. doi:10.1103/PhysRevD.106.063024 (2022). ISSN 2470-0010.
- Malik, T., et al. *GW170817: Constraining the Nuclear Matter Equation of State From the Neutron Star Tidal Deformability*. Physical Review C, 98(3):035804. doi:10.1103/PhysRevC.98.035804 (2018). ISSN 2469-9985.
- Malik, T. et al. *Spanning the Full Range of Neutron Star Properties Within a Microscopic Description* (2023).
- Manchester, R. N., et al. *The Parkes Pulsar Timing Array Project*. Publications of the Astronomical Society of Australia, 30:e017. doi:10.1017/pasa.2012.017 (2013). ISSN 1323-3580.
- McLaughlin, M. A. *The North American Nanohertz Observatory for Gravitational Waves*. Classical and Quantum Gravity, 30(22):224008. doi:10.1088/0264-9381/30/22/224008 (2013). ISSN 02649381.
- Meacher, D., et al. *Mock data and science challenge for detecting an astrophysical stochastic gravitational-wave background with Advanced LIGO and Advanced Virgo*. Physical Review D, 92(6):063002. doi:10.1103/PhysRevD.92.063002 (2015). ISSN 1550-7998.
- Meyers, B. and Chime/Pulsar Collaboration. *Confirmation of a Change in the Emission Properties of PSR J1713+0747*. The Astronomer's Telegram, 14652:1 (2021).
- Mignani, R. P., et al. *Studies of neutron stars at optical/IR wavelengths*. Astrophysics and Space Science, 308(1-4):203. doi:10.1007/s10509-007-9340-z (2007). ISSN 0004-640X.
- Milgrom, M. *A Modification of the Newtonian Dynamics as a Possible Alternative to the Hidden Mass Hypothesis*. The Astrophysical Journal, 270:365. doi:10.1086/161130 (1983). ISSN 0004-637X.
- Miller, M. C. and F. K. Lamb. *Observational constraints on neutron star masses and radii*. The European Physical Journal A, 52(3):63. doi:10.1140/epja/i2016-16063-8 (2016). ISSN 1434-6001.
- Miller, M. C., et al. *PSR J0030+0451 Mass and Radius from NICER Data and Implications for the Properties of Neutron Star Matter*. The Astrophysical Journal, 887(1):L24. doi:10.3847/2041-8213/ab50c5 (2019). ISSN 2041-8213.
- Miller, M. C. et al. *The Radius of PSR J0740+6620 from NICER and XMM-Newton Data*. The Astrophysical Journal Letters, 918(2):L28. doi:10.3847/2041-8213/ac089b (2021). ISSN 2041-8205.

- Miralles, J. A., V. Urpin, and D. Konenkov. *Joule Heating and the Thermal Evolution of Old Neutron Stars*. The Astrophysical Journal, 503(1):368. doi:10.1086/305967 (1998). ISSN 0004-637X.
- Nice, D., *et al.* *Tempo: Pulsar Timing Data Analysis* (2015).
- Nobleson, K., T. Malik, and S. Banik. *Tidal Deformability of Neutron Stars with Exotic Particles Within a Density Dependent Relativistic Mean Field Model in R-squared Gravity*. Journal of Cosmology and Astroparticle Physics, 2021(08):012. doi:10.1088/1475-7516/2021/08/012 (2021). ISSN 1475-7516.
- Nobleson, K., *et al.* *Low-Frequency Wideband Timing of InPTA Pulsars Observed With the uGMRT*. Monthly Notices of the Royal Astronomical Society, 512(1):1234. doi:10.1093/mnras/stac532 (2022). ISSN 0035-8711.
- Ofengeim, D. D. and D. G. Yakovlev. *Analytic description of neutron star cooling*. Monthly Notices of the Royal Astronomical Society, 467(3):3598. doi:10.1093/mnras/stx366 (2017). ISSN 0035-8711.
- O'Hanlon, J. *Intermediate-Range Gravity: A Generally Covariant Model*. Physical Review Letters, 29(2):137. doi:10.1103/PhysRevLett.29.137 (1972). ISSN 0031-9007.
- Oppenheimer, J. R. and G. M. Volkoff. *On Massive Neutron Cores*. Physical Review, 55(4):374. doi:10.1103/PhysRev.55.374 (1939). ISSN 0031-899X.
- Orellana, M. *et al.* *Structure of Neutron Stars in R-Squared Gravity*. General Relativity and Gravitation, 45(4):771. doi:10.1007/s10714-013-1501-5 (2013). ISSN 0001-7701.
- Otto, K., M. Oertel, and B.-J. Schaefer. *Hybrid and Quark Star Matter Based on a Nonperturbative Equation of State*. Physical Review D, 101(10):103021. doi:10.1103/PhysRevD.101.103021 (2020). ISSN 2470-0010.
- Padmanabhan, T. *Cosmological Constant — The Weight of the Vacuum*. Physics Reports, 380(5-6):235. doi:10.1016/S0370-1573(03)00120-0 (2003). ISSN 03701573.
- Paladi, A. K., *et al.* *Multi-band Extension of the Wideband Timing Technique* (2023).
- Patra, N. K. *et al.* *Nearly Model-Independent Constraints on Dense Matter Equation of State in a Bayesian Approach*. Phys. Rev. D, 106(4):043024. doi:10.1103/PhysRevD.106.043024 (2022).
- Payne, E., C. Talbot, and E. Thrane. *Higher Order Gravitational-Wave Modes with Likelihood Reweighting*. Physical Review D, 100(12):123017. doi:10.1103/PhysRevD.100.123017 (2019). ISSN 2470-0010.

- Pennucci, T. T. *Frequency-Dependent Template Profiles for High-Precision Pulsar Timing*. The Astrophysical Journal, 871(1):34. doi:10.3847/1538-4357/aaf6ef (2019).
- Pennucci, T. T., P. B. Demorest, and S. M. Ransom. *Elementary Wideband Timing of Radio Pulsars*. The Astrophysical Journal, 790(2):93. doi:10.1088/0004-637X/790/2/93 (2014).
- Pennucci, T. T., P. B. Demorest, and S. M. Ransom. *Pulse Portraiture: Pulsar timing* (2016).
- Percival, W. J., *et al.* *Measuring the Baryon Acoustic Oscillation Scale Using the Sloan Digital Sky Survey and 2dF Galaxy Redshift Survey*. Monthly Notices of the Royal Astronomical Society, 381(3):1053. doi:10.1111/j.1365-2966.2007.12268.x (2007). ISSN 00358711.
- Perera, B. B., *et al.* *The International Pulsar Timing Array: Second Data Release*. Monthly Notices of the Royal Astronomical Society, 490(4):4666. doi:10.1093/mnras/stz2857 (2019). ISSN 13652966.
- Perlmutter, S., *et al.* *Measurements of  $\Omega$  and  $\Lambda$  from 42 High-Redshift Supernovae*. The Astrophysical Journal, 517(2):565. doi:10.1086/307221 (1999). ISSN 0004-637X.
- Peters, P. C. and J. Mathews. *Gravitational Radiation from Point Masses in a Keplerian Orbit*. Physical Review, 131(1):435. doi:10.1103/PhysRev.131.435 (1963). ISSN 0031-899X.
- Popov, S. B. *High magnetic field neutron stars and magnetars in binary systems*. Proceedings of the International Astronomical Union, 16(S363):61. doi:10.1017/S1743921322000308 (2020). ISSN 1743-9213.
- Raaijmakers, G., *et al.* *A NICER View of PSR J0030+0451: Implications for the Dense Matter Equation of State*. The Astrophysical Journal, 887(1):L22. doi:10.3847/2041-8213/ab451a (2019). ISSN 2041-8213.
- Radice, D., *et al.* *GW170817: Joint Constraint on the Neutron Star Equation of State from Multimessenger Observations*. The Astrophysical Journal, 852(2):L29. doi:10.3847/2041-8213/aaa402 (2018). ISSN 2041-8213.
- Raithel, C. A. *Constraints on the Neutron Star Equation of State from GW170817*. The European Physical Journal A, 55(5):80. doi:10.1140/epja/i2019-12759-5 (2019). ISSN 1434-6001.
- Raithel, C. A., F. Özel, and D. Psaltis. *Tidal Deformability from GW170817 as a Direct Probe of the Neutron Star Radius*. The Astrophysical Journal, 857(2):L23. doi:10.3847/2041-8213/aabcbf (2018). ISSN 2041-8213.

- Ramachandran, R., *et al.* *Interstellar Plasma Weather Effects in Long-Term Multifrequency Timing of Pulsar B1937+21*. *The Astrophysical Journal*, 645(1):303. doi:10.1086/500634 (2006).
- Reddy, S. H., *et al.* *A Wideband Digital Back-End for the Upgraded GMRT*. *Journal of Astronomical Instrumentation*, 6(1):1641011. doi:10.1142/S2251171716410117 (2017). ISSN 22511725.
- Reddy, S. H., *et al.* *Timestamp Flow in GWB and Correction*. Technical report, National Centre for Radio Astrophysics, Pune (2021).
- Regge, T. and J. A. Wheeler. *Stability of a Schwarzschild Singularity*. *Physical Review*, 108(4):1063. doi:10.1103/PhysRev.108.1063 (1957). ISSN 0031-899X.
- Renzini, A. I., *et al.* *Stochastic Gravitational-Wave Backgrounds: Current Detection Efforts and Future Prospects*. *Galaxies*, 10(1):34. doi:10.3390/galaxies10010034 (2022). ISSN 2075-4434.
- Rickett, B. J. *Interstellar Scattering and Scintillation of Radio Waves*. *Annual Review of Astronomy and Astrophysics*, 15(1):479. doi:10.1146/annurev.aa.15.090177.002403 (1977).
- Riess, A. G., *et al.* *Observational Evidence from Supernovae for an Accelerating Universe and a Cosmological Constant*. *The Astronomical Journal*, 116(3):1009. doi:10.1086/300499 (1998). ISSN 00046256.
- Riley, T. E. *et al.* *A NICER View of PSR J0030+0451: Millisecond Pulsar Parameter Estimation*. *Astrophys. J. Lett.*, 887(1):L21. doi:10.3847/2041-8213/ab481c (2019).
- Riley, T. E., *et al.* *A NICER View of the Massive Pulsar PSR J0740+6620 Informed by Radio Timing and XMM-Newton Spectroscopy*. *The Astrophysical Journal Letters*, 918(2):L27. doi:10.3847/2041-8213/ac0a81 (2021). ISSN 2041-8205.
- Romani, R. W., *et al.* *PSR J09520607: The Fastest and Heaviest Known Galactic Neutron Star*. *The Astrophysical Journal Letters*, 934(2):L17. doi:10.3847/2041-8213/ac8007 (2022). ISSN 2041-8205.
- Romano, J. D. and N. J. Cornish. *Detection methods for stochastic gravitational-wave backgrounds: a unified treatment*. *Living Reviews in Relativity*, 20(1):2. doi:10.1007/s41114-017-0004-1 (2017). ISSN 2367-3613.
- Sahni, V. and A. Starobinsky. *The Case for a Positive Cosmological  $\Lambda$ -Term*. *International Journal of Modern Physics D*, 09(04):373. doi:10.1142/S0218271800000542 (2000). ISSN 0218-2718.

- Sakharov, A. D. *Vacuum Quantum Fluctuations in Curved Space and the Theory of Gravitation*. Soviet Physics Uspekhi, 34(5):394. doi:10.1070/PU1991v034n05ABEH002498 (1991). ISSN 0038-5670.
- Sato, T., *et al.* *High-entropy ejecta plumes in Cassiopeia A from neutrino-driven convection*. Nature, 592(7855):537. doi:10.1038/s41586-021-03391-9 (2021). ISSN 0028-0836.
- Schaffner, J. and I. N. Mishustin. *Hyperon-Rich Matter in Neutron Stars*. Physical Review C, 53(3):1416. doi:10.1103/PhysRevC.53.1416 (1996). ISSN 0556-2813.
- Shannon, R. M. and J. M. Cordes. *Modelling and Mitigating Refractive Propagation Effects in Precision Pulsar Timing Observations*. Monthly Notices of the Royal Astronomical Society, 464(2):2075. doi:10.1093/mnras/stw2449 (2017).
- Shannon, R. M., *et al.* *Gravitational-Wave Limits from Pulsar Timing Constrain Supermassive Black Hole Evolution*. Science, 342(6156):334. doi:10.1126/science.1238012 (2013). ISSN 0036-8075.
- Shannon, R. M., *et al.* *The Disturbance of a Millisecond Pulsar Magnetosphere*. The Astrophysical Journal Letters, 828(1):L1. doi:10.3847/2041-8205/828/1/L1 (2016).
- Sharma, S. S., *et al.* *Wide-band Timing of GMRT Discovered Millisecond Pulsars*. arXiv e-prints, arXiv:2201.04386 (2022).
- Siemens, X., *et al.* *The Stochastic Background: Scaling Laws and Time to Detection for Pulsar Timing Arrays*. Classical and Quantum Gravity, 30(22):224015. doi:10.1088/0264-9381/30/22/224015 (2013).
- Singha, J., *et al.* *Evidence for Profile Changes in PSR J1713+0747 Using the uGMRT*. Monthly Notices of the Royal Astronomical Society, 507(1):L57. doi:10.1093/mnrasl/slab098 (2021).
- Somasundaram, R. *et al.* *Perturbative QCD and the Neutron Star Equation of State* (2022).
- Sotiriou, T. P. and V. Faraoni.  *$f(R)$  Theories of Gravity*. Reviews of Modern Physics, 82(1):451. doi:10.1103/RevModPhys.82.451 (2010). ISSN 0034-6861.
- Spergel, D. N., *et al.* *First-Year Wilkinson Microwave Anisotropy Probe (WMAP) Observations: Determination of Cosmological Parameters*. The Astrophysical Journal Supplement Series, 148(1):175. doi:10.1086/377226 (2003). ISSN 0067-0049.

- Spergel, D. N., *et al.* *Three-Year Wilkinson Microwave Anisotropy Probe (WMAP) Observations: Implications for Cosmology.* The Astrophysical Journal Supplement Series, 170(2):377. doi:10.1086/513700 (2007). ISSN 0067-0049.
- Staelin, D. H. and E. C. Reifstein. *Pulsating Radio Sources near the Crab Nebula.* Science, 162(3861):1481. doi:10.1126/science.162.3861.1481 (1968). ISSN 0036-8075.
- Starobinsky, A. *A new Type of Isotropic Cosmological Models Without Singularity.* Physics Letters B, 91(1):99. doi:10.1016/0370-2693(80)90670-X (1980). ISSN 03702693.
- Steiner, A. W., M. Hempel, and T. Fischer. *Core-Collapse Supernova Equations of State Based on Neutron Star Observations.* Astrophys. J., 774:17. doi:10.1088/0004-637X/774/1/17 (2013).
- Sugahara, Y. and H. Toki. *Relativistic Mean-Field Theory for Unstable Nuclei with Non-Linear  $\sigma$  and  $\omega$  terms.* Nuclear Physics A, 579(3-4):557. doi:10.1016/0375-9474(94)90923-7 (1994). ISSN 03759474.
- Susobhanan, A., *et al.* *pinta: The uGMRT Data Processing Pipeline for the Indian Pulsar Timing Array.* Publications of the Astronomical Society of Australia, 38:e017. doi:10.1017/pasa.2021.12 (2021). ISSN 1323-3580.
- Swarup, G., *et al.* *Large Steerable Radio Telescope at Ootacamund, India.* Nature Physical Science, 230(17):185. doi:10.1038/physci230185a0 (1971). ISSN 0300-8746.
- Tang, S.-P., *et al.* *The Masses of Isolated Neutron Stars Inferred from the Gravitational Redshift Measurements.* The Astrophysical Journal, 888(1):45. doi:10.3847/1538-4357/ab5959 (2020). ISSN 1538-4357.
- Tauris, T. M. and E. P. J. van den Heuvel. *Formation and evolution of compact stellar X-ray sources.* In *Compact Stellar X-ray Sources*, pages 623–666. Cambridge University Press (2006). doi:10.1017/CBO9780511536281.017.
- Taylor, J. H. *Pulsar Timing and Relativistic Gravity.* Royal Society of London Philosophical Transactions Series A, 341:117. doi:10.1098/rsta.1992.0088 (1992).
- Taylor, J. H. *Pulsar Timing and Relativistic Gravity.* Philosophical Transactions of the Royal Society of London. Series A: Physical and Engineering Sciences, 341(1660):117. doi:10.1098/rsta.1992.0088 (1992). ISSN 0962-8428.

- Teyssandier, P. and P. Tournenc. *The Cauchy Problem for the  $R+R^2$  Theories of Gravity Without Torsion*. Journal of Mathematical Physics, 24(12):2793. doi:10.1063/1.525659 (1983). ISSN 0022-2488.
- Thrane, E., V. Mandic, and N. Christensen. *Detecting very long-lived gravitational-wave transients lasting hours to weeks*. Physical Review D, 91(10):104021. doi:10.1103/PhysRevD.91.104021 (2015). ISSN 1550-7998.
- Tolman, R. C. *Static Solutions of Einstein's Field Equations for Spheres of Fluid*. Physical Review, 55(4):364. doi:10.1103/PhysRev.55.364 (1939). ISSN 0031-899X.
- Tolos, L., M. Centelles, and A. Ramos. *Equation of State for Nucleonic and Hyperonic Neutron Stars with Mass and Radius Constraints*. Astrophys. J., 834(1):3. doi:10.3847/1538-4357/834/1/3 (2017).
- Traversi, S., P. Char, and G. Pagliara. *Bayesian Inference of Dense Matter Equation of State within Relativistic Mean Field Models Using Astrophysical Measurements*. The Astrophysical Journal, 897(2):165. doi:10.3847/1538-4357/ab99c1 (2020). ISSN 1538-4357.
- Typel, S. *Relativistic Model for Nuclear Matter and Atomic Nuclei With Momentum-Dependent Self-Energies*. Physical Review C, 71(6):064301. doi:10.1103/PhysRevC.71.064301 (2005). ISSN 0556-2813.
- Typel, S., *et al.* *Composition and Thermodynamics of Nuclear Matter with Light Clusters*. Physical Review C, 81(1):015803. doi:10.1103/PhysRevC.81.015803 (2010). ISSN 0556-2813.
- van Straten, W. and M. Bailes. *DSPSR: Digital Signal Processing Software for Pulsar Astronomy*. Publications of the Astronomical Society of Australia, 28(1):1–14. doi:10.1071/AS10021 (2011).
- Verlinde, E. *On the origin of gravity and the laws of Newton*. Journal of High Energy Physics, 2011(4):29. doi:10.1007/JHEP04(2011)029 (2011). ISSN 1029-8479.
- Walecka, J. *A Theory of Highly Condensed Matter*. Annals of Physics, 83(2):491. doi:10.1016/0003-4916(74)90208-5 (1974). ISSN 00034916.
- Walecka, J. D. *The Relativistic Nuclear Many-Body Problem*. In *The Relativistic Nuclear Many-Body Problem*, pages 229–271. Springer, Boston, MA (1986). doi:10.1007/978-1-4684-5179-5\_8.
- Walecka, J. D. *Theoretical Nuclear and Subnuclear Physics*. Co-published with Imperial College Press (2004). ISBN 978-981-238-795-0. doi:10.1142/5500.

- Wei, J.-B., *et al.* *Neutron star universal relations with microscopic equations of state.* Journal of Physics G: Nuclear and Particle Physics, 46(3):034001. doi:10.1088/1361-6471/aaf95c (2019). ISSN 0954-3899.
- Weinberg, S. *The Cosmological Constant Problem.* Reviews of Modern Physics, 61(1):1. doi:10.1103/RevModPhys.61.1 (1989). ISSN 0034-6861.
- Weisberg, J. M., D. J. Nice, and J. H. Taylor. *TIMING MEASUREMENTS OF THE RELATIVISTIC BINARY PULSAR PSR B1913+16.* The Astrophysical Journal, 722(2):1030. doi:10.1088/0004-637X/722/2/1030 (2010). ISSN 0004-637X.
- Weisberg, J. M. and J. H. Taylor. *Gravitational radiation from an orbiting pulsar.* General Relativity and Gravitation, 13(1):1. doi:10.1007/BF00766292 (1981). ISSN 0001-7701.
- Wesolowski, S. *et al.* *Bayesian Parameter Estimation for Effective Field Theories.* J. Phys. G, 43(7):074001. doi:10.1088/0954-3899/43/7/074001 (2016).
- Will, C. M. *The Confrontation Between General Relativity and Experiment.* Living Reviews in Relativity, 17(1):4. doi:10.12942/lrr-2014-4 (2014). ISSN 2367-3613.
- Xu, H., *et al.* *A Sustained Pulse Shape Change in PSR J1713+0747 Possibly Associated with Timing and DM Events.* The Astronomer's Telegram, 14642:1 (2021).
- Yagi, K. and N. Yunes. *I-Love-Q Relations in Neutron Stars and Their Applications to Astrophysics, Gravitational Waves, and Fundamental Physics.* Physical Review D, 88(2):023009. doi:10.1103/PhysRevD.88.023009 (2013). ISSN 1550-7998.
- Yazadjiev, S. S., D. D. Doneva, and K. D. Kokkotas. *Tidal Love Numbers of Neutron Stars in  $f(R)$  Gravity.* The European Physical Journal C, 78(10):818. doi:10.1140/epjc/s10052-018-6285-z (2018). ISSN 1434-6044.
- Yazadjiev, S. S., *et al.* *Non-Perturbative and Self-Consistent Models of Neutron Stars in R-Squared Gravity.* Journal of Cosmology and Astroparticle Physics, 2014(06):003. doi:10.1088/1475-7516/2014/06/003 (2014). ISSN 1475-7516.
- You, X. P., *et al.* *Dispersion Measure Variations and Their Effect on Precision Pulsar Timing.* Monthly Notices of the Royal Astronomical Society, 378(2):493. doi:10.1111/j.1365-2966.2007.11617.x (2007). ISSN 0035-8711.



# List of Publications and Presentations

## List of Publications Relevant to This Thesis

- **Nobleson, K.**, A. Ali, and S. Banik, *Comparison of Perturbative and Non-perturbative Methods in  $f(R)$  Gravity*, The European Physical Journal C, 82(1):32, doi:10.1140/epjc/s1005n2n-021-09969-x (2022a), ISSN 1434-6044.
- **Nobleson, K.**, T. Malik, and S. Banik, *Tidal Deformability of Neutron Stars with Exotic Particles Within a Density Dependent Relativistic Mean Field Model in R-squared Gravity*, Journal of Cosmology and Astroparticle Physics, 2021(08):012, doi:10.1088/1475-7516/2021/08/012 (2021), ISSN 1475-7516
- **Nobleson, K.**, et al., *Low-Frequency Wideband Timing of InPTA Pulsars Observed With the uGMRT*, Monthly Notices of the Royal Astronomical Society, 512(1):1234, doi:10.1093/mnras/stac532 (2022b), ISSN 0035-8711.
- Tarafdar, P., **Nobleson, K.**, et al., *The Indian Pulsar Timing Array: First Data Release*, Publications of the Astronomical Society of Australia, 39:e053, doi:10.1017/pasa.2022.46 (2022), ISSN 1323-3580.
- **Nobleson, K.**, S. Banik, and T. Malik. *Unveiling a universal relationship between the  $f(R)$  parameter and neutron star properties*. Physical Review D, 107(12):124045.(2023).

## List of Other Publications

1. Susobhanan, A., **Nobleson, K.**, et al. *pinta: The uGMRT Data Processing Pipeline for the Indian Pulsar Timing Array*. Publications of the Astronomical Society of Australia, 38:e017. doi:10.1017/pasa.2021.12 (2021). ISSN 1323-3580.

2. Krishnakumar, M. A., **Nobleson, K.**, et al. *High Precision Measurements of Interstellar Dispersion Measure With the Upgraded GMRT*. *Astronomy & Astrophysics*, 651:A5. doi:10.1051/0004-6361/202140340 (2021).
3. Singha, J., **Nobleson, K.**, et al. *Evidence for Profile Changes in PSR J1713+0747 Using the uGMRT*. *Monthly Notices of the Royal Astronomical Society*, 507(1):L57. doi:10.1093/mnrasl/slab098 (2021).
4. Joshi, B. C., **Nobleson, K.**, et al. *Nanohertz Gravitational Wave Astronomy During the SKA Era: An InPTA Perspective*. *Journal of Astrophysics and Astronomy*, 10 (2022).
5. Srivastava, A., **Nobleson, K.**, et al. *Noise analysis of the Indian Pulsar Timing Array data release I*. *Physical Review D*, 108(2):023008.
6. Paladi, A. K., **Nobleson, K.**, et al. *Multi-band Extension of the Wideband Timing Technique* <https://arxiv.org/abs/2304.13072> (2023)
7. Antoniadis, J., **Nobleson, K.**, et al. *The second data release from the European Pulsar Timing Array II: Customised pulsar noise models for spatially correlated gravitational waves* (2023a), <https://arxiv.org/abs/2306.16225>.
8. Antoniadis, J., **Nobleson, K.**, et al. *The second data release from the European Pulsar Timing Array III: Search for gravitational wave signals* (2023b), <https://arxiv.org/abs/2306.16214>.
9. Antoniadis, J., **Nobleson, K.**, et al. *The second data release from the European Pulsar Timing Array IV: Search for continuous gravitational wave signals* (2023c), <https://arxiv.org/abs/2306.16226>.
10. Antoniadis, J., **Nobleson, K.**, et al. *The second data release from the European Pulsar Timing Array: V: Implications for massive black holes, dark matter and the early Universe* (2023d) <https://arxiv.org/abs/2306.16227>.

## List of Talks and Presentations

### Invited

1. Research Facility Training Program, Osmania University 2022, *Neutron Stars as Tools to Study Advanced Astrophysics*

## Oral

1. 32nd meeting of Indian Association for General Relativity and Gravitation (IAGRG32) 2022, *Tidal Deformability of Neutron Stars With Exotic Particles Within a Density-Dependent Relativistic Mean Field Model in R-Squared Gravity*, **Nobleson K.**, Malik T., Banik S.
2. International Pulsar Timing Array – Catchup meeting 2022, *The Indian Pulsar Timing Array: First Data Release*. Tarafdar P., **Nobleson K.**, et al.
3. Science at Low Frequencies VIII 2021, *Low-frequency Wideband Timing on uGMRT Data*, **Nobleson K.**, et al.
4. 27th International Conference of International Academy of Physical Sciences on Advances in Relativity and Cosmology 2021, *Tidal Deformability of Neutron Stars With Exotic Particles Within a Density-Dependent Relativistic Mean Field Model in R-Squared Gravity*, **Nobleson K.**, Malik T., Banik S.
5. Astronomical Society of India – 2020, *Neutron Stars With Realistic EoS in  $f(R)$  Theories of Gravity*, **Nobleson K.**, Ali A., Banik S.

## Poster

1. Astronomical Society of India – 2022, *Tidal deformability of neutron stars with exotic particles within a density-dependent relativistic mean field model in R-squared gravity*, **Nobleson K.**, Malik T., Banik S.
2. International Pulsar Timing Array – Catchup meeting 2021, *Low-frequency wideband timing on uGMRT data*, **Nobleson K.**, et al.

## List of Seminars and Workshops Attended

1. Compact stars in the QCD phase diagram VIII: The era of multi-messenger astronomy, August 17 to 21, 2020, Online, Organized by ICTS, Bangalore.
2. 1-day Online Symposium on Physics of Neutron Stars, June 16, 2021, Organized by BITS-Pilani, Hyderabad Campus.
3. DataScience in Astrophysics 2019 workshop, November 1-3, 2019, IIIT Allahabad
4. Pulsar Astronomy with uGMRT Boot-Camp & Multi-Wavelength Neutron Star Workshop, January 3-8, 2018, BITS-Pilani, Hyderabad Campus.

## **Brief Biography of Nobleson K.**

Mr. Nobleson completed his Masters of Science (Astrophysics) from Osmania University, India. He joined Department of Physics, Birla Institute of Technology and Science-Pilani: Hyderabad Campus, as Research Fellow funded by the institute in the year 2019 to carry out his doctoral research work under the supervision of Prof. Sarmistha Banik. He also joined the Indian Pulsar Array collaboration in 2019 and has been an active member since. He presented his research work in different scientific conferences (National and International) and attended various workshops and seminars related to his research area. Mr. Nobleson published his results in at least five internationally reputed peer-to-peer review journals, such as, Physical Review D, The European Physical Journal C (EPJ-C), Journal of Cosmology and Astroparticle Physics (JCAP), Monthly Notices of the Royal Astronomical Society (MNRAS), Publications of the Astronomical Society of Australia (PASA), Astronomy & Astrophysics (A&A), etc.

## **Brief Biography of Prof. Sarmistha Banik**

Prof. Sarmistha Banik is presently working as a Professor in the Department of Physics, Birla Institute of Technology and Science, Pilani, Hyderabad Campus. She has also been a visiting associate at the Inter-University Center for Astronomy & Astrophysics (IUCAA), Pune, India, since 2015. She got PhD degree from Calcutta University and pursued her postdoctoral studies at School of Physics & Astronomy, University of Manchester, UK. Prof. Banik is an Alexander von Humboldt Fellow and worked as a guest scientist at Frankfurt Institute for Advanced Studies, Germany with Humboldt fellowship. She is involved in neutron star research for the last 20 years. She has published around 50 research articles and delivered invited lectures at various national and international conferences. Prof. Banik has visited many reputed institutes in the world and established joint collaborations. Her small research group comprising of research scholars and postdoctoral fellows have successfully hosted national level workshop on neutron stars. Teaching physics is a passion that Prof. Banik takes a keen interest in.